TABLE OF CONTENTS - Appendix C

List of Figures ..... C–ii
List of Tables ..... C–v

Appendix C
Interim Report on Analysis of Aircraft Impact into the WTC Towers C–1

C.1 Introduction C–1
C.2 Material Constitutive Modeling C–1
C.2.1 WTC Tower Steel Constitutive Models C–2
C.2.2 Failure Models C–12
C.2.3 Concrete Constitutive Models C–31
C.2.4 Aircraft Constitutive Models C–32
C.3 Development of Aircraft Model C–33
C.3.1 Aircraft Data Collection C–33
C.3.2 Description of the Aircraft Model C–33
C.3.3 Analysis of Fuel Distribution at Impact C–40
C.4 Component-Level Analyses C–47
C.4.1 Analysis Methodology C–49
C.4.2 Exterior Column Impact Analyses C–50
C.4.3 Core Column Impact Analyses C–63
C.4.4 Combined Engine Impact Analyses C–63
C.4.5 Floor Assembly Component Analyses C–67
C.5 Summary and Preliminary Findings C–68
C.6 References C–71

LIST OF FIGURES

Figure C–1. Example finite element models of the ASTM 370 rectangular tensile specimen. C–3

Figure C–2. Example finite element models of the ASTM 370 round bar tensile specimen. C–4

Figure C–3. Test data and true stres-strain conversion for the 75 ksi steel. C–6

Figure C–4. Tabular true stress-strain constitutive model curve for the 75 ksi steel. C–6

Figure C–5. Calculated tensile test response with necking for the 75 ksi steel. C–7

Figure C–6. Comparison of measured and calculated engineering stress-strain curves for the 75 ksi steel. C–7

Figure C–7. Comparison of the constitutive model and synthetic steel behaviors for the 75 ksi steel. C–8

Figure C–8. Tabular true stress-strain constitutive model curves. C–9

Figure C–9. Comparison of the constitutive model and synthetic steel behaviors for the higher strength perimeter steel curves. C–9

Figure C–10. Comparison of the constitutive model and synthetic steel behaviors for the lower strength perimeter steel curves. C–10

Figure C–11. Comparison of the constitutive model and synthetic steel behaviors for the core steel curves. C–10

Figure C–12. Comparison of rate effects model and test data. C–12

Figure C–13. Calculated necking response in the 75 ksi tensile specimen. C–14

Figure C–14. Coarse shell element mesh for the 75 ksi tensile specimen. C–14

Figure C–15. Mesh refinement effects in the calculated 75 ksi tensile test. C–15

Figure C–16. Notched round bar specimen dimensions. C–17

Figure C–17. Notched round bar tensile specimen models. C–18

Figure C–18. Calculated notched round bar stress triaxiality. C–18

Figure C–19. Calculated critical plastic strain as a function of notched stress triaxiality. C–19

Figure C–20. Simulation of the notched and smooth round bar tests. C–20

Figure C–21. Photograph of an exterior column with weld zone fractures. C–21

Figure C–22. Micrograph of an exterior column weld geometry. C–21

Figure C–23. Microhardness characterization of the weld and HAZ materials. C–22

Figure C–24. 2-D weldment model developed for analysis of failure behavior. C–23

Figure C–25. Simulation of the 55 ksi steel tensile test. C–24

Figure C–26. Mesh resolutions used in the 2-D weldment failure model. C–24

Figure C–27. Calculated weldment deformations and failure. C–25

Figure C–28. Detail of the calculated weldment failure behavior. C–25

Figure C–29. Mesh refinement effects on calculated weldment failure behavior. C–26
Figure C–30. Calculated energy balance for the 2-D weldment models. C–27
Figure C–31. Drop test model for column weld fracture analysis. C–27
Figure C–32. Models developed for column weld fracture analysis. C–28
Figure C–33. Calculated strain profile for the weld zone. C–29
Figure C–34. Calculated drop test fracture behavior. C–29
Figure C–35. Measured bolt load-displacement behavior. C–30
Figure C–36. Comparison of the measured and calculated bolt behavior. C–31
Figure C–37. Finite element analysis of the unconfined compression test. C–32
Figure C–38. Comparison of the calculated unconfined compression behavior with concrete compression test data. C–33
Figure C–39. Digitized engineering stress-strain curves for various 2024 aluminum alloys. C–34
Figure C–40. Digitized engineering stress-strain curves for various 7075 aluminum alloys. C–34
Figure C–41. True stress-strain curves developed for various aircraft aluminum alloys. C–35
Figure C–42. Tabular true stress-strain curves developed for various aircraft aluminum alloys. C–35
Figure C–43. Pratt and Whitney PW4000 turbofan engine. C–36
Figure C–44. PW4000 engine cross sectional geometry and simplification. C–37
Figure C–45. Pratt and Whitney PW4000 turbofan engine model. C–37
Figure C–46. Finite element model of the Boeing 767-200ER. C–40
Figure C–47. Complete empennage for the 767 aircraft model. C–41
Figure C–48. Retracted landing gear components for the 767 aircraft model. C–41
Figure C–49. Underside of the 767 airframe model (skin removed) showing the position of retracted main landing gear. C–42
Figure C–50. Complete wing structures for the 767 aircraft model. C–42
Figure C–51. Small wing section model for component-level analyses. C–43
Figure C–52. Wing section model developed for the subassembly impact simulations. C–43
Figure C–53. Flammable material locations in a Boeing 767 aircraft. C–44
Figure C–54. Layout of fuel tanks in the Boeing 767 wing. C–45
Figure C–55. Approximate fuel tank dimensions C–46
Figure C–56. Wing cross sections at various rib locations. C–46
Figure C–57. Fuel tank capacity. C–47
Figure C–58. Approximate fuel locations for smooth and level flight. C–48
Figure C–59. Exterior column response comparison, showing contours of the displacement magnitude C–51
Figure C–60. Calculated impact damage with the empty short wing section component model. C–52
Figure C–61. Damage produced by the empty wing section impact. C–52

Figure C–62. SPH fuel in the small wing segment. C–53
Figure C–63. Exterior panels impact behavior for a wing segment with fuel (SPH fuel model)..... C–54
Figure C–64. SPH Analysis of structural damage and fuel dispersion (top view). C–55
Figure C–65. ALE analysis of structural damage and fuel dispersion (top view)..... C–55
Figure C–66. SPH analysis of structural damage and fuel dispersion (side view)..... C–56
Figure C–67. ALE analysis of structural damage and fuel dispersion (side view). C–56
Figure C–68. Exterior column end connection modeling. C–58
Figure C–69. Typical bolt bearing shear failures of spandrel connections. C–58
Figure C–70. Bolted spandrel connection modeling. C–59
Figure C–71. Example engine impact analysis with exterior columns. C–60
Figure C–72. Engine velocity history for the exterior wall impact. C–61
Figure C–73. Example engine impact analysis with different impact locations. C–61
Figure C–74. Example engine impact analysis with different spandrel connection treatments. C–62
Figure C–75. Engine velocity history for the exterior wall impact. C–62
Figure C–76. Wide flange core column response comparison, showing contours of the displacement magnitude. C–64
Figure C–77. Displacement and kinetic energy comparison for wide flange core column wing impact analysis. C–64
Figure C–78. Box core column response comparison, showing contours of the displacement magnitude C–65
Figure C–79. Displacement and kinetic energy comparison for box core column wing impact analysis. C–65
Figure C–80. Example engine impact analysis with interior and exterior columns. C–66
Figure C–81. Example engine impact analysis with interior and exterior columns. C–67
Figure C–82. Floor assembly impact analysis with brick element concrete slab. C–69
Figure C–83. Floor assembly impact analysis with shell element concrete slab. C–70

LIST OF TABLES

Table C–1. Material constitutive parameter table–WTC tower steels. C–11
Table C–2. Summary of notched round bar tensile tests. C–17
Table C–3. 2-D weldment model comparison. C–26
Table C–4. Engine model parameters. C–38
Table C–5. Boeing 767 engine comparison. C–38
Table C–6. Summary of Boeing 767-200 aircraft model size (under construction). C–42
Table C–7. Truss floor assembly component analyses comparison. C–68

This page intentionally left blank.

Appendix C
INTERIM REPORT ON ANALYSIS OF AIRCRAFT IMPACT INTO THE WTC TOWERS

C.1 INTRODUCTION

One of the objectives of Project 2, Baseline Structural Performance and Aircraft Impact Damage Analysis, of the National Institute of Standards and Technology (NIST)-led investigation into the collapse of the World Trade Center (WTC) towers is to analyze the aircraft impact into each of the two towers. The purpose of this analysis is to provide the following: (1) estimates of the damage to structural systems due to aircraft impact—including exterior walls, floor systems, and interior core columns; (2) estimates of the aircraft fuel dispersal during impact; (3) estimates of accelerations and deformations as a function of time in each of the two towers due to aircraft impact to be used for estimating damage to fire proofing; and (4) a database of the major fragments of the aircraft and destroyed structural components of the towers to be used for estimating damage to the mechanical and architectural systems inside the towers. The analyses, thus, establish the initial conditions for the fire dynamics modeling in Project 5, Reconstruction of Thermal and Tenability Environment, and the thermal-structural response and collapse initiation analysis in Project 6, Structural Fire Response and Collapse Analysis.

The impact analyses are conducted at various levels including: (1) the component level, (2) the subassembly level, and (3) the global level to estimate the probable damage to the towers due to aircraft impact. The analyses also include simplified and approximate methods. Analysis of uncertainties using the component, subassembly, global, and simplified analyses will also be conducted to assess the effect of variability associated with various parameters on the damage estimates. NIST is working with experts from Applied Research Associates (ARA), Inc., to conduct the impact analyses. This appendix summarizes the progress made to date on this project. Emphasis is on the models development and component level analyses.

Section C.2 outlines the development of constitutive models describing the actual behavior of the various materials included in the aircraft impact analysis. The materials in this section include WTC steels, reinforced concrete, and aircraft materials. Special emphasis is also placed on the modeling of weldments and bolts. Section C.3 presents the status of the development of the aircraft model, including the engine and airframe. This section also provides an analysis of the fuel distribution at the time of aircraft impact. Section C.4 provides details on the component level analyses performed to date, including exterior and core columns, column and spandrel connections, and floor segments under the impact of an aircraft engine or a segment of a wing. A summary and preliminary findings are provided in Section C.5.

C.2 MATERIAL CONSTITUTIVE MODELING

An important requirement for high fidelity simulation of the aircraft impact damage is the development of constitutive models to represent the actual behavior of the structure under the dynamic impact conditions of the aircraft. The primary materials that need to be considered for the component analyses are the several grades of steel used in the columns, spandrels, and floor trusses and beams of the WTC towers,

the concrete floor slabs, and the aluminum airframe structure of the Boeing 767 aircraft. All of these materials play a significant role in the aircraft impact damage analyses. These materials also display significant nonlinear rate-dependent deformation and failure behavior.

The analysis of the aircraft impact damage is being performed with the LS-DYNA finite element code (LS-DYNA 2003). LS-DYNA has an extensive library of more that 130 different constitutive models and is capable of accurately reproducing the important material behaviors required in this analysis. Material models currently available in LS-DYNA have been utilized for the analyses using material data from tests conducted by NIST or available in the public domain.

Secondary materials of interest include the nonstructural aircraft components and masses such as fuel, seats, interior trim, cargo, and luggage. Furthermore, a significant part of the mass of the WTC towers is material not included in the primary structural steel frame that includes windows, nonstructural walls, partitions, furniture and other building contents, flooring, mechanical equipment, and insulation. Selection of the constitutive modeling for these secondary material behaviors has not yet been performed. However, the strength of these materials is relatively small compared to the structural materials and simple description of their constitutive behavior will be adequate.

C.2.1 WTC Tower Steel Constitutive Models

Various constitutive models are available in LS-DYNA that can capture the nonlinear behavior of the steel under impact conditions including strain rates effects and failure. The primary constitutive model applied to date is the Piecewise Linear Plasticity model. This model is sufficient to model the nonlinear dynamic deformation and failure of the steel structures. A tabular effective stress versus effective strain curve can be used in this model with various definitions of strain rate dependency.

The constitutive model parameters were developed for each grade of steel used in the construction of the WTC towers based on engineering stress-strain data provided by Project 3 of the NIST-led investigation on Mechanical and Metallurgical Analysis of Structural Steel. The approach to developing the constitutive parameters for each grade of steel was:

- Convert the engineering stress-strain curve to a true stress versus true strain curve. The conversion process is described below and is valid up to the onset of necking in the specimen.
- Extrapolate the true-stress-strain curve beyond the point of necking onset.
- Perform iterative finite element analyses of the tensile test and adjust the true stress-strain curve extrapolation and failure strain until the necking behavior and failure point are accurately captured. The primary criterion is the quantitative agreement of the measured and calculated engineering stress-strain behavior in the softening region beyond maximum stress. These analyses require a fine mesh resolution in the specimen to accurately model the large strain deformation response during necking.
- Perform a final finite element analysis of the material test using a coarser mesh resolution (medium mesh corresponding to the mesh resolution applied in the component analyses). Adjust the failure criteria (strain at failure) to obtain failure at the same engineering strain level.

The advantage of this approach is that the measured nonlinear material behavior up to failure is accurately captured in the constitutive model. In addition, the simulation of the material testing provides a validation that the constitutive model parameters are defined accurately and that the model can reproduce the measured response for the test conditions.

The tensile tests performed by NIST applied the ASTM 370 test standard (ASTM Designation A 370-03a 2003). Example finite element models of a rectangular test specimen with the fine and medium mesh resolutions are shown in Fig. C–1. This specimen type was used for all of the tests on WTC exterior column materials. A similar figure of the round bar specimen models used for testing of the WTC core column steels is shown in Fig. C–2. The typical element length used in the gage section for the fine meshes is approximately 0.015 in. and for the medium meshes is approximately 0.10 in. The use of the specimen models to develop the constitutive model parameters is described in the following subsections.

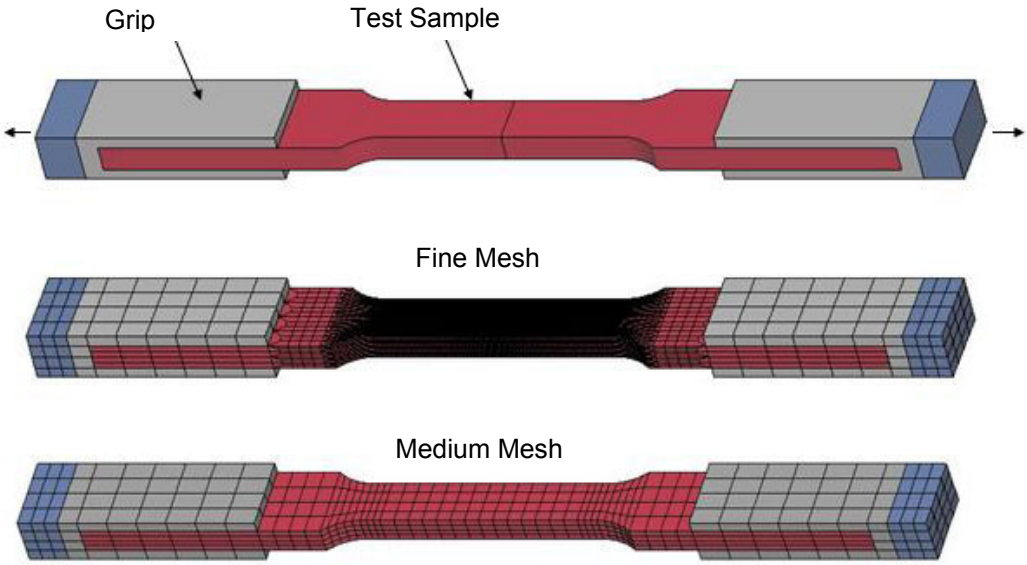

Figure C–1. Example finite element models of the ASTM 370 rectangular tensile specimen.

True Stress and True Strain Corrections

In most tensile tests, a plot is generated of the load measured at the cross head of the testing machine against the displacement of the specimen. A plot of engineering stress versus strain can be generated from this plot by dividing the load by the original cross sectional area of the specimen and the displacement by the original length of the specimen. If the changes in area and length are small during the test, these measures give a good indication of material behavior. However, in reality, the cross section changes (shrinks) significantly during the test and the engineering stress does not yield the “true” stress in the cross section. Similarly, the engineering strain is not representative of the material behavior, especially when a general 3-D state of strain exists. As a result, the engineering stress decreases as some materials approach failure, implying a weakening of the material. In reality, the stress in the cross section is increasing due to the reduction in the cross sectional area (i.e., necking).

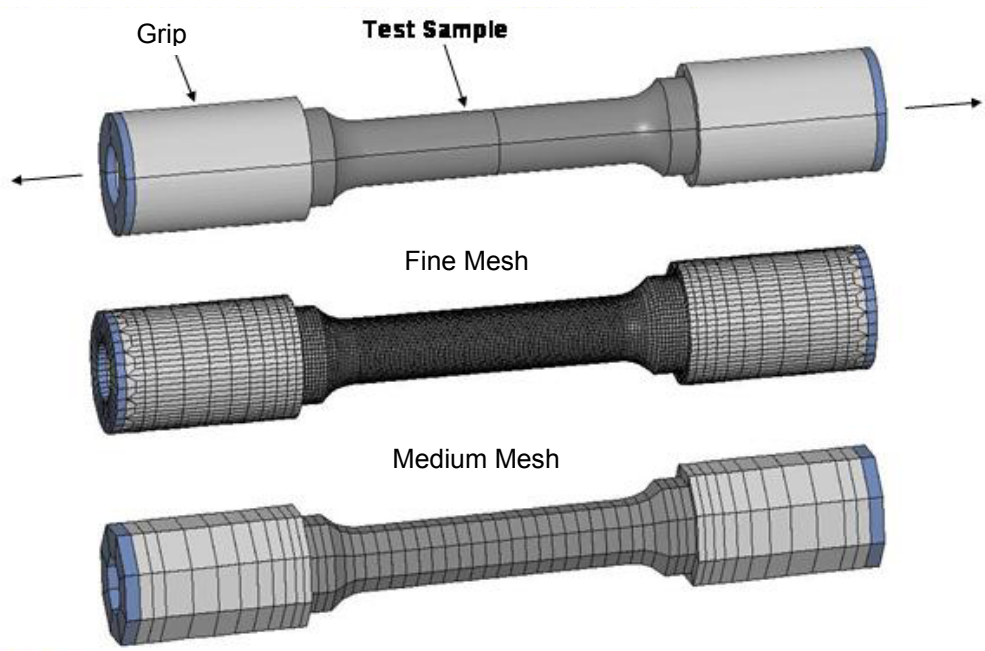

Figure C–2. Example finite element models of the ASTM 370 round bar tensile specimen.

There are several different ways to measure stress and strain based on the coordinate system used. Some are based on material (Lagrangian) coordinates and some on spatial (Eulerian) coordinates. These give rise to terms such as "Green" and "Almansi" strain tensors. These are important in writing a computer code to solve large strain problems. An alternate approach is to define a "true" or "natural" stress and strain. The true stress is based on the load divided by the actual cross sectional area of the specimen and is equal to the engineering stress multiplied by a term to correct for the change in cross section.

$$\sigma_T = \sigma_{eng}(1+e) \tag{1}$$

where:

σ_T = true stress

σ_{eng} = engineering stress

e = engineering strain

The natural or true strain is defined as

$$\varepsilon_T = \ln(\frac{l}{l_o}) = \ln(1+e) \tag{2}$$

where:

ε_T = true strain

This definition comes about from defining the incremental true or "natural" strain as the current "change in length" divided by the current length, or

$$d\varepsilon_T = \frac{dl}{l} \tag{3}$$

This is in contrast with the definition of engineering strain that references the change in length, Δl, divided by the original length, l_0, or

$$e = \frac{\Delta l}{l_0} \tag{4}$$

Development of Steel Constitutive Properties

In this section, examples are provided to illustrate the methodology for the development of the steel constitutive models and typical results. Figure C–3 shows an example of the measured engineering stress-strain behavior for the 75 ksi perimeter column steel. Four tests were performed by Project 3, and the data clearly indicates anisotropy in the behavior introduced by the roll forming process (longitudinal tests L1 and L2 versus transverse tests T1 and T2 in the figure). This particular grade of steel had a larger anisotropy than seen in most of the other steel grades. Whenever anisotropy was observed, the material had greater ductility for specimens aligned with the rolling direction. In addition, the largest effects of the anisotropy were seen in the behavior after the onset of necking.

The first step in the constitutive model development process is to obtain a true stress-true strain curve. The typical approach is to select a representative test and perform the data conversion process described earlier. In this example, the data from test L1 was used to create the true stress-strain curve shown in Fig. C–3. This true stress-strain curve is then approximated by a piecewise linear curve in tabular form as shown in Fig. C–4. This tabular curve is the input used to specify the mechanical behavior in the constitutive model.

The final step is to apply the tabular true stress-strain behavior in the constitutive model to simulate the tensile test as shown in Fig. C–5. If necessary, the extrapolation of the true stress-strain behavior is adjusted until the simulation matches the measured engineering stress-strain response including necking and failure (the portion of the stress-strain curve beyond the maximum engineering stress). A comparison of the calculated and measured tensile behavior for the 75 ksi perimeter steel is shown in Fig. C–6. In this example, the constitutive model was developed as an average between the longitudinal and transverse properties. Test results conducted by Project 3 on the tower steels indicated that the stress-strain behavior is very similar in the longitudinal and transverse directions up to the onset of necking. The difference between the longitudinal and transverse properties is in the ductility, where the average ratio of the longitudinal to transverse strain to failure in the exterior column steels is about 1.22:1. The approach used in the constitutive modeling is to use an average between the longitudinal and transverse properties and ignore the orthotropic characteristics of the material in the impact analyses. The effects produced by the variation of ductility between the longitudinal and transverse directions will be assessed as part of the uncertainty analyses.

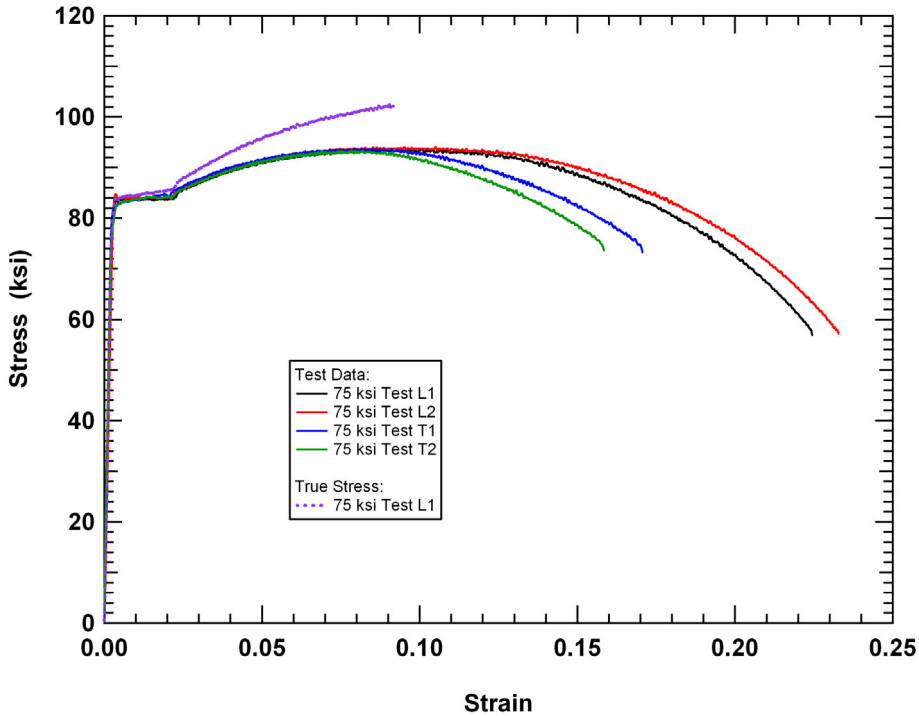

Figure C–3. Test data and true stress-strain conversion for the 75 ksi steel.

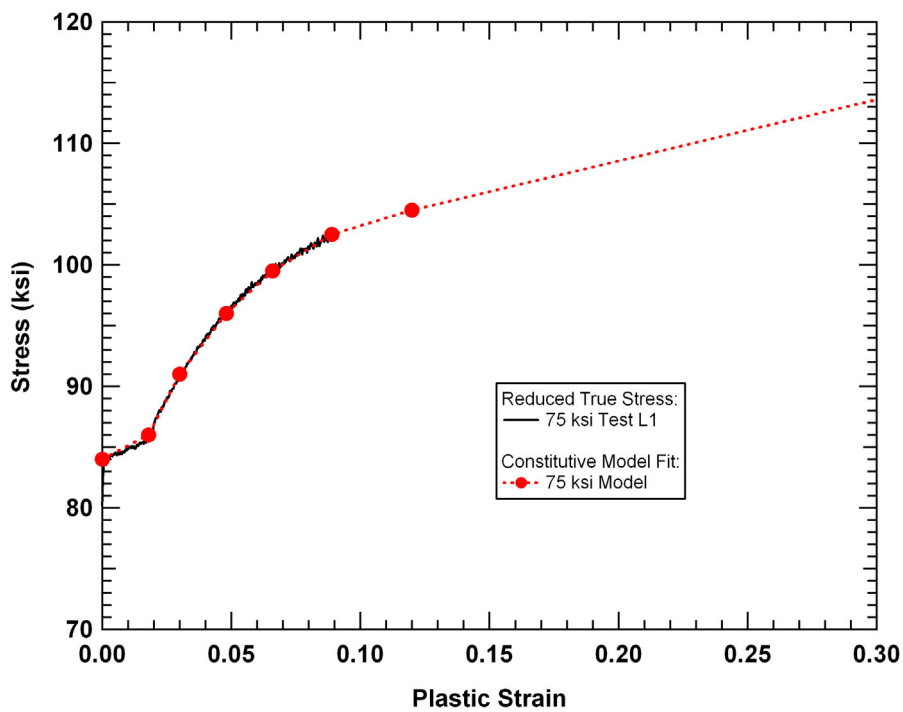

Figure C–4. Tabular true stress-strain constitutive model curve for the 75 ksi steel.

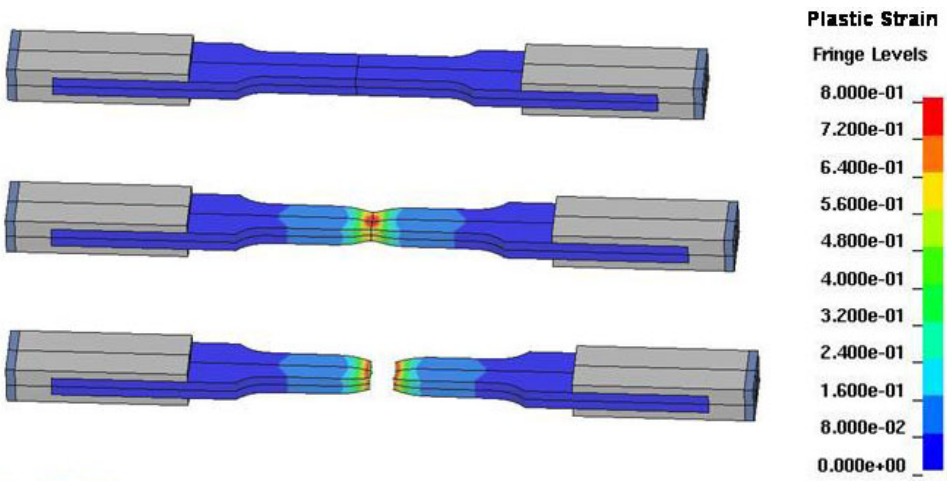

Figure C–5. Calculated tensile test response with necking for the 75 ksi steel.

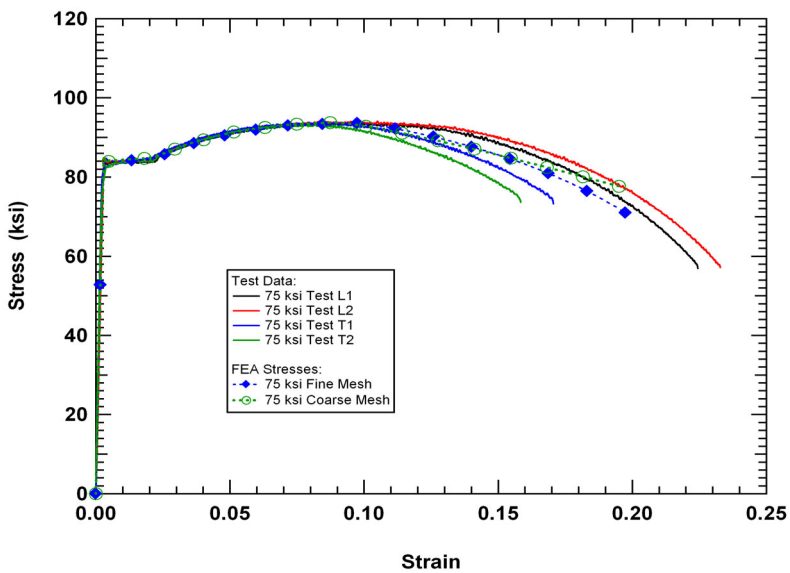

Figure C–6. Comparison of measured and calculated engineering stress-strain curves for the 75 ksi steel.

The resulting true stress-true strain behavior incorporated into the constitutive model is representative of the steels tested in this project. However, there were multiple sources (suppliers) of steel used in the construction of the WTC towers. Project 3 developed synthetic stress-strain curves for each grade of steel based on several data sources. A comparison of this synthetic curve with the constitutive model behavior is shown in Fig. C–7. There are observable differences in the curves such as the representation of a yield point behavior in the constitutive model. However, the differences are not sufficiently large to produce a large variation in the calculated structural impact behavior. In addition, the effect of material strength variation on impact damage will be assessed in the uncertainty analyses.

The above procedure was applied to develop constitutive models for all of the WTC tower steels for which test data was provided by Project 3.

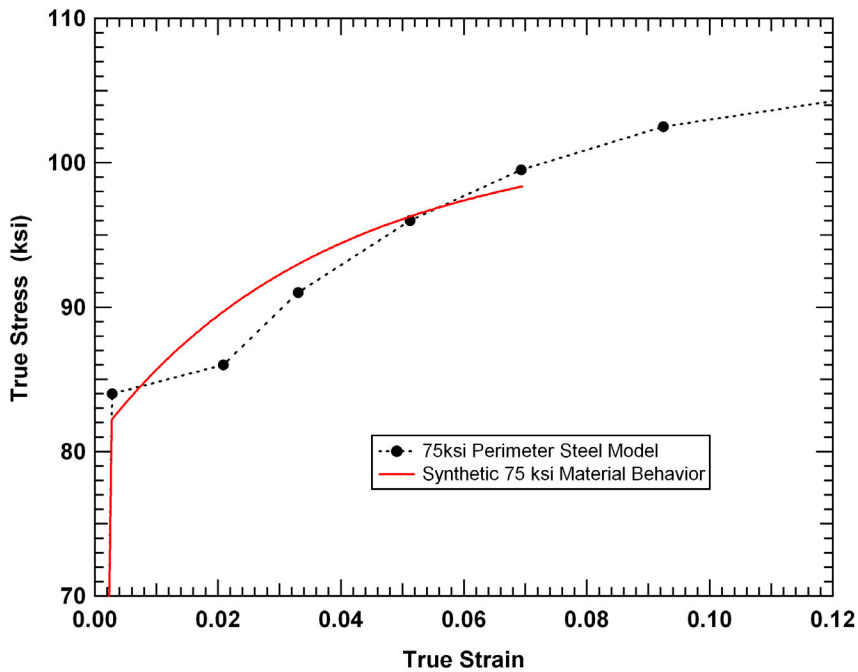

Figure C–7. Comparison of the constitutive model and synthetic steel behaviors for the 75 ksi steel.

Summary of Steel Constitutive Properties

A summary of the true stress-strain curves used in the constitutive models for the various WTC tower steels are summarized in Fig. C–8. Similarly a comparison of the true stress-strain constitutive curves with the synthetic stress-strain curves developed by Project 3 for the various exterior column steels is shown in Figures C–9 and C–10, and for core column steels in Fig. C–11. In general, the true stress-strain curves developed from the test data and the synthetic curves developed from multiple sources agree to within approximately 10 percent. This variation in measured and expected material strengths will be used as part of the future uncertainty analyses.

Strain Rate Effects in Steel Constitutive Models

Strain rate effects on the steel yield strength are included in the constitutive model for tower steels with the Cowper and Symonds rate effect model. The functional form for the rate effects on strength is governed by the equation:

$$\sigma_y\left(\dot{\varepsilon}\right) = \sigma_y\left[1 + \left(\frac{\dot{\varepsilon}}{C}\right)^{1/p}\right] \tag{5}$$

Where σ_y is the yield strength, $\dot{\varepsilon}$ is the strain rate, and C and p are the Cowper and Symonds parameters.

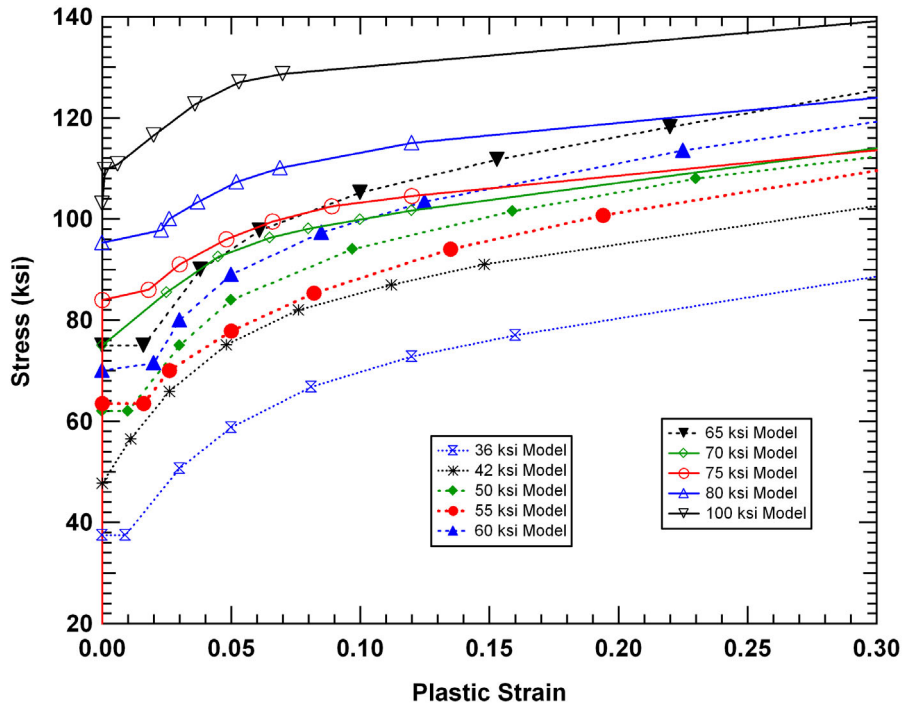

Figure C–8. Tabular true stress-strain constitutive model curves.

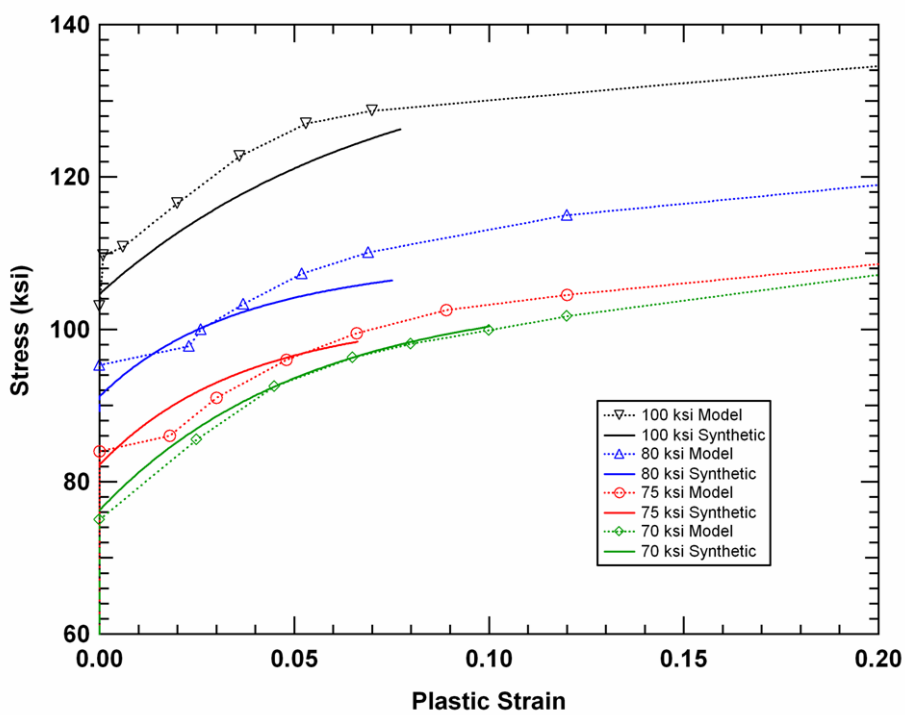

Figure C–9. Comparison of the constitutive model and synthetic steel behaviors for the higher strength perimeter steel curves.

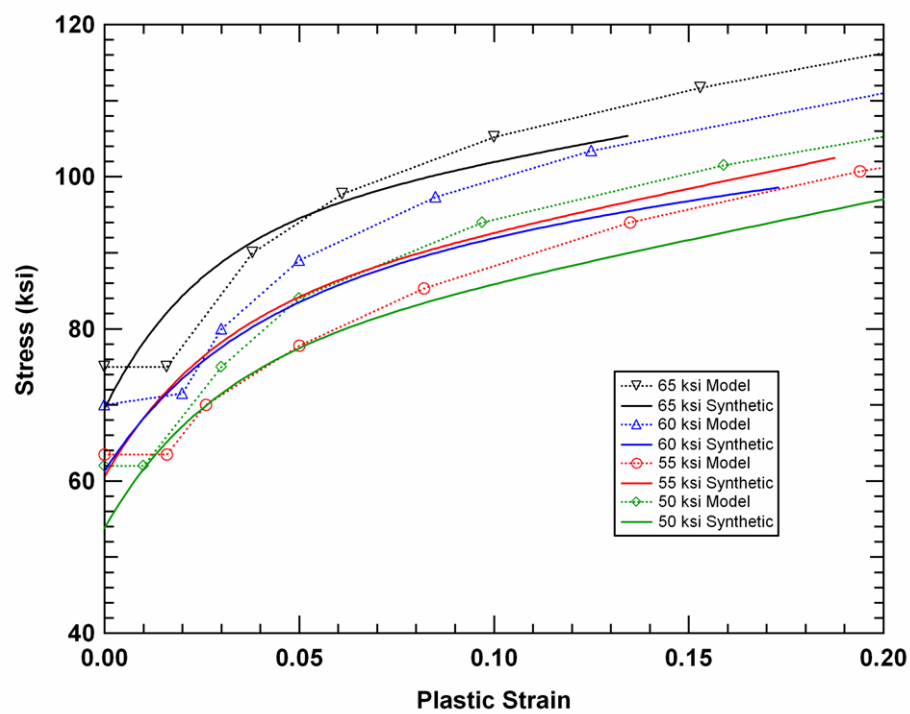

Figure C–10. Comparison of the constitutive model and synthetic steel behaviors for the lower strength perimeter steel curves.

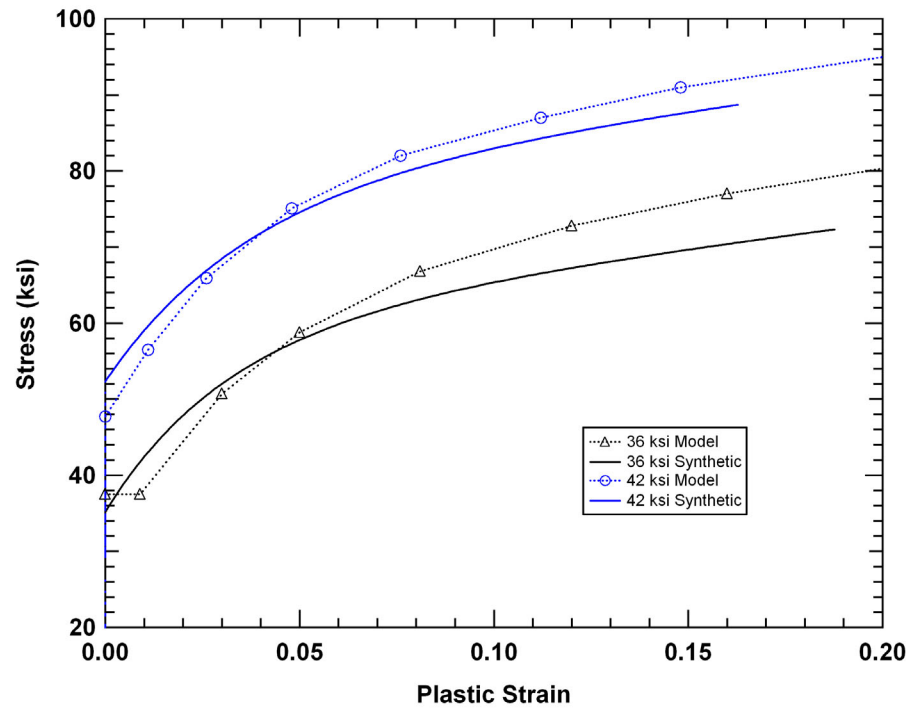

Figure C–11. Comparison of the constitutive model and synthetic steel behaviors for the core steel curves.

A series of high-rate characterization tests was performed on tower steels by Project 3. In addition to quasi-static tests (performed at a rate below 0.001 s^{-1}), a series of high rate tests was performed primarily at strain rates between 100 s^{-1} and 1000 s^{-1}. The Cowper and Symonds model parameters *C* and *p* were then fit to the test data and provided in the following functional form for a strain rate in s^{-1} and a yield strength in ksi:

- $\text{Log}(C) = -7.55 + 0.324\sigma_y - 0.00153(\sigma_y)^2$
- $p = 6.7824$

The specific values used for each of the different tower steels are summarized in Table C–1. The 36 ksi and 42 ksi steels are materials used in the core columns and the remaining steels are used in the exterior columns. The resulting rate effects used in the constitutive modeling of tower steel based on Equation (5) are compared to the measured high-rate test data for the 50 ksi, 75 ksi, and 100 ksi tower steels in Fig. C–12. The comparison shows that the Cowper and Symonds model is capable of reproducing the rate effects for the range of data available.

Table C–1. Material constitutive parameter table–WTC tower steels.

Material Yield Specification	Young's Modulus	Poisson's Ratio	Strain-Rate Coefficient (C)	Strain-Rate Exponent (p)	Brick Element Failure Strain
36 ksi	29,700 ksi	0.288	7.900e+01	6.782	0.32
42 ksi	29,700 ksi	0.288	1.360e+05	6.782	0.32
50 ksi	29,700 ksi	0.288	4.220e+06	6.782	0.50
55 ksi	29,700 ksi	0.288	6.700e+06	6.782	0.64
60 ksi	29,700 ksi	0.288	3.950e+07	6.782	0.56
65 ksi	29,700 ksi	0.288	1.270e+08	6.782	0.51
70 ksi	29,700 ksi	0.288	1.270e+08	6.782	0.62
75 ksi	29,700 ksi	0.288	6.710e+08	6.782	0.56
80 ksi	29,700 ksi	0.288	2.440e+09	6.782	0.49
100 ksi	29,700 ksi	0.288	3.430e+09	6.782	0.53

Test results indicated that the influence of strain rate on the ductility of the tower steels did not follow a consistent trend. Several grades of steel had an increased ductility at high rates (more common for low strength steels), some had a reduced ductility at high rates (more common for high strength steels), and some showed no significant effect of strain rate on ductility. The approach used in the constitutive modeling is to ignore the changes in ductility produced by elevated strain rates. The effects of the variation of ductility over the expected range of strain rates will be assessed as part of the uncertainty analyses.

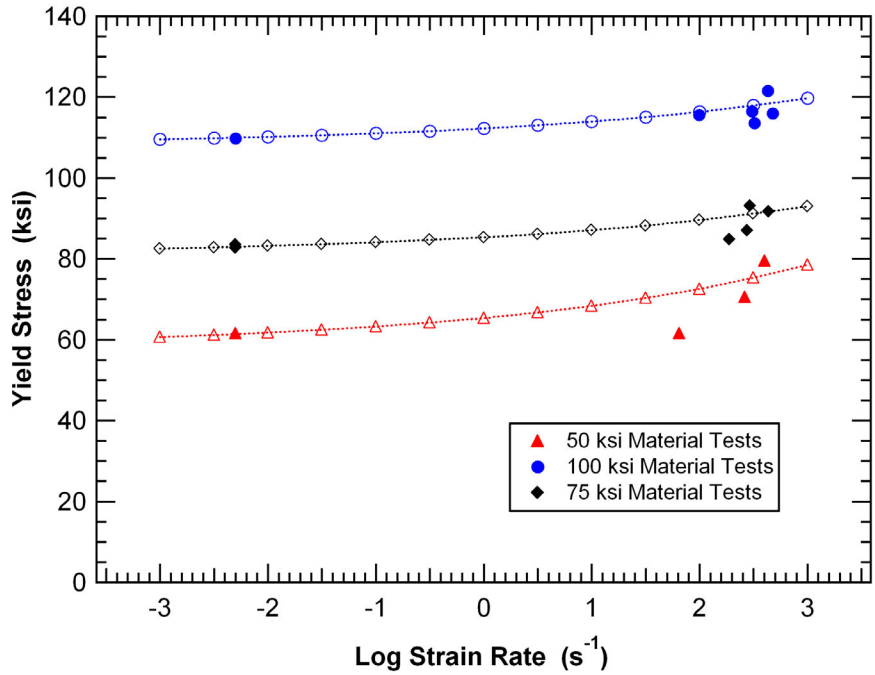

Figure C–12. Comparison of rate effects model and test data.

C.2.2 Failure Models

A challenge for calculating the aircraft impact response and damage to the WTC towers is the wide range of failure mechanisms that occur in both the aircraft and tower structures. These failures result from large scale deformations of the materials as well as from exceeding the strength of bolted, welded, and riveted connections. At the connection locations, complex behaviors are influenced by variations in material cross sectional geometry and material properties that produce large stress and strain concentrations.

The overall approach applied to modeling the impact damage and failure of the structures is to use engineering damage mechanics within the framework of the LS-DYNA finite element analyses. This analysis methodology is also referred to as local damage modeling and has been applied successfully in a wide variety of applications (e.g., Mudry 1985; Beremin 1983; Simons et al., 1999). Detailed fracture mechanics analysis of all the failures that occurred is beyond the scope of this project. The damage is calculated within each element in the impact simulations and damage development is based on local (element) quantities including plastic strain and stress state. When the specified failure criterion in an element is exceeded, the element is eroded (deleted) from the calculation. The erosion of elements allows for the propagation of failure through a structure.

Calculation of the failure of structural components is further complicated by the scale of the global impact analyses. Local damage modeling is often applied to the analysis of smaller components and failure initiation. In these applications, a relatively fine mesh can be applied, and damage regions around a local fracture can be resolved on a fine scale. For the global impact of an aircraft into a WTC tower, element sizes will have to be on average a few in. to maintain a model size at approximately 2 million to 3 million elements. At this resolution, the gradients around a fracture cannot be accurately resolved, and the damage criteria need to be adjusted to obtain the appropriate strength and ductility of the structures. In

the following subsections, various local damage modeling techniques applied to estimate failure of the aircraft and tower structures are described.

Mesh Refinement Effects

One of the significant modeling issues for the analysis of aircraft impact damage and failure is the effect of mesh refinement. The global impact analyses of the aircraft impacts into the WTC towers are very large analyses of complex structures and will require the refinement of the model to be reduced significantly from the detailed component analyses. As the mesh refinement is reduced, it is important to ensure that the damage mechanisms and extent of impact damage are properly captured.

A preliminary example of the effects of mesh refinement on the response was introduced earlier in the analysis of the material tests on the WTC tower steels. Figure C–1 showed both a fine mesh and a coarser mesh (referred to as medium mesh) version of the ASTM 370 rectangular tensile specimen for plate material. A comparison of the calculated necking behavior for two 75 ksi specimens immediately preceding failure is shown in Fig. C–13. The fine mesh is able to better resolve the strain gradients in the necking region and as a result has higher peak strain values at the same level of specimen displacement.

The effects of further reductions in mesh refinement required for global impact analyses can be demonstrated with the ASTM 370 tensile test example used in this section. The extreme limit for a coarse model of the tensile specimen would use a single shell element to model the entire specimen gage section. An example of coarse shell element model of the tensile specimen is shown in Fig. C–14. This coarse tensile specimen model would have a single stress and a single strain value for the gage section and does not have sufficient independent degrees of freedom to model the localization that occurs during necking. As a result, the critical plastic strain criterion for this single shell element model would be approximately equal to the engineering failure strain of 0.20 (see Fig. C–6).

The calculated engineering stress-strain behavior obtained with the three different mesh resolutions is shown in Fig. C–15. In these calculations, a maximum plastic strain criterion was used and the critical failure strain was shifted until each calculation failed at a value matching the average measured engineering failure strain. The corresponding critical plastic strains were 1.00 for the fine mesh resolution, 0.56 for the medium mesh resolution, and 0.18 for the coarse mesh resolution (shell element model).

The medium mesh resolution used in the above analysis of the tensile test corresponds to the mesh resolution applied in the exterior column component impact analyses described in Section C.4. Therefore, the critical failure strain of 0.56 would be carried forward to the detailed component analyses. The coarser shell element subassembly and global impact models are typically developed with shell elements and a resolution that might correspond to the coarse model shown in Fig. C–14. Therefore, the measured engineering elongation of the specimens is used for the critical strain. Additional modifications for regions with stress concentrations, such as along welds, is described later in this section.

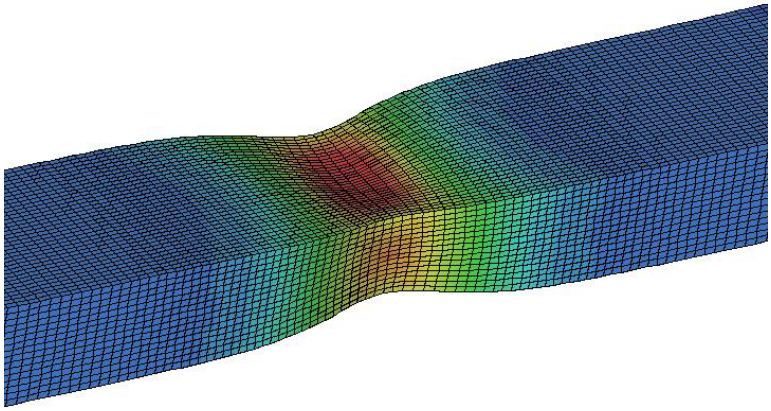

(a) Fine mesh necking behavior (red = 75 percent plastic strain)

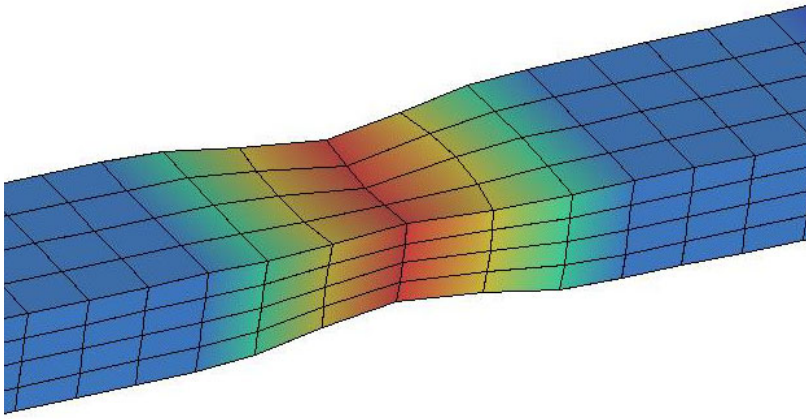

(b) Medium mesh necking behavior (red = 50 percent plastic strain)

Figure C–13. Calculated necking response in the 75 ksi tensile specimen.

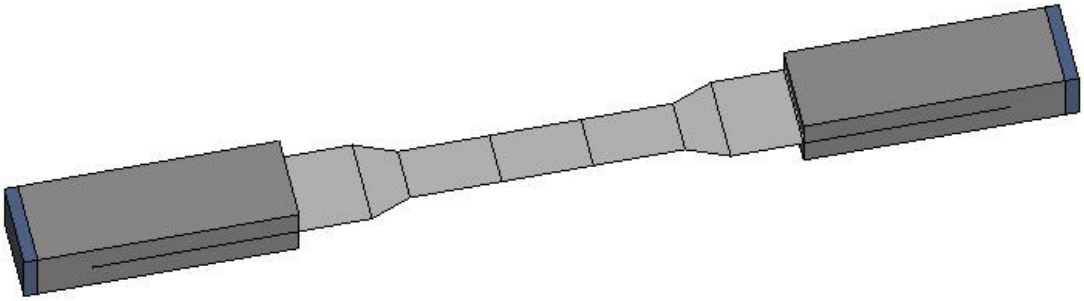

Figure C–14. Coarse shell element mesh for the 75 ksi tensile specimen.

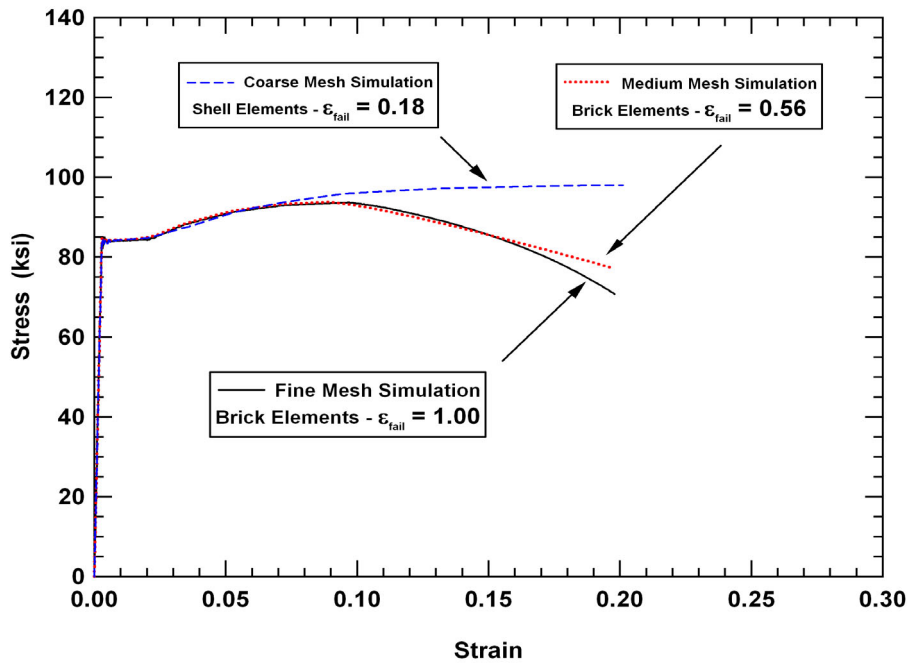

Figure C–15. Mesh refinement effects in the calculated 75 ksi tensile test.

Stress Triaxiality Effects

Using a local damage approach to model fracture with a damage model incorporating stress triaxiality effects has been successful in predicting the response and failure of welded steel structures to dynamic loads (Kirkpatrick, Giovanola, and Simons 1996). The strength of welded steel structures subjected to dynamic loads can be strongly influenced by the weld strengths and connection details. The following describes this approach to modeling fracture for impact damage to the WTC towers.

The damage analyses use a local damage approach within a finite element code to simulate the development of damage as the structure deforms. The fracture model is a simple form of a ductile fracture criterion (Mudry 1985). It assumes that failure of a material location occurs when the damage within a surrounding microstructural characteristic volume, V_{MIC}, exceeds a critical value. Mathematically, the damage function in the failure criterion can be written in the form:

$$D = \int \frac{d\varepsilon_{eq}^{p}}{\varepsilon_c(\sigma_{mean}/\sigma_{eq})} = 1 \qquad \text{over } V_{MIC} \approx (R_{MIC})^3 \tag{6}$$

where:

D = normalized damage parameter

$d\varepsilon_{eq}^{p}$ = increment in plastic strain

$\varepsilon_c(\sigma_{mean}/\sigma_{eq})$ = critical failure strain as a function of the stress triaxiality

The stress triaxiality is defined as the ratio of the mean stress to the equivalent stress.

This critical strain function can be determined by a series of notched tensile tests with specimens of varying notch radii (e.g., Mackenzie, Hancock, and Brown 1977). V_{MIC} is a characteristic volume of the material, which can be interpreted as the critical microstructural process zone. In turn, R_{MIC}, the representative linear dimension of the volume V_{MIC}, can be associated with microstructural dimensions such as grain size or spacing of the microvoid nucleating inclusions. R_{MIC} is therefore a constant length dimension that can be used to introduce a scaling effect in the fracture simulations. In its present form, the model does not account for a possible strain rate sensitivity of the damage growth and has been calibrated using static data for the failure strain as a function of stress triaxiality.

The damage function in Equation (6) provides the failure criterion based on the accumulation of damage over the history of the material. However, this damage law requires an appropriate definition of a critical failure strain function. In this type of model, the performance of the damage law is typically better if the form of the damage law has a physical basis from observations of the microstructural failure processes. Previous studies have shown that the rate of void growth in the ductile fracture process is an exponential function of the stress triaxiality (Rice and Tracey 1969) in the form:

$$\frac{dR}{R_o} = 0.28\, d\varepsilon_{eq} \exp\left[1.5(\sigma_{mean}/\sigma_{eq})\right] \tag{7}$$

This type of void growth law can be used to develop a critical strain function of the form:

$$\varepsilon_c(\sigma_{mean}/\sigma_{eq}) = \alpha \left\{ \frac{1.0}{\exp[1.5(\sigma_{mean}/\sigma_{eq})]} \right\} - \varepsilon_{shift} \tag{8}$$

where α and ε_{shift} are constants. The critical strain function in Equation (8), combined with the damage law in Equation (6), form the basis of the local fracture model.

The effect of stress triaxiality on damage development was measured by Project 3 for the core column steel materials using the specimen geometry shown in Fig. C–16. Only the core column materials were selected since the thickness of the components was sufficiently large to fabricate the notched round bar specimens. A series of 12 tests were performed using two different steel strengths and three different notch radii with a repeat test for each configuration. A summary of the notched round bar tests is given in Table C–2.

To determine the triaxiality in the three different notched round bar specimen geometries, models were developed of the specimens and the tests were analyzed. The models for the three different specimen geometries are shown in Fig. C–17. The models had a fine mesh (average element size of approximately 0.008 in.) capable of resolving the gradients in stress and strain across the specimen. It was found that the triaxiality and damage across the gage section is relatively uniform with a maximum along the axis of the specimen (failure is expected to initiate at the center of the specimen and propagate to the edges).

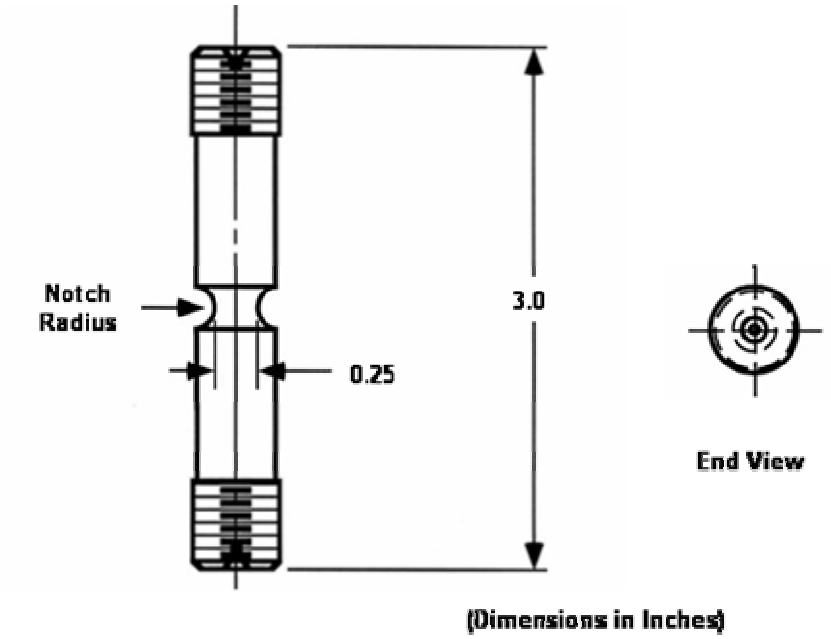

Figure C–16. Notched round bar specimen dimensions.

Table C–2. Summary of notched round bar tensile tests.

Specimen Number	Gage Dia. (in.)	Specimen Length (in.)	Notch Radius (in.)	Failure Dia. (in.)	Failure Strain	Stress Triaxiality
B6152-1-F1-1-1-05	0.2519	3.005	0.245	0.18646	0.2598	0.7
B6152-1-F1-1-1-06	0.2488	3.008	0.25	0.19223	0.2274	0.7
B6152-1-F1-1-2-01	0.2526	3.007	0.065	0.21466	0.1502	1.2
B6152-1-F1-1-2-02	0.2518	3.003	0.065	0.20518	0.1851	1.2
B6152-1-F1-1-2-03	0.2513	3.005	0.148	0.18571	0.2610	0.9
B6152-1-F1-1-2-04	0.2507	3.006	0.125	0.19837	0.2087	0.9
C71-1-F1-07	0.2506	3.005	0.245	0.19835	0.2085	0.7
C71-1-F1-08	0.2519	3.004	0.249	0.20325	0.1931	0.7
C71-1-F1-09	0.2487	3.005	0.125	0.21888	0.1199	0.9
C71-1-F1-10	0.2519	3.01	0.13	0.21818	0.1339	0.9
C71-1-F1-11	0.2514	3.005	0.064	0.23301	0.0732	1.2
C71-1-F1-12	0.2525	3.005	0.063	0.23919	0.0527	1.2

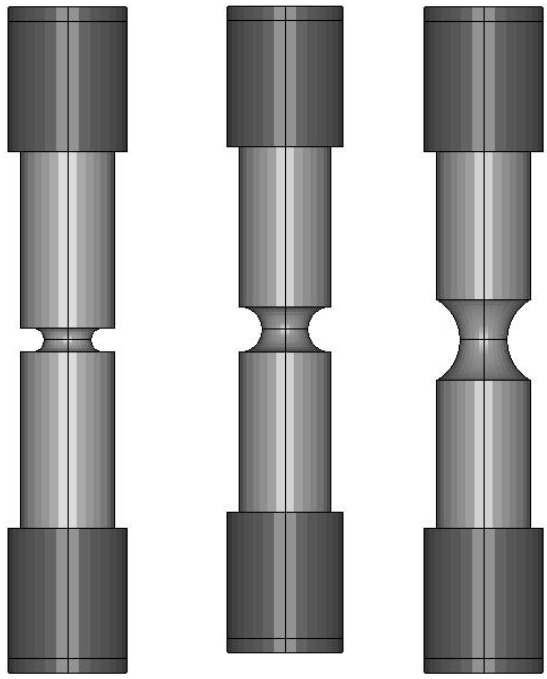

Figure C–17. Notched round bar tensile specimen models.

The calculated triaxiality at the specimen center as a function of damage, parameter D in Equation (6), for the three different notched round bar specimens is shown in Fig. C–18. The calculated responses for all three specimens show an initial spike in triaxiality and then settle to a constant stress triaxiality over a wide range of specimen deformation. The average value of triaxiality from these calculations is summarized in the last column of Table C–2.

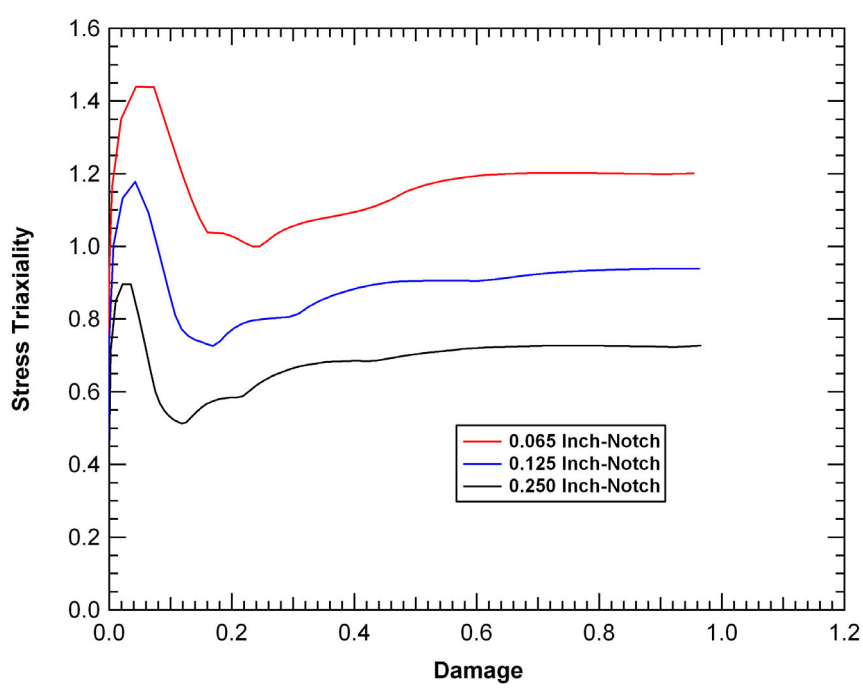

Figure C–18. Calculated notched round bar stress triaxiality.

A summary of the WTC steel notched round bar tests is shown in Fig. C–19. In addition, the figure shows failure criteria fit to the notched round bar data using Equation (8). For the WTC steels of interest, the presence of sulfide inclusions can be used to justify that the nucleation of voids occurs nearly instantaneously and ε_{shift} can be set to zero. The figure compares the C71-1-F1 tests with the failure criterion using a coefficient value α=0.5. Similarly the tests with the B6152-1-F1-1 steel (36 ksi yield) are compared to the failure criterion using a coefficient value α=0.90. Although neither set of material test is in perfect agreement with the failure criteria, the overall trends of the aggregate data set match and suggest that the form of the failure criteria is appropriate for the steels.

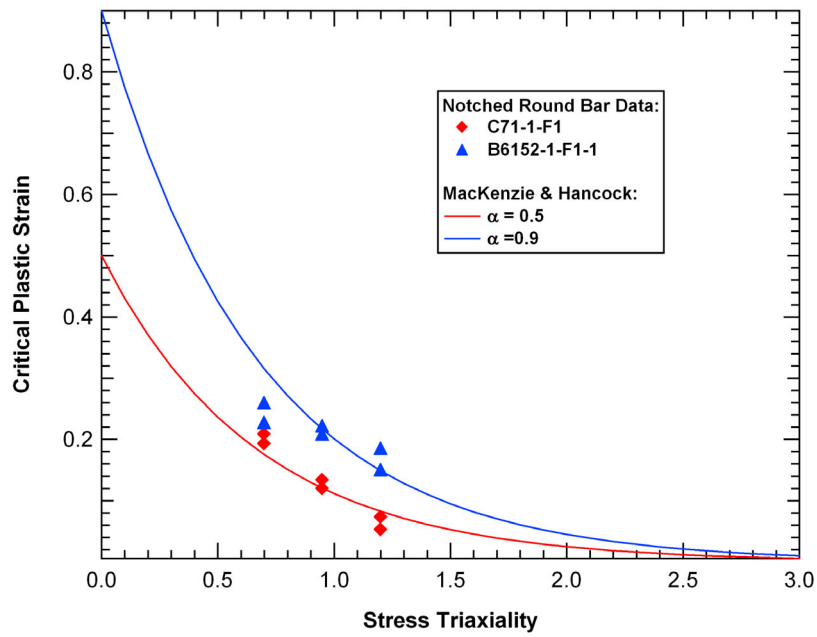

Figure C–19. Calculated critical plastic strain as a function of notched stress triaxiality.

A user-defined constitutive and failure model was developed and incorporated into LS-DYNA in this project. The model is identical to the piecewise linear constitutive model applied previously for the analysis of the WTC tower steels with the addition of the above stress triaxiality damage function incorporated. The simulations of the B6152 steel tensile and notched round bar tests were repeated with the user-defined constitutive model. The load-displacement relationships were compared to the previous analyses to validate the stress-strain relationships in the user-defined constitutive model. The calculated failure of the specimens is compared to the corresponding failure criteria in Fig. C–20. The agreement of the failure strains is a validation of the damage algorithm within the user-defined constitutive model.

In the following subsection, the user defined constitutive and damage model is applied to investigate failure of components in the WTC tower structure. A region of the WTC towers where the stress triaxiality is expected to be relatively high and play a role in the failure strength is the welded joints in the exterior column flanges and webs. This welded connection is analyzed below.

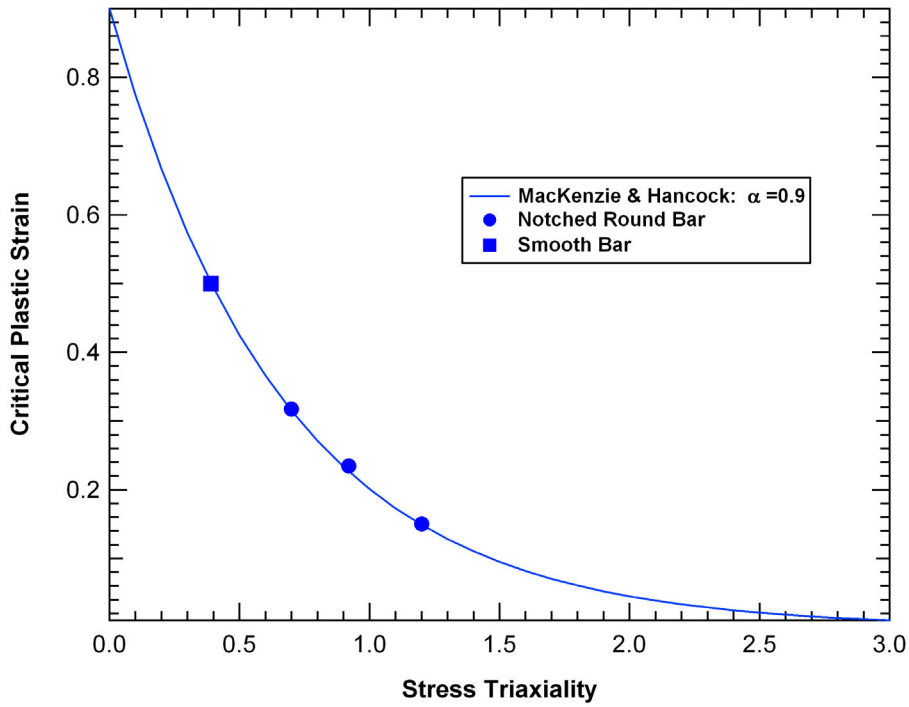

Figure C–20. Simulation of the notched and smooth round bar tests.

Weld Zone Constitutive Modeling

Photographs of the WTC towers immediately after impact, and inspection of the recovered exterior wall panels in the impact zone, have shown that failure along the weld zone was a characteristic feature of the impact damage. An example exterior column from the impact zone that has significant fractures along the weld zone for the outer web is shown in Fig. C–21. The amount of energy dissipated by these weld fractures is very small compared to the overall impact energy. As a result, the failure of the welds will have little effect on the subsequent damage to the interior structures and contents of the towers. However, to capture the damage mechanisms of the impacted exterior columns and to develop models and failure criteria for the global impact analysis, a failure model for the weld zone is required.

Modeling of the constitutive behavior for the weld and heat affected zone (HAZ) material is a challenging task due to the lack of significant material testing in these regions. To date, the data obtained on the weld properties consist of a micrographic characterization of an exterior column weld with microhardness indentation tests performed at various locations across the weld geometry. The specific weld geometry and microhardness characterization locations are shown in Fig. C–22. The corresponding hardness measurements across the base, HAZ, and weld materials are shown in Fig. C–23.

Figure C–21. Photograph of an exterior column with weld zone fractures.

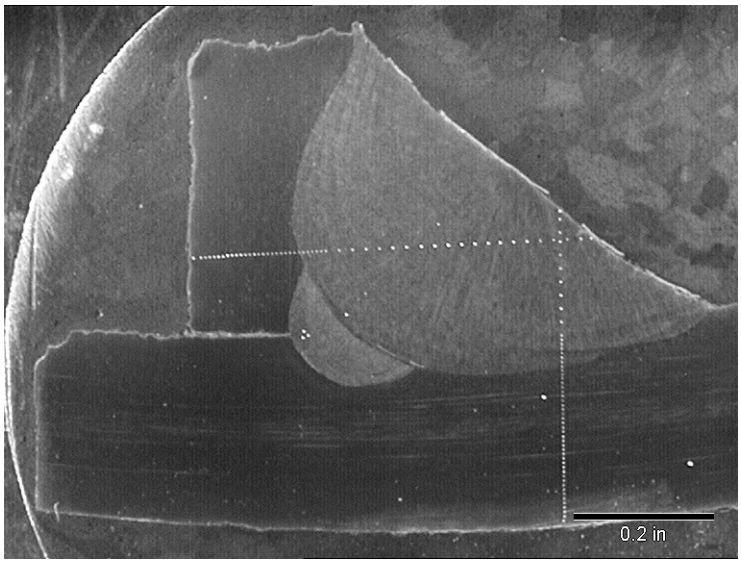

Figure C–22. Micrograph of an exterior column weld geometry.

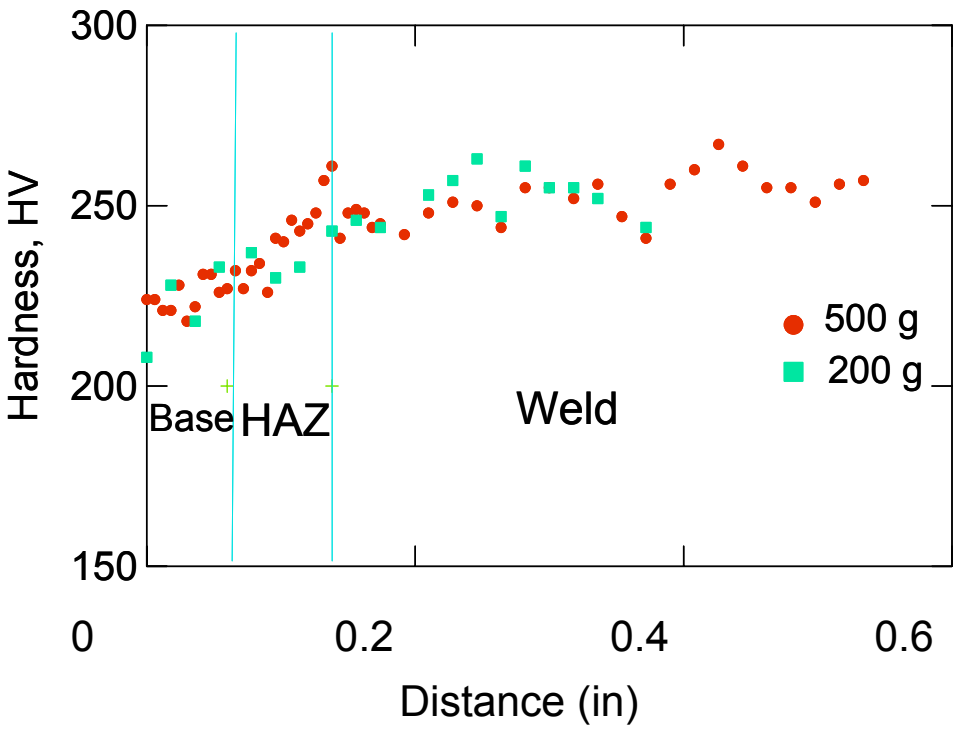

Figure C–23. Microhardness characterization of the weld and HAZ materials.

The microhardness measurements shown in Fig. C–23 were used to develop approximate plasticity behaviors for the weld and HAZ material regions. The approach used was to use the base material constitutive behavior and shift the flow stress of the HAZ and weld materials by 12 percent and 18 percent, respectively. These shifts correspond to the relative magnitude of the average measured hardness in each material region.

Analyses were performed to investigate the weld failure behavior using a detailed model of a simplified two-dimensional (2-D) weldment geometry representative of an exterior column side flanges and welded outer web as shown in Fig. C–24. A short duration pressure load is applied across the front web to introduce a dynamic loadcondition on the welded connection. The boundary conditions were approximated by fixing the displacements at the top and bottom of the side plates, seen in Fig. C–24 (b). The entire model is constrained to a plane strain condition. The weldment model includes weld and HAZ regions as shown in Fig. C–24 (c).

The base metal for the weldment is the 55 ksi steel. An approximate damage criterion was developed for the steel based on the results of the tensile tests on the material. The criterion is that of Equation (8) with a coefficient value α=0.92. This value was obtained by using an approximate value for the average triaxiality of the tensile specimen and the failure strain obtained from the previous analyses of the tensile tests described earlier in Section C.2.1. The estimate of the average triaxiality is approximate since the triaxiality is changing in the region of the necking prior to failure. The user-defined constitutive model with this estimated damage model was used to simulate the tensile test. The comparison to the data and previous analyses is shown in Fig. C–25. The approach underestimated the engineering failure strain by approximately 10 percent.

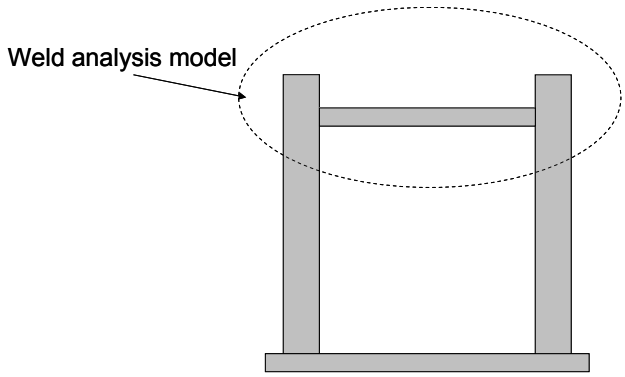

(a) Cross section of an exterior column

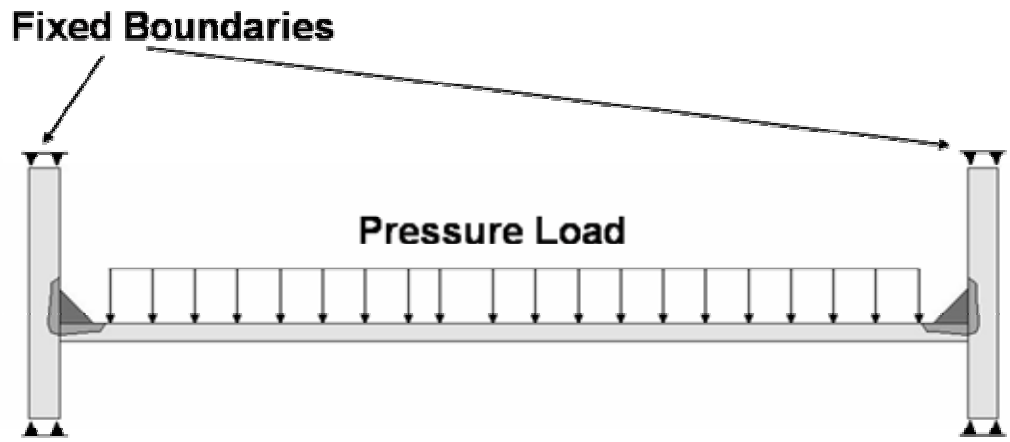

(b) Weld analysis model

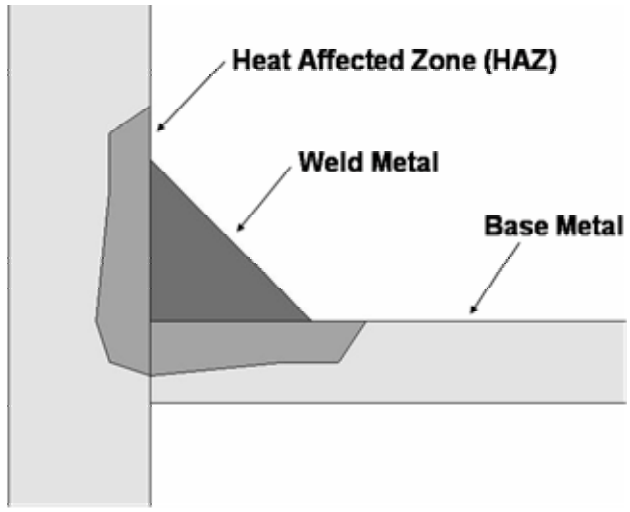

(c) Weld region detail

Figure C–24. 2-D weldment model developed for analysis of failure behavior.

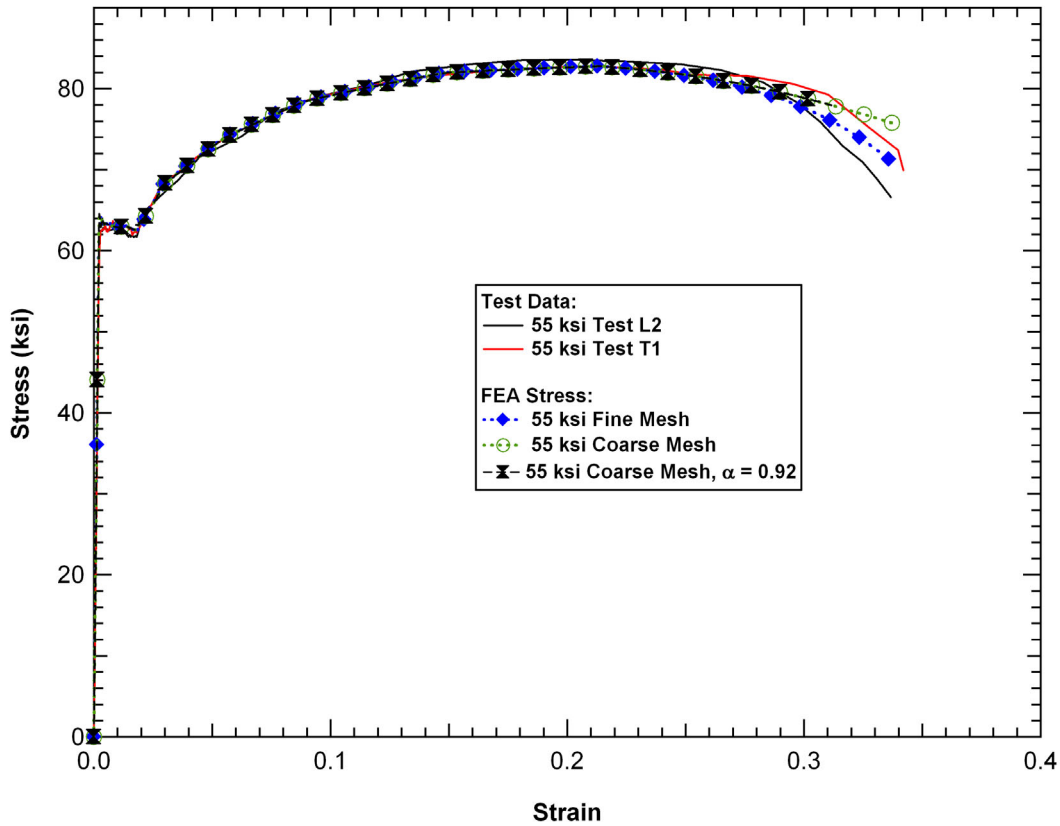

Figure C–25. Simulation of the 55 ksi steel tensile test.

Two different mesh refinements were developed for the weldment model as shown in Fig. C–26. The model developed using the fine mesh has 10,240 solid brick elements, as shown in Fig. C–26 (a). The fine mesh model should have sufficient resolution to capture the gradients in stress and strain around the weld and HAZ. The model developed using the medium mesh has 702 solid brick elements, as shown in Fig. C–26 (b). This model was developed with a mesh refinement that could be applied to a three-dimensional analysis of a column for component impact analyses.

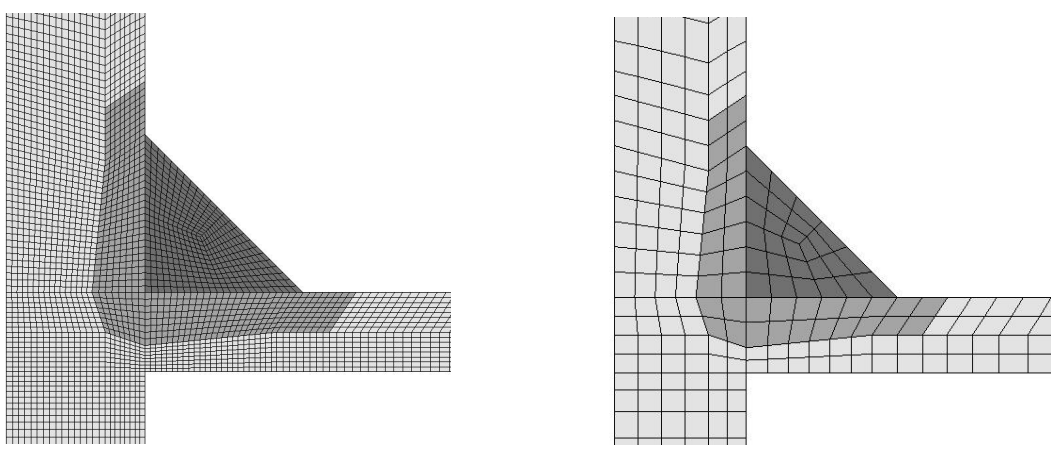

(a) Fine mesh resolution **(b) Medium mesh resolution**

Figure C–26. Mesh resolutions used in the 2-D weldment failure model.

An example fracture analysis of the weldment model using the fine mesh model is shown in Fig. C–27. The loading was provided by a rectangular pressure pulse with 0.10 ms duration and amplitude of 38 ksi (262 MPa). The failure initiates at the toe of the weld and propagates through the heat affected zone and outer web plate. This is the most common weld failure mode observed in the recovered WTC exterior columns. The pressure load results in a downward velocity of the front web. The motion at the ends of the web is restrained by the welds at the flanges and a moving plastic hinge behavior develops in the web. The deformations result in bending and tension at the weld location and eventually the local deformations initiate a fracture at the toe of the weld that propagates through the HAZ and web base metal. The details of the calculated fracture behavior are shown in Fig. C–28.

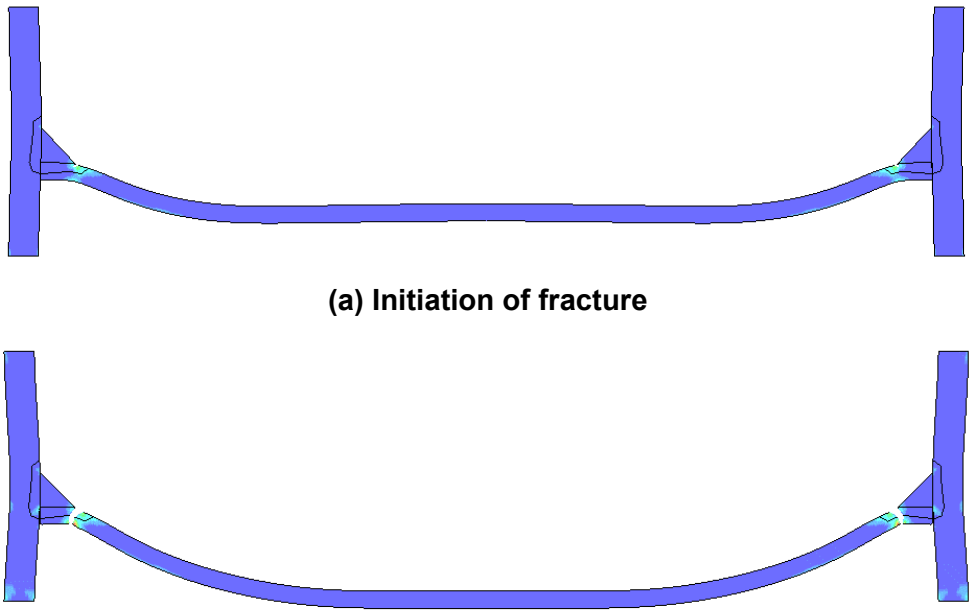

(a) Initiation of fracture

(b) Complete fracture through the web

Figure C–27. Calculated weldment deformations and failure.

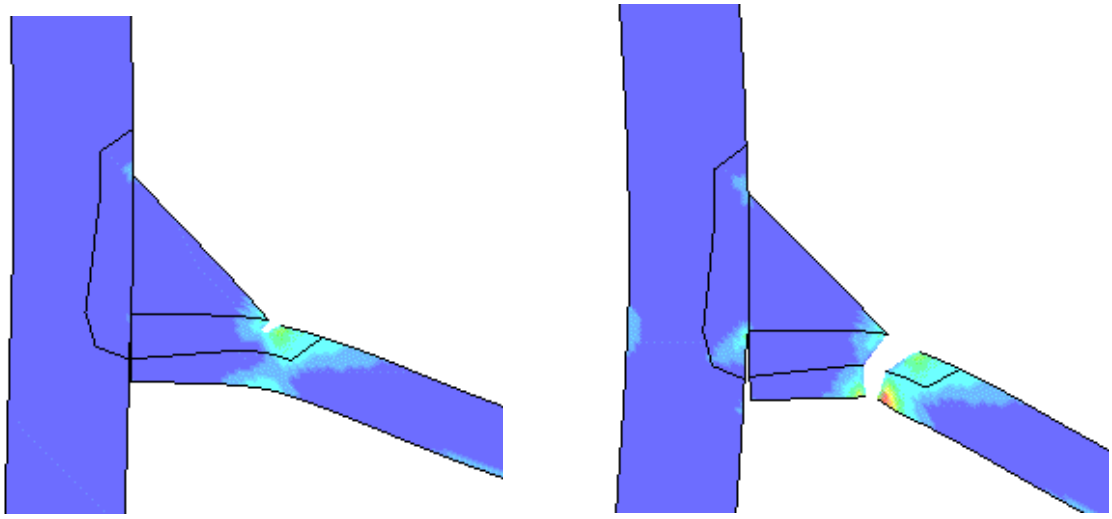

(a) Initiation of fracture **(b) Complete fracture through the web**

Figure C–28. Detail of the calculated weldment failure behavior.

As described in previous analyses, the application of a coarser mesh resolution does not resolve the same gradients in stress and strain and the failure criteria need to be adjusted. The failure criteria parameters used in the two analyses are given in Table C–3. The comparison of the fracture behavior for the two mesh resolutions is shown in Fig. C–29. Similarly the kinetic and internal energies for the two calculations are compared in Fig. C–30. The comparisons show that both models have the same deformation and failure modes at very similar energy levels.

Table C–3. 2-D weldment model comparison.

Mesh Refinement	Fine	Medium
Element class	Brick	Brick
Base metal failure coefficient (α)	1.35	0.76
HAZ metal failure coefficient (α)	0.81	0.45
Weld metal failure coefficient (α)	1.10	0.62

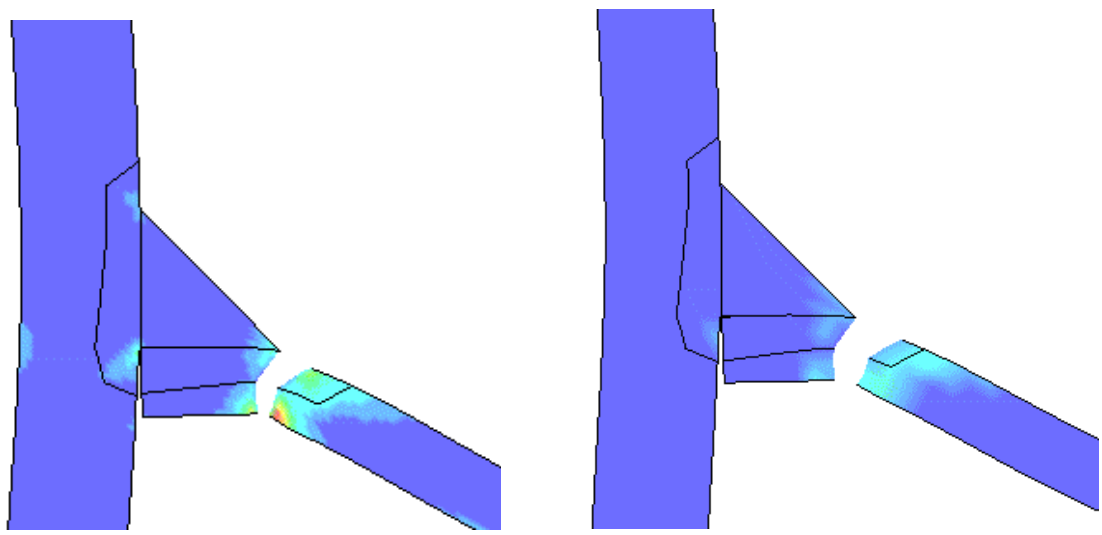

(a) Fine mesh resolution **(b) Medium mesh resolution**

Figure C–29. Mesh refinement effects on calculated weldment failure behavior.

The remaining stage in developing the weldment failure model is to perform three-dimensional component impact analyses of the exterior column and develop a coarser shell element description of the weld region that can be applied in the global aircraft impact analyses. The problem analyzed is the drop test configuration shown in Fig. C–31. The drop test configuration shown has a 550 lb steel impactor with an impact velocity of 37.4 mph. The impactor is 12 in. wide and 5 in. across. The nose of the impactor has a reduced area that is 12 in. wide and 2 in. across with a one-half in. radius rounded edge around the impact face. The length of the column section represents a portion of an exterior column between spandrels.

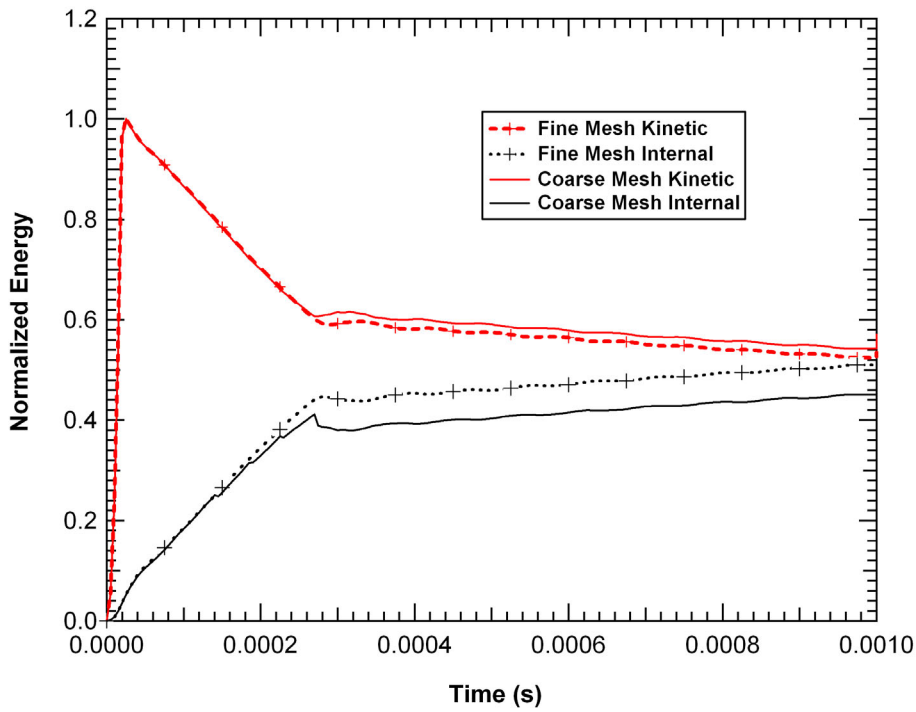

Figure C–30. Calculated energy balance for the 2-D weldment models.

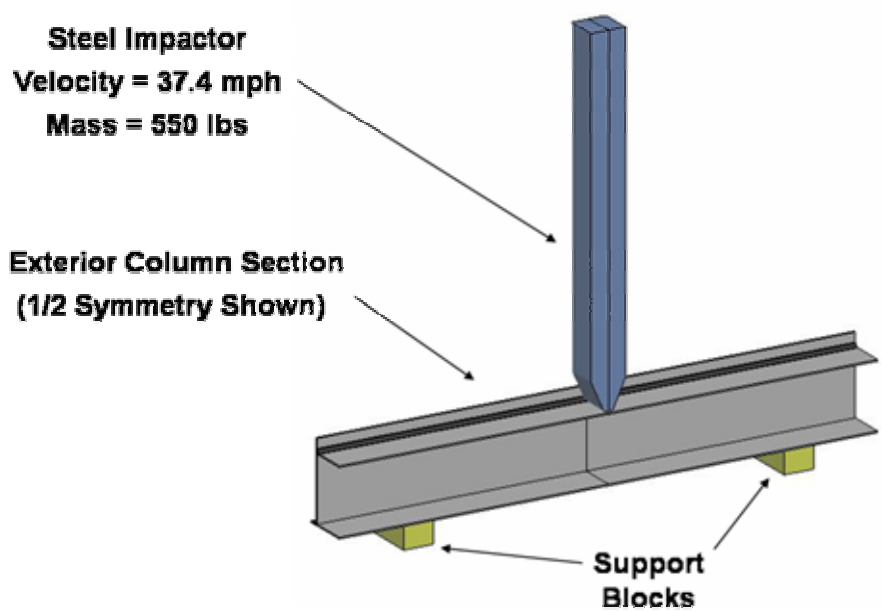

Figure C–31. Drop test model for column weld fracture analysis.

The two different column and weld models applied are shown in Fig. C–32. The medium mesh resolution was previously applied in the 2–D weldment fracture analyses. The half symmetry medium mesh column model contained 63,680 brick elements. The coarse shell element model has significantly fewer elements with approximately 4 in. elements to define the column and 1 in. wide elements in the weld zone. The

half symmetry coarse shell element column model contained 144 linear shell elements. Obviously, the coarse shell element model is not capable of capturing the stress and strain gradients to the same extent as the brick element model. As a result, the shell element model applies the simpler critical plastic strain criterion available in the default piecewise linear constitutive model.

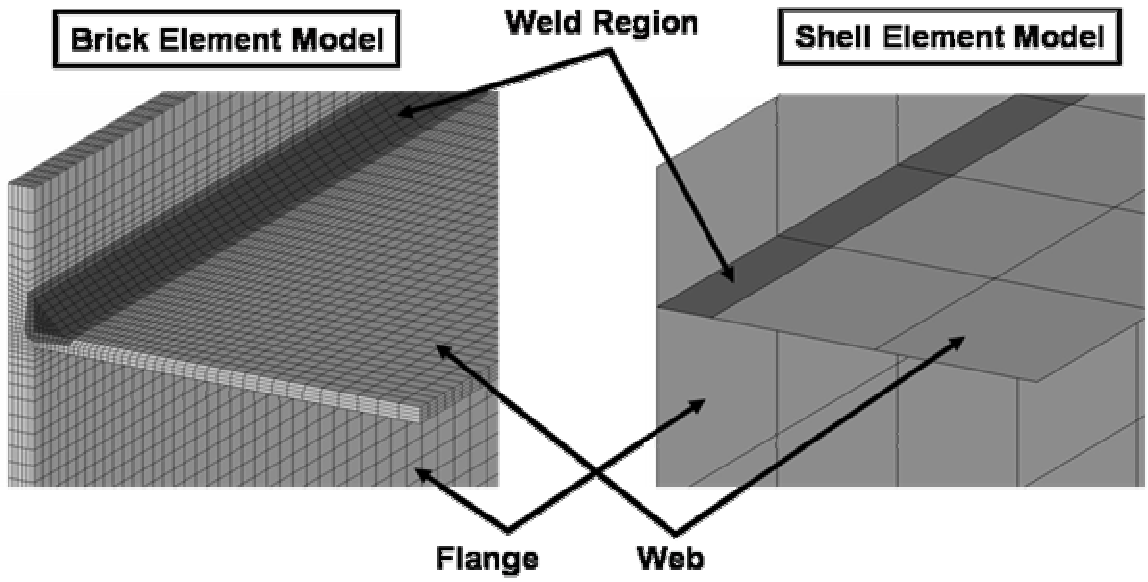

(a) Medium mesh resolution **(b) Coarse mesh resolution**

Figure C–32. Models developed for column weld fracture analysis.

The drop test was simulated first using the medium resolution brick element model. The results of the calculated impact response and failure were then used to develop an appropriate failure strain for the shell element model weld zone. The strain profile calculated in elements along the upper surface of the web in the weld fracture region is plotted in Fig. C–33. The figure shows a strong gradient in the calculated strains with the peak strains of approximately 15 percent plastic strain near the toe of the weld. A corresponding critical strain of 8 percent was selected for the corresponding one-in.-wide single shell element weld zone. This strain is indicated by the red line in Fig. C–33.

The comparison of the resulting impact behavior for the two models is shown in Fig. C–34. Both models have similar impact deformations and the lengths of the weld failures are in good agreement.

These analyses have been used to develop improved engineering fracture criteria in the weld region. There is still significant uncertainty in the details of the weld geometry and damage development in the weld region with variations in material properties and stress distributions. However, reasonable bounds on the effects of these variations will be assessed later in the uncertainty analyses.

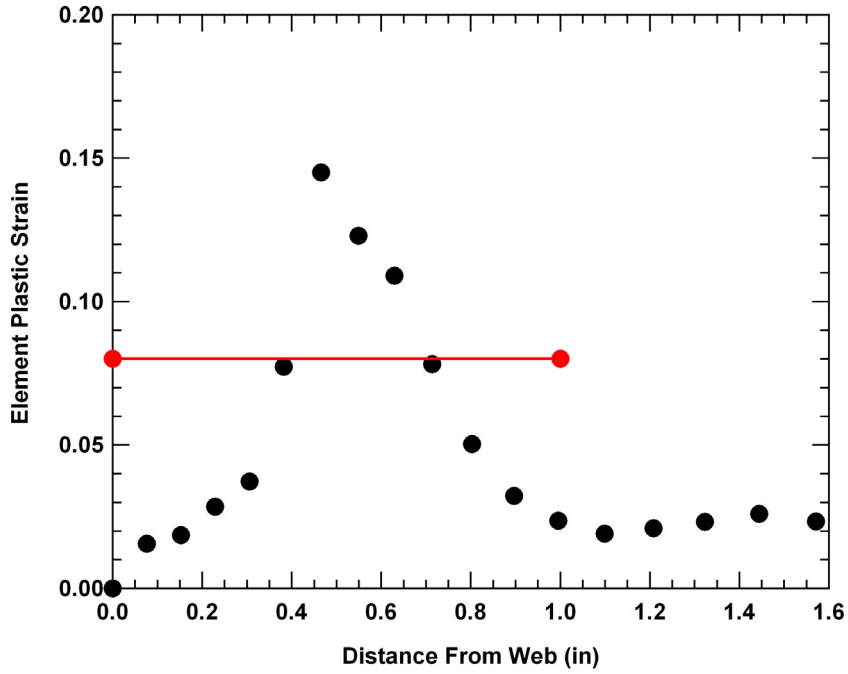

Figure C–33. Calculated strain profile for the weld zone.

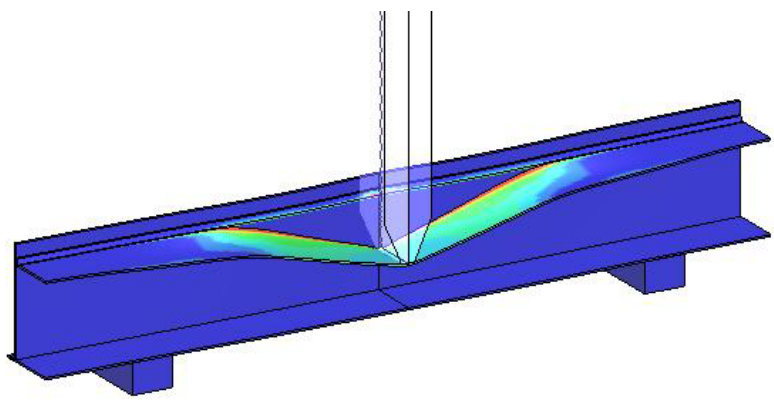

(a) Medium resolution brick element model

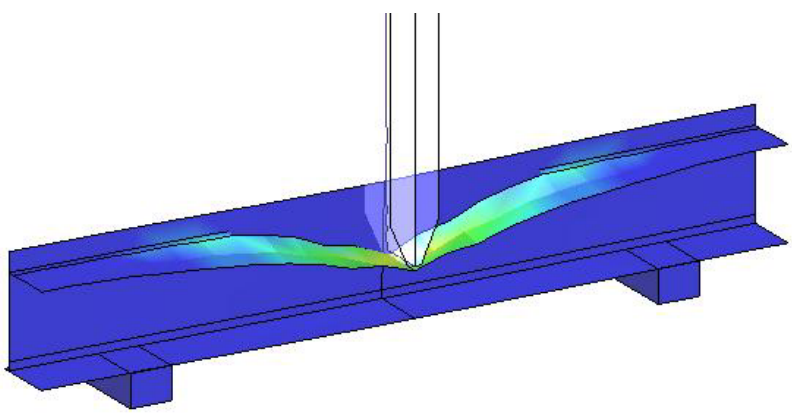

(b) Coarse resolution shell element model

Figure C–34. Calculated drop test fracture behavior.

Bolt Material Constitutive Modeling

The primary bolts of interest for the impact analysis are those used at the connections between the exterior columns on the WTC towers. Within the impact zone, the connections are typically made using 0.875 in. in diameter steel bolts grade A325. Initially, there was no test data available that could be applied to develop a bolt model. The modeling approach was to develop a brick element bolt model and use it to develop a corresponding beam element bolt model for the majority of the impact analyses. A description of these bolt analyses are given in Section C.4.2, along with the component analyses.

Subsequently, a series of tests was performed by Project 3 on bolts recovered from the WTC towers. A summary of the bolt testing is given in Fig. C–35. The bolts were found to yield at a load of approximately 50 kip and have an ultimate failure load of approximately 68 kip. The measured elongation at failure is approximately 0.18 in.

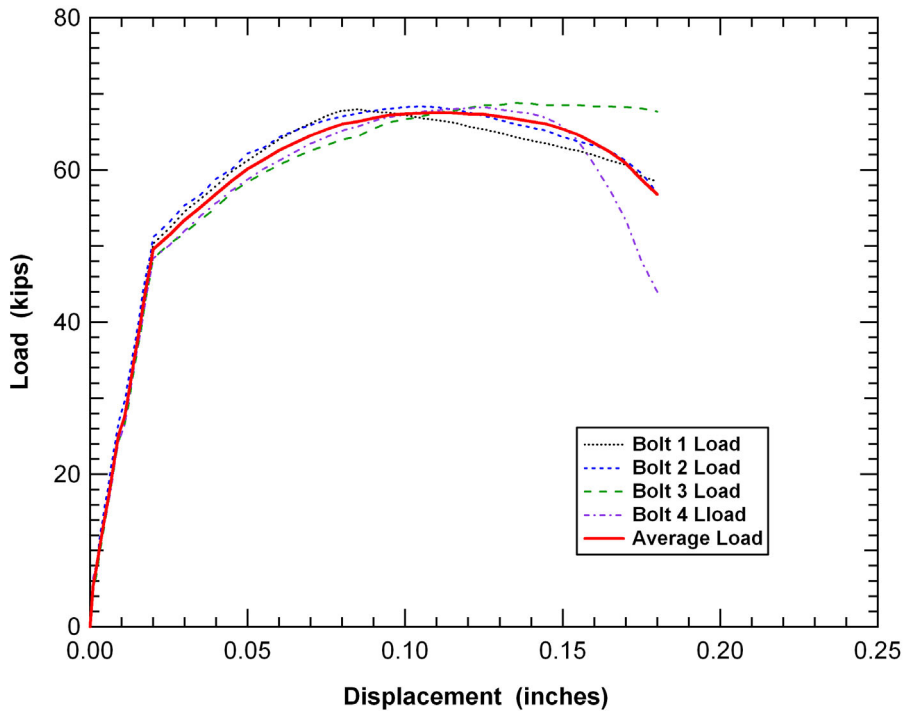

Figure C–35. Measured bolt load-displacement behavior.

The beam element model for the bolt, described in Section C.4.2, was compared to the bolt test data. The comparison showed good agreement in the strength of the bolt, but it also indicated that the beam model overestimated the ductility. This may be a result of not capturing the details of the stress concentrations in the region of the threaded connection and nut. The bolt test data was used to correct the ductility of the beam element bolt model and the resulting comparison of the model and data is shown in Fig. C–36. The bolt model shows a bilinear elastic-plastic behavior that is stiffer in the elastic region and yields at a higher stress level than the data. The inability of the simplified model to capture stress gradients in the regions of the bolt head, threads, and nut may cause this type of response. However, the overall strength and ductility of the model and test data as well as the strain energy capacity agree reasonably well that further model development was not required.

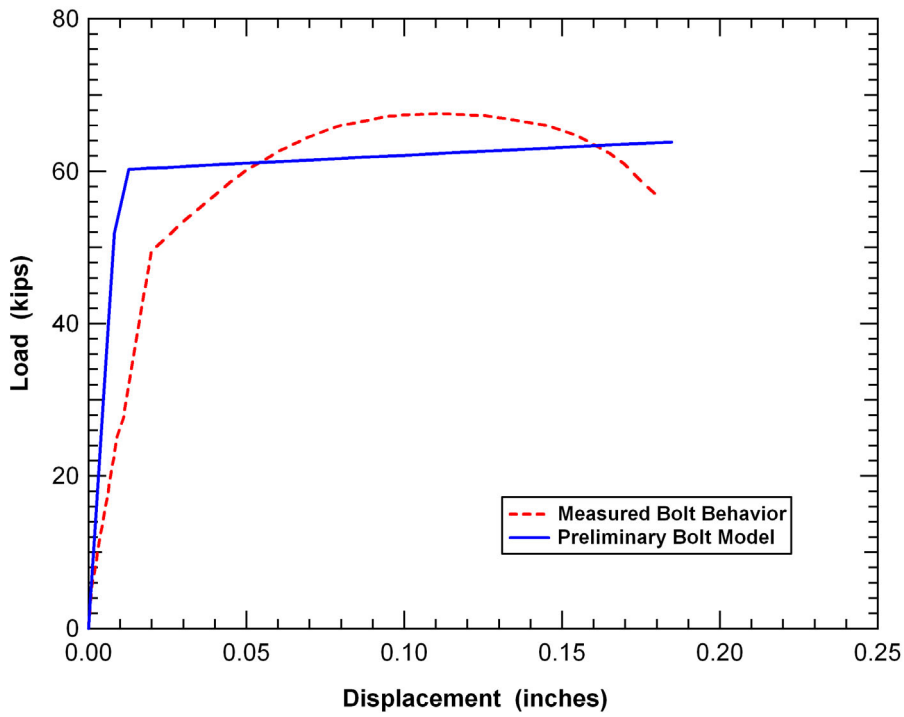

Figure C–36. Comparison of the measured and calculated bolt behavior.

C.2.3 Concrete Constitutive Models

There are several concrete models in LS-DYNA. Each has different capabilities for modeling rate effects and nonlinearity associated with damage and failure behavior. Potential concrete models in LS-DYNA are Types 5 (soil and crushable/non-crushable foam model), 16 (pseudo-tensor concrete model), 25 (kinematic hardening cap model), 78 (soil and concrete model), and 111 (Holmquist-Johnson-Cook concrete model). An important factor in determining the behavior of a concrete structure in compression or bending is its lateral confinement. The concrete floor slabs in the WTC towers were not highly confined so a material model suitable for this loading condition is needed.

In this study, the ability to accurately model the low confinement damage and softening behavior is important. Damage caused by cracking in the concrete degrades the strength in the low confinement regime. Inclusion of this damage growth provides a more accurate representation of the stress-strain response. Based on this capability, the LS-DYNA material Type 16 (pseudo-tensor concrete model) is selected for modeling the concrete floor slabs. This model also accounts for the high strain-rate sensitivity of reinforced concrete.

As implemented in LS-DYNA, the pseudo-tensor model can be operated in two major modes: (1) a simple tabular pressure-dependent yield surface, and (2) a model with two pressure-dependent yield functions and a damage-dependent function to migrate between curves. The first option is well suited for implementing standard geologic material behaviors such as a Mohr–Coulomb yield surface with a Tresca limit and has been used successfully for the analysis of ground shock and soil-structure interactions under high confinement. The second option, applied here, allows for implementation of tensile failure and damage scaling, which are more dominant material behaviors at low confinement.

The pseudo-tensor model, as applied to the analysis of the lightweight concrete in the WTC towers, has two pressure-dependent yield functions. By defining suitable yield functions for the undamaged and fully damaged concrete and an appropriate tabular interpolation between the curves, the behavior of the damage under low confinement can be properly captured.

Material constitutive parameters for the pseudo-tensor model were developed for a 3 ksi compressive strength lightweight concrete. A simulation was performed of a standard unconfined concrete compression test to check the constitutive model behavior. The simulated behavior of the concrete specimen is shown in Fig. C–37. The calculated compressive stress-strain response is compared to measured compression data for 2.3 ksi and 3.8 ksi strength concretes in Fig. C–38 (Wischers 1978). Currently, the same material parameters are being used for the concrete in both the core (normal weight concrete) and truss floor (lightweight concrete) areas.

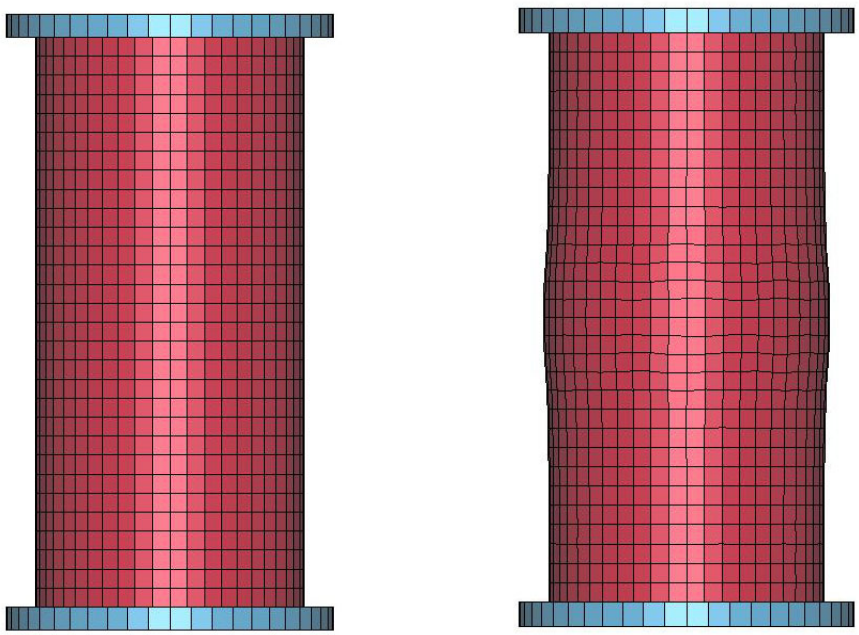

Initial Configuration **2 % Compression**

Figure C–37. Finite element analysis of the unconfined compression test.

C.2.4 Aircraft Constitutive Models

No material testing was performed to characterize the structural materials in the aircraft or develop the constitutive model parameters for these materials. Therefore, the constitutive and failure properties for the aircraft materials were developed from data available in the open literature. The principal sources of data for the airframe materials are the Military Handbook (MIL-HDBK-5F), 1987 and Aerospace Structural Metals Handbook (Brown et al. 1991). Additional sources of data are used to verify and supplement the information obtained from these primary data sources.

Complete engineering stress-strain curves were provided in the MIL-HDBK-5F for various 2024 and 7075 aluminum alloys that are commonly used in the construction of the 767 airframe structures. These

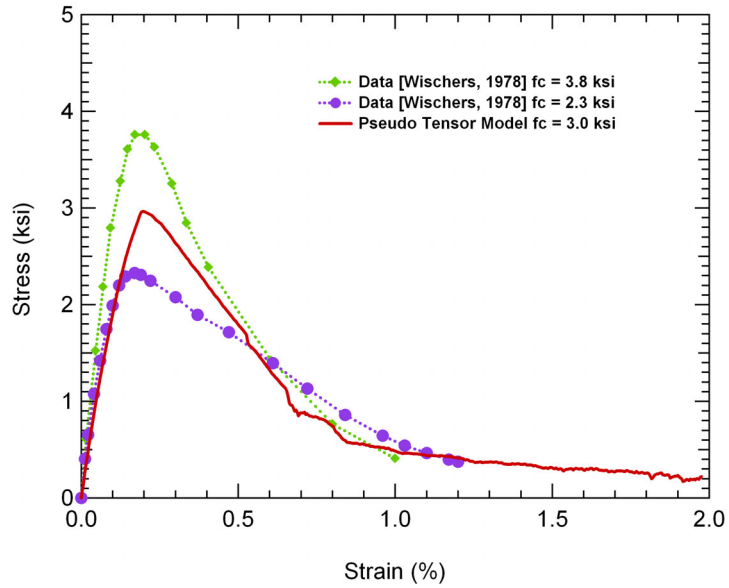

Figure C–38. Comparison of the calculated unconfined compression behavior with concrete compression test data.

curves were digitized for the various 2024 and 7075 alloys as shown in Fig. C–39 and Fig. C–40, respectively. Representative stress-strain curves were then converted into true stress and true strain as described earlier and used to develop tabular curves for constitutive models. The calculated true stress-strain curves and tabular constitutive model fits are shown in Fig. C–41 and Fig. C–42, respectively.

C.3 DEVELOPMENT OF AIRCRAFT MODEL

Development of the model of the Boeing 767-200ER aircraft is being accomplished through a three-step process. These are data collection, data interpretation and engineering analysis, and finally meshing of the structure. Data collection is nearing completion, and additional efforts will mainly focus on final details of non-structural contents and material properties for primary structural parts. Reviewing, organizing, and analyzing the data as well as meshing of the structure are also at the final stages.

C.3.1 Aircraft Data Collection

Data collection for the Boeing 767-200ER is nearing completion. Significant information on the aircraft structure and contents has been gathered from (1) documentary aircraft structural information, and (2) data from measurements on Boeing 767 aircraft.

C.3.2 Description of the Aircraft Model

The model for the Boeing 767-200ER is nearing completion. Certain components, such as the PW4000 engine shown in Fig. C–43, have been completed. Construction of the wings is in the final stage with only the inboard flaps and ailerons left to be modeled. Work has begun on the fuselage as well. Some details of the airframe model are shown in Fig. C–46 later. The LS-DYNA model of the aircraft is generated and meshed using the TrueGrid software (TrueGrid Manual 2001).

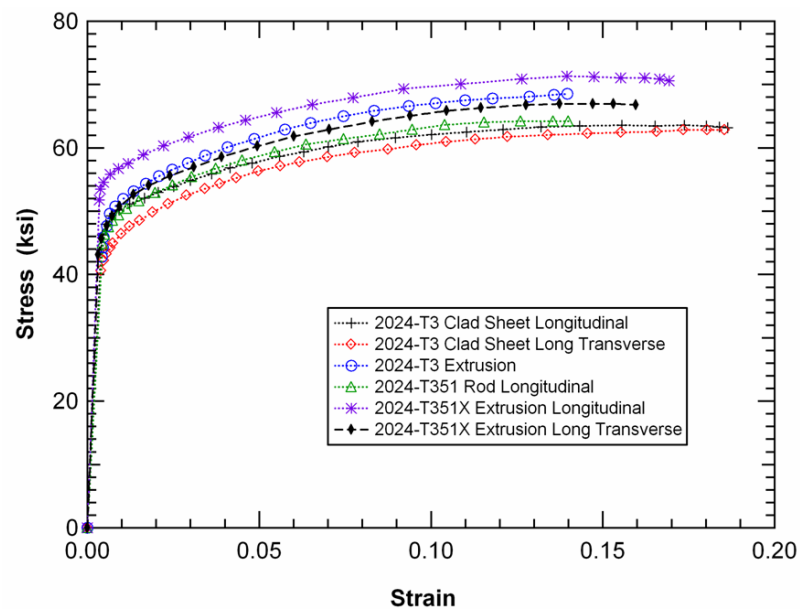

Figure C–39. Digitized engineering stress-strain curves for various 2024 aluminum alloys.

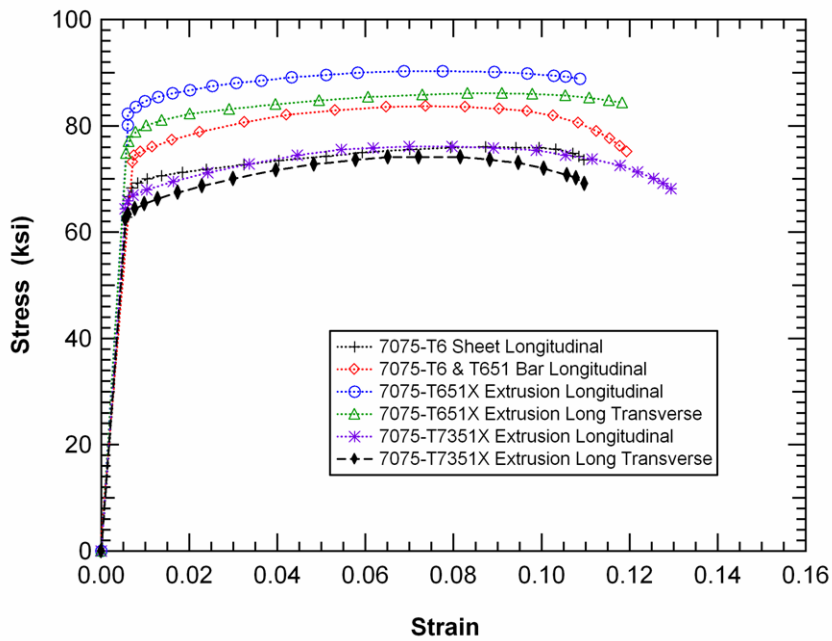

Figure C–40. Digitized engineering stress-strain curves for various 7075 aluminum alloys.

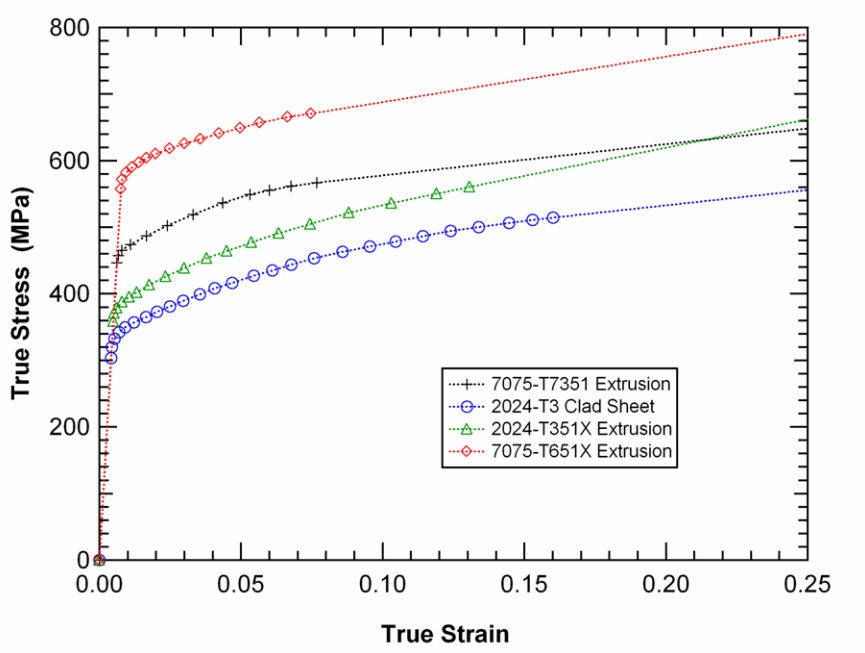

Figure C–41. True stress-strain curves developed for various aircraft aluminum alloys.

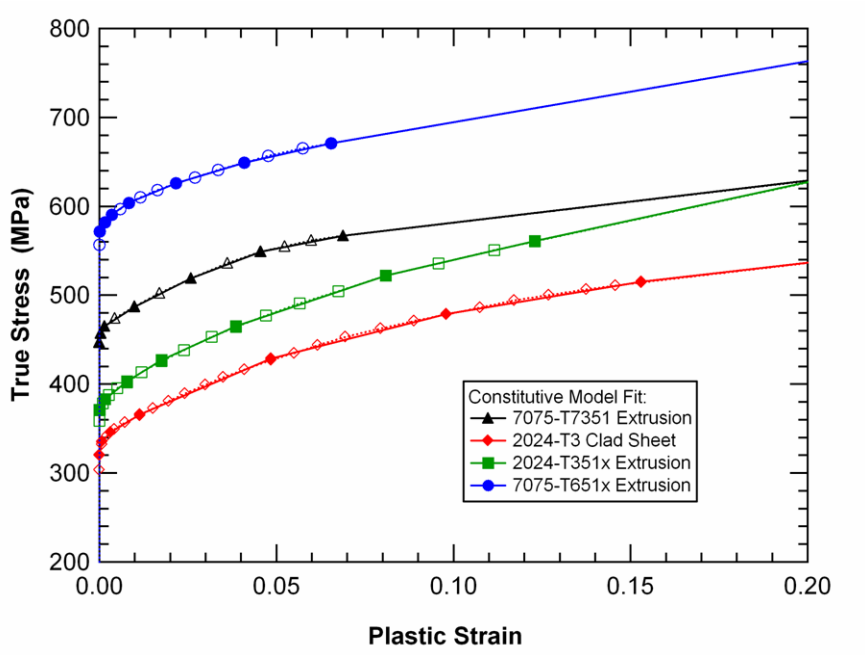

Figure C–42. Tabular true stress-strain curves developed for various aircraft aluminum alloys.

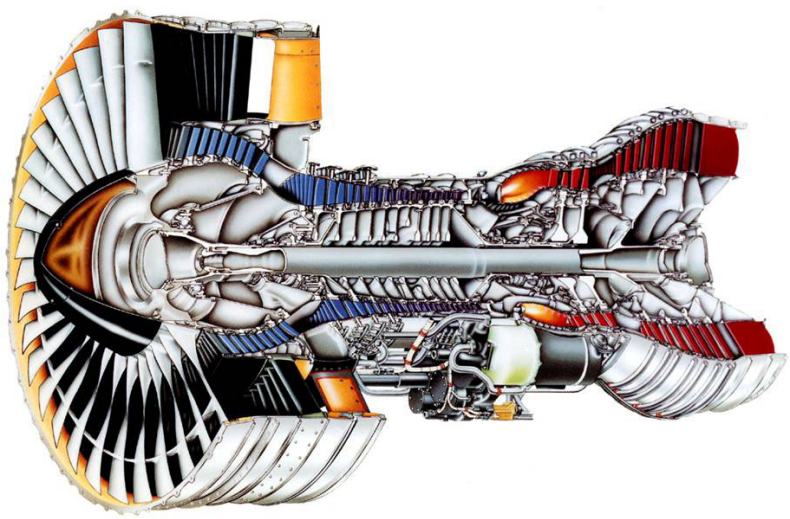

Figure C–43. Pratt and Whitney PW4000 turbofan engine.

Engine Model Development

The Pratt and Whitney PW4000 turbofan engine has a very complex structure as shown in Fig. C–43. The engine is an important component of the aircraft with the potential to produce significant impact damage to the WTC tower structures (e.g., fail core columns). As a result, special care was given to the development of the engine model to include all the details of the engine construction.

To develop a structural model of the engine, the primary structural components in the engine were identified and approximated with simplified geometry as illustrated in Fig. C–44. Known engine dimensions were used to determine the scale factor for the drawing. The simplified geometry of the engine structures could then be captured using a common digitization procedure. Once the engine's internal geometry was captured, the digitized geometry was imported into TrueGrid and used to generate surface definitions and part geometries for the engine model. The engine model was developed primarily with shell elements. The objective was to develop a mesh with typical element dimensions between one and two in. However, smaller element dimensions were required at many locations to capture details of the engine geometry. Brick elements were used for some of the thicker hubs and the roots of the compressor blades. The various components of the resulting engine model are shown in Fig. C–45. A summary of the elements used in the engine model is given in Table C–4.

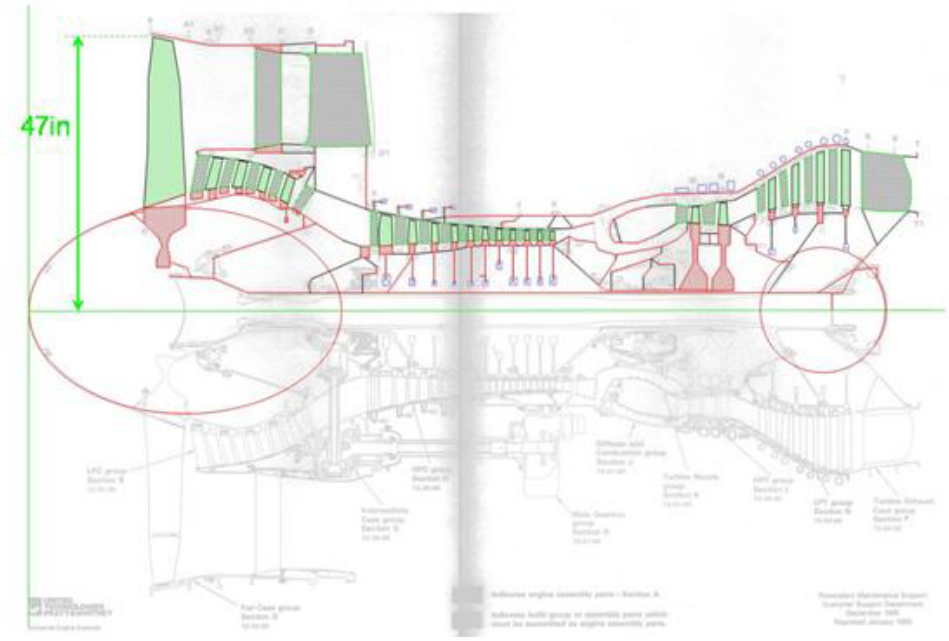

Figure C–44. PW4000 engine cross sectional geometry and simplification.

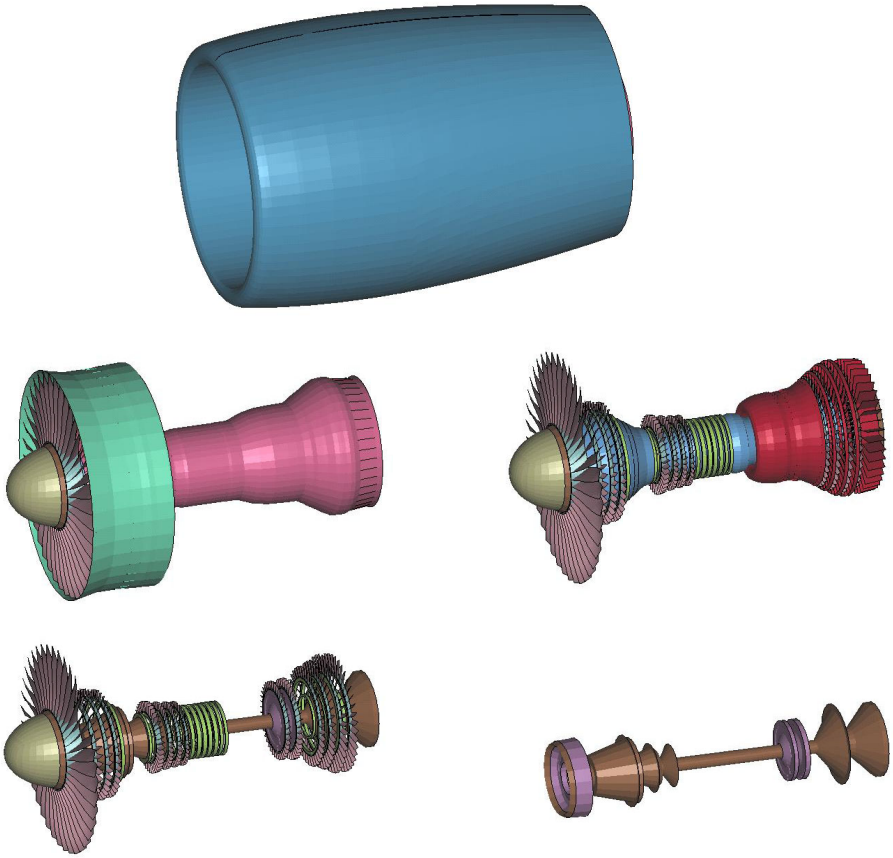

Figure C–45. Pratt and Whitney PW4000 turbofan engine model.

Table C–4. Engine model parameters.

	PW4000 Engine Model
Number of brick elements	9,560
Number of shell elements	54,788
Total nodes	101,822
Preliminary engine model weight	7,873 lb (3,571 kg)
Adjusted engine model weight	9,447 lb (4,285 kg)

After the known structural components of the engine were included in the engine model, the weight of the model was calculated at 7,873 lb (3,571 kg). The dry weight of the PW4000 engine is listed at 9,400 lb. The difference in weight potentially results from the nonstructural components (tubing, pumps, seals, bearings, etc) that were not captured in the model. To account for the difference, the density of all of the material models used for engine components was increased by 20 percent. This effectively smears the missing mass in proportion to the original mass distribution in the model. The resulting adjusted engine model mass is 9,447 lb (4,285 kg).

Information available from the Aviation Safety Network (http://aviation-safety.net/) indicates that American Airlines Flight 11 was powered by two General Electric CF6-80A2 engines, while United Airlines Flight 175 was powered by two Pratt and Whitney JT9D–7R4D engines. Review of these engines indicates that the PW4000 turbofan engine is very similar to the General Electric CF6-80A2 and the PW JT9D-7R4D engines. Comparisons of specific physical characteristics of the engines are given in Table C–5. In fact, the JT9D-7R4 and PW4000-94 are almost identical as they are in the same family of Pratt and Whitney aircraft engines. The PW4000 was labeled the "new technology JT9D" when it began replacing the latter engine on 767s built after 1987 where the PW4000-94 is 5.8 percent heavier than the JT9D-7R4 but produces up to 10 percent more thrust. Aside from an additional set of long stator blades and elongated exit nozzle, the CF6-80C2 is also of similar weight and dimensions to the PW4000. Due to these similarities, the PW4000 engine model will be used for all impact simulations.

Table C–5. Boeing 767 engine comparison.

Engine	Pratt and Whitney PW4000-94	Pratt and Whitney JT9D-7R4[a, b]	General Electric CF6-80C2[c, d]
Fan blade diameter	94 (in.)	94 (in.)	93 (in.)[e]
Length	153 (in.)	153 (in.)	161–168 (in.)[f]
Dry weight	9,400 (lb)	8,885 (lb)	9135–9860 (lb)

a. Reference value of 106 in. also found—may include cowling.
b. The "tail" of the CF6-80C2 is much longer than the PW4000. This potentially accounts for the additional 15 in. in length.
c. The CF6-80C2 has an additional set of long stator blades for the excess fan air that is not present in the PW4000.
d. The second stage compressor blades in the CF6-80C2 are closer to the central shaft than the PW4000 and do not appear to have counter weights.
e. The JT9D-7R4 and PW4000-94 are almost identical: (1) They are in the same family of Pratt & Whitney aircraft engines, and (2) the PW4000 was labeled the "new technology JT9D" when it began replacing the latter engine on 767s built after 1987.
f. The PW4000-94 is 5.8 percent heavier than the JT9D-7R4, but produces up to 10 percent more thrust.

Airframe Model Development

All significant structural components are being included in the airframe model of the Boeing 767-200ER. Figure C–46 shows the status of the initial version of the complete aircraft model. Detailed models of the empennage and landing gears, not shown in this figure, are shown in Figs. C–47 and C–48, respectively. Ribs, spars, rudder, and elevator have all been modeled in detail in the empennage. Tires and hubs, the main strut and truck, and support bracing have all been included in the landing gear model. The underside of the airframe in the model is shown in Fig. C–49 illustrating the position of the retracted main landing gear in the wheel well.

The models of the fuselage, empennage, and wing structures are developed using shell elements. The model is being developed in parameterized form where the mesh resolution is determined by a single element characteristic size parameter. This approach was selected early in the development to allow flexibility in the model size and resolution as the model development and impact analyses progressed. The objective was to develop a mesh with typical element dimensions between one and two in. for small components, such as spar or rib flanges, and element dimensions of 3 in. to 4 in. for large parts such as the wing or fuselage skin. A summary of the current model size is shown in Table C–6.

Figure C–50 shows the entire wing structure modeled to-date, including the center wing which attaches the port and starboard outboard wings. The wing stringers were not explicitly modeled to help reduce the size of the model. The stringers have a z-section geometry with typical dimensions of approximately one in. flanges and a two in. web with a thickness of approximately 1/8 in. These stringers run spanwise over the top and bottom of the wing ribs. In the model, an ‘effective’ wing skin has been used to account for the weight and strength of the riveted skin/stringer construction.

Wing Section Component Model Development

Two wing segment models have been developed to perform the component level and subassembly level analyses. The smaller segment, for component analyses, is shown in Fig. C–51. The large wing segment for subassembly analyses is shown in Fig. C–52. The wing section components are modeled with shell elements. The main spars, wing ribs, leading edge ribs, nosebeams, leading edge slats, and outboard flaps have been included in the model. Nonstructural components, such as hydraulic lines, and mechanical components, such as slat actuators, are not included in the model geometry. The density of the spars, ribs and other structural components have been increased to account for this nonstructural mass.

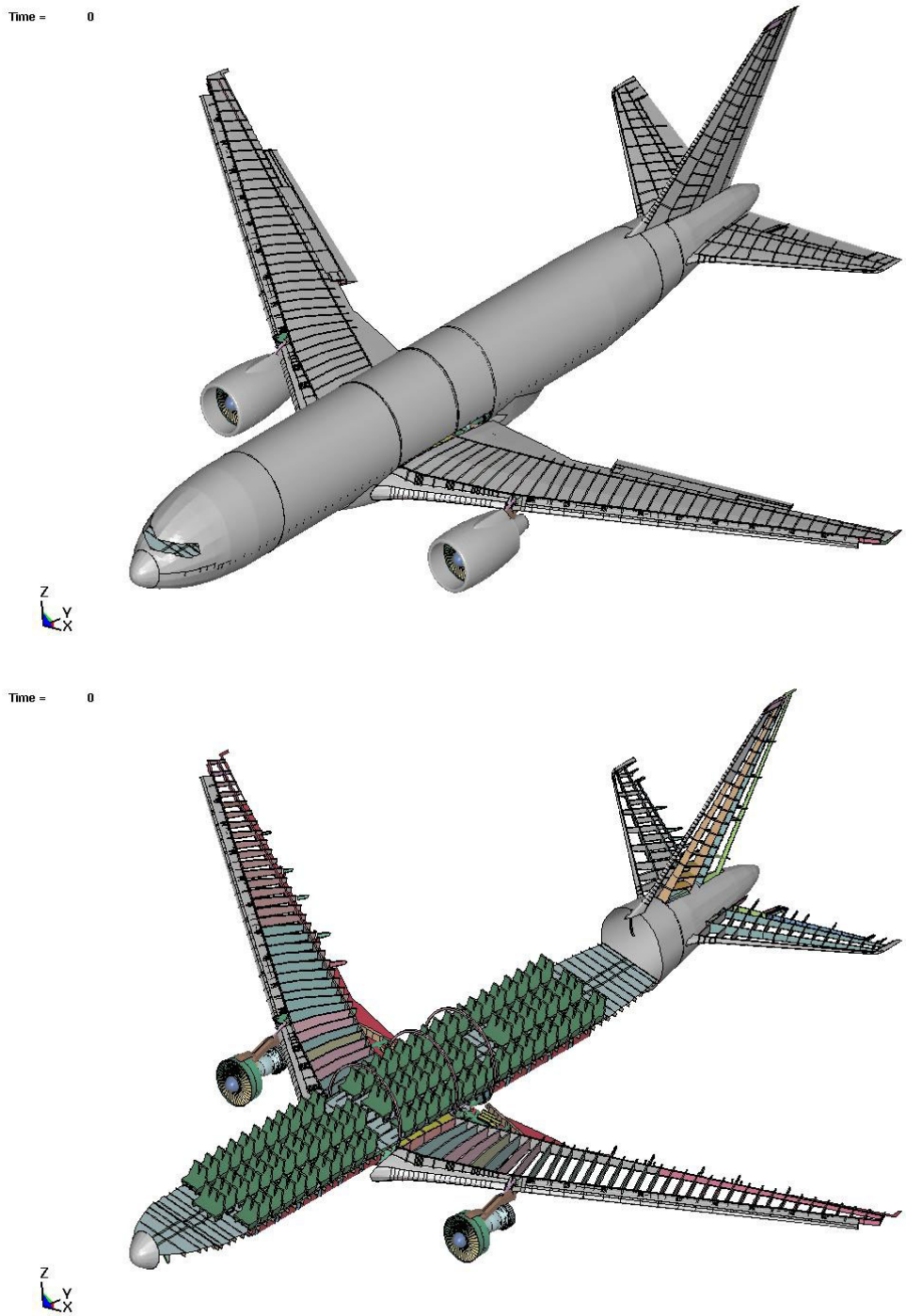

Figure C–46. Finite element model of the Boeing 767-200ER (under construction).

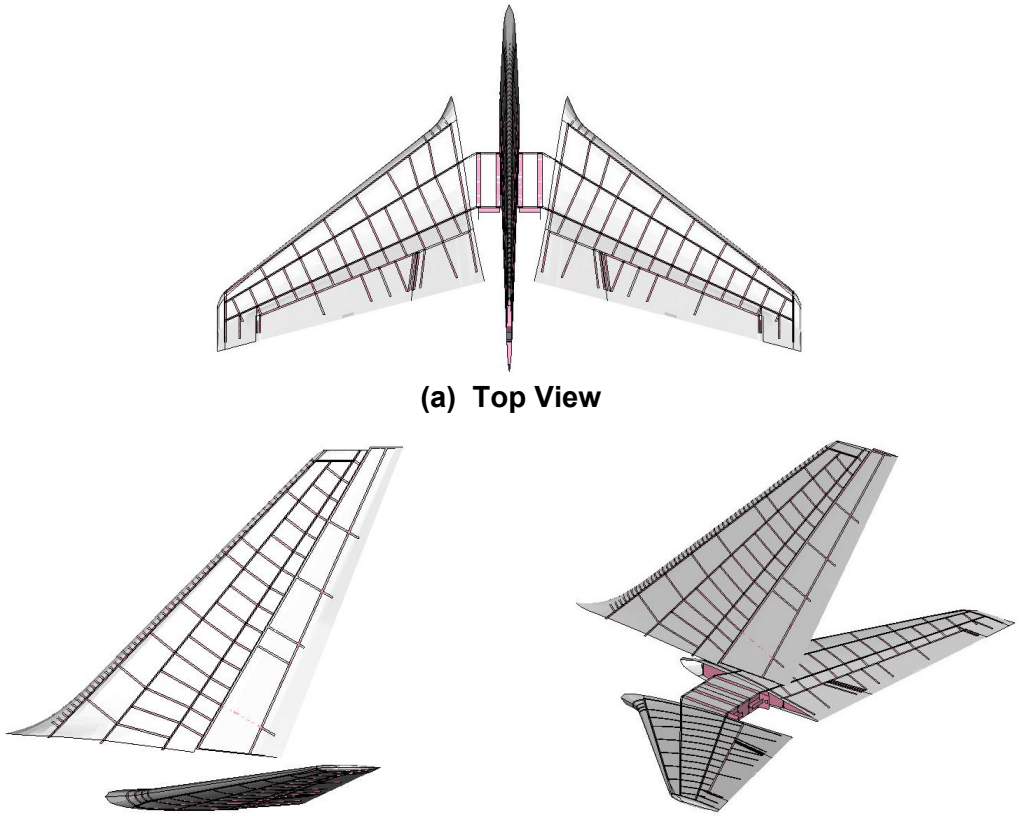

(a) Top View

(b) Side View

(c) Oblique View

Figure C–47. Complete empennage for the 767 aircraft model.

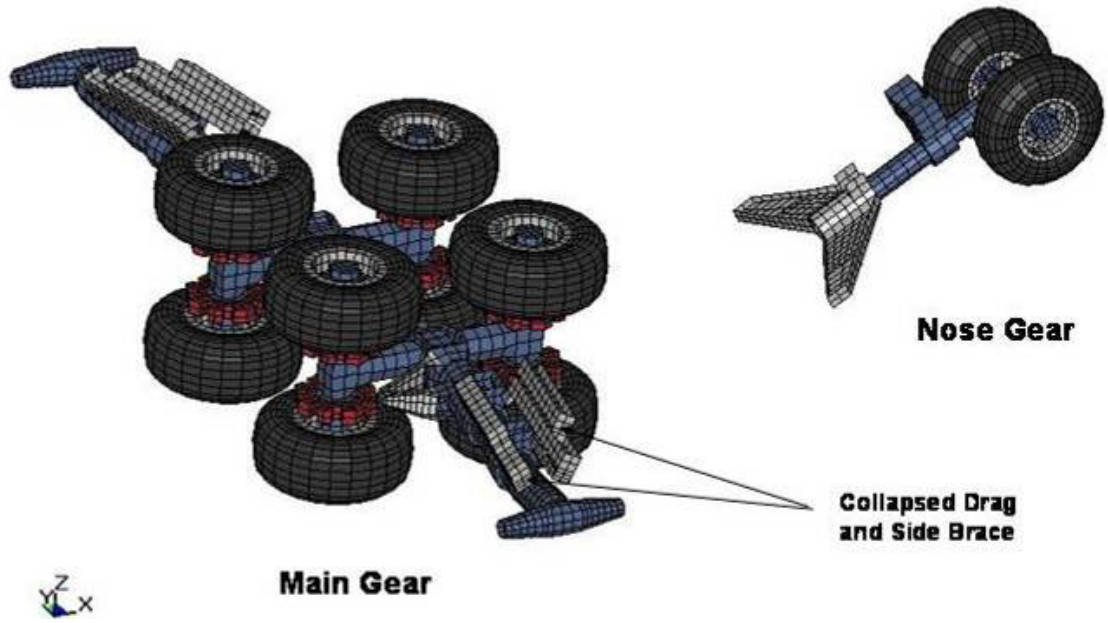

Figure C–48. Retracted landing gear components for the 767 aircraft model.

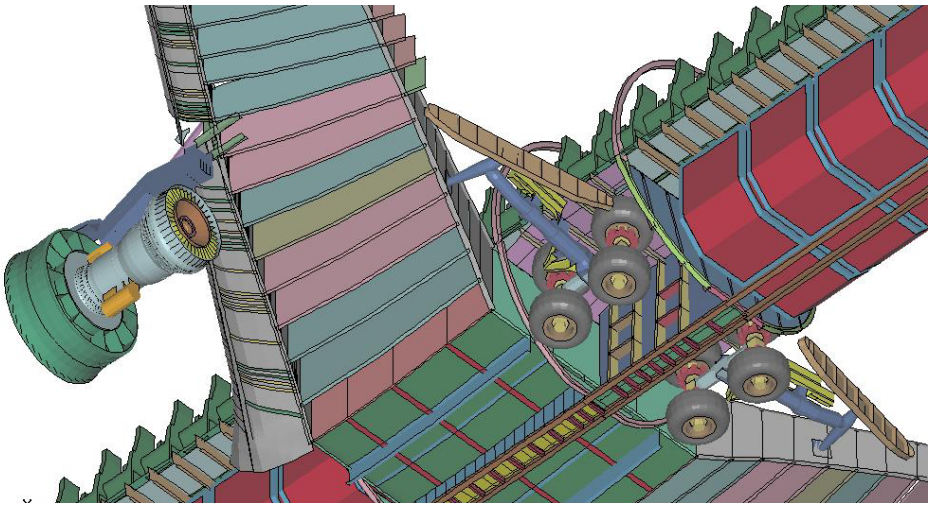

Figure C–49. Underside of the 767 airframe model (skin removed) showing the position of retracted main landing gear.

Table C–6. Summary of Boeing 767-200 aircraft model size (under construction).

	Number of Elements
Number of brick elements	70,000
Number of shell elements	562,000
Total nodes	740,000

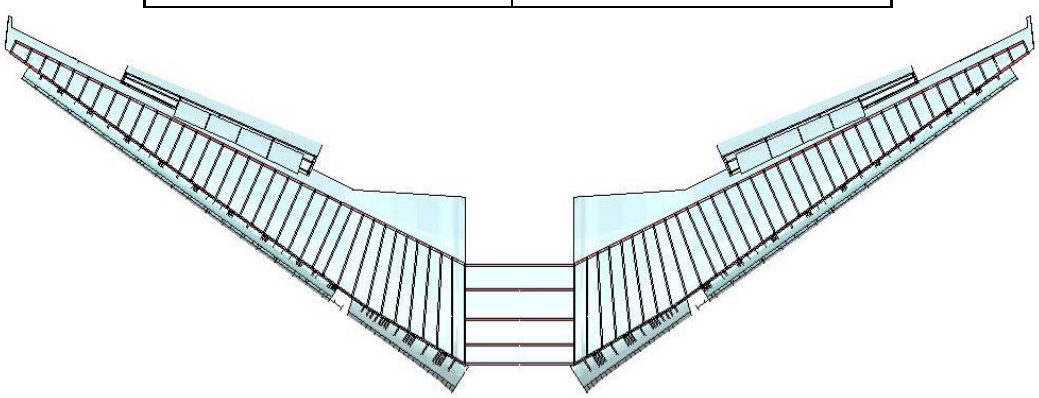

(a) Complete wing model

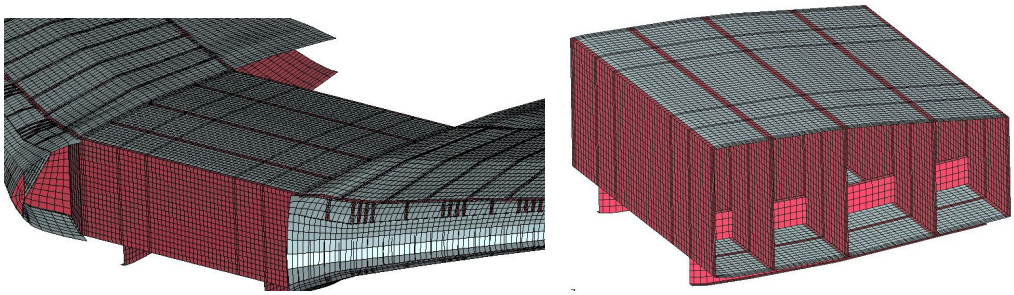

(b) Center wing structures

Figure C–50. Complete wing structures for the 767 aircraft model.

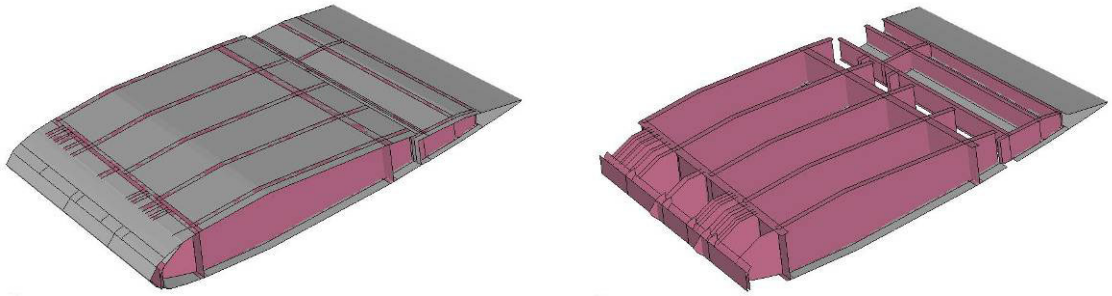

(a) Small Wing Section Model **(b) Internal Structure (skin not shown)**

Figure C–51. Small wing section model for component-level analyses.

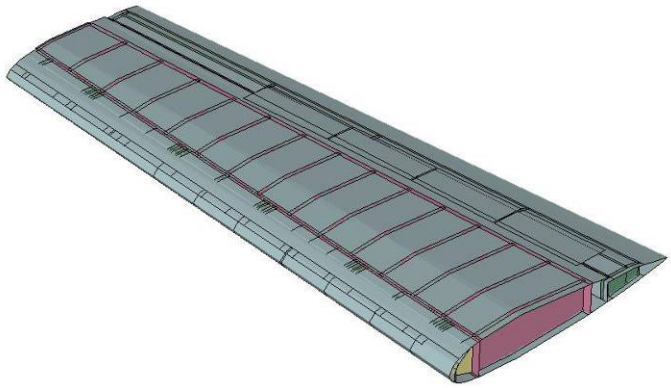

(a) Large wing section model

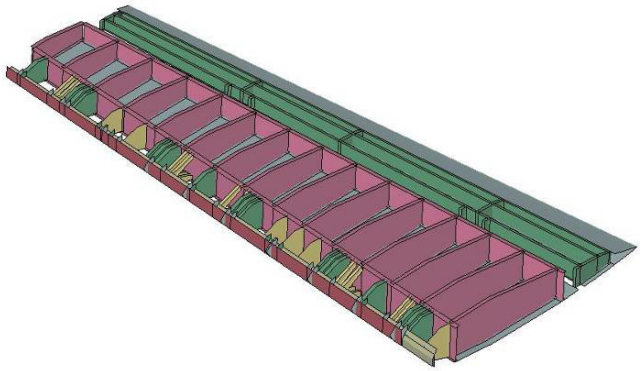

(b) Wing section internal structures (skin not shown).

Figure C–52. Wing section model developed for the subassembly impact simulations.

C.3.3 Analysis of Fuel Distribution at Impact

An important factor for determining impact damage and subsequent fire initiation is the distribution of the fuel in the aircraft at the time of impact. Both United Airlines and American Airlines have provided estimates for the quantity and distribution of fuel for UAL Flight 175 and AA Flight 11 at the time of impact.[1,2] UAL estimates that Flight 175 contained approximately 62,000 lb or 9,118 gal of fuel at impact with the "fuel evenly distributed between both main tanks."[1] American Airlines estimates that Flight 11 contained 66,081 lb or 9,717 gal of fuel at impact and "the fuel was evenly distributed between left and right wing tanks of the aircraft."[2]

Fuel tank locations and capacities for the Boeing 767 are shown in Fig. C–53. The Boeing 767 uses an integral fuel tank where the wing skin, ribs, and spars serve as the fuel tank. There are three classes of fuel tanks onboard the 767-200ER, a main tank, a surge tank, and auxiliary tanks. The auxiliary tanks consist of port, starboard, and center fuel tanks. All tanks are shown for the port wing in Fig. C–54 along with the associated internal structures. The main tank is from rib 3 to rib 31, the port and starboard auxiliary tanks are from the inboard closure rib to rib 3. The center auxiliary tank is between the port and starboard closure ribs and the surge tank is from rib 31 to rib 34. A dry bay is located above the engine at the forward part of the main tank between ribs 6 and 9. Baffle ribs are located at rib 5 and 18.

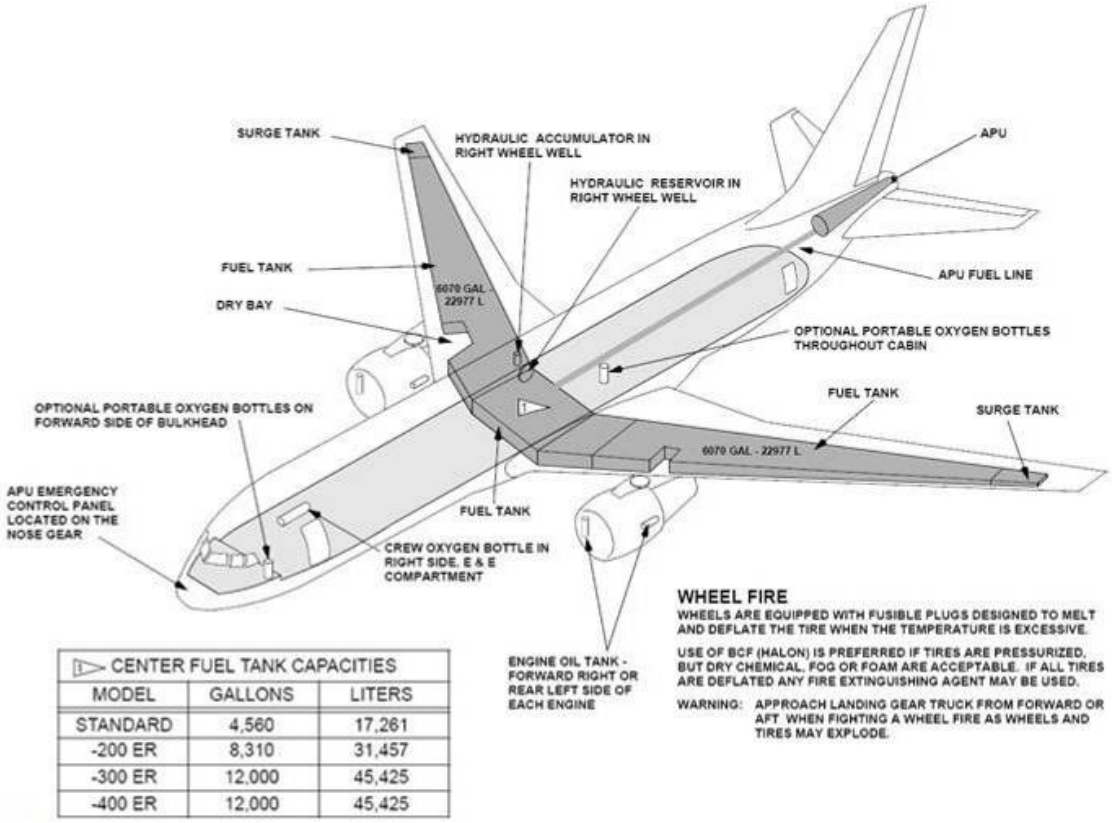

CENTER FUEL TANK CAPACITIES

MODEL	GALLONS	LITERS
STANDARD	4,560	17,261
-200 ER	8,310	31,457
-300 ER	12,000	45,425
-400 ER	12,000	45,425

Figure C–53. Flammable material locations in a Boeing 767 aircraft (www.boeing.com).

[1] Communication between United Airlines and NIST, September 5, 2003, "NIST WTC Flammable Contents Request."

[2] Communication between American Airlines and NIST, August 12, 2003, "In re September 11 Litigation C&F Ref.: DTB/MH28079."

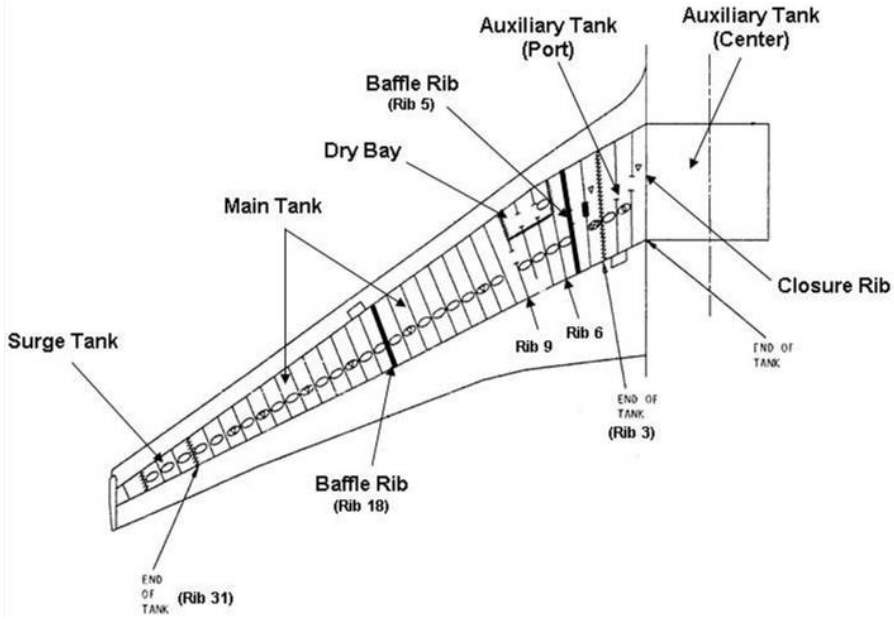

Figure C–54. Layout of fuel tanks in the Boeing 767 wing.

The functionality of the wing fuel tanks is such that a typical wing rib allows some fuel to flow along the wing but acts as a two-way fuel baffle to minimize fuel slosh. However, there are special rib designs that alter the position and flow of fuel within the tank. The ribs in the dry bay region, between ribs 6 and 9, include a fuel barrier running parallel to the rear wing spar. In addition, baffle ribs (ribs 5 and 18) include a series of fuel dams that act as a one-way valve allowing fuel flow inboard toward the sump areas (low point of tank). According to the statements from both airlines regarding fuel distribution, it is most likely that the surge tanks and all auxiliary tanks were dry at the time of impact.

Overall tank dimensions and geometry were estimated using the dimensions and approximated geometry shown in Fig. C–55. As shown in Fig. C–56, the front spar height is a good approximation for fuel depth in a full wing section. Using these approximate dimensions, the fuel tank capacity as a function of the distance along the wing buttock line (see Fig. C–57) was calculated. The maximum capacity of each main tank was calculated to be approximately 6,500 gal. The actual main tank capacity is 6,070 gal (Fig. C–53) so the calculated fuel capacity distribution was modified to match this maximum value, as shown in Fig. C–57. Notice that the main tank capacity inboard of baffle rib 18 is approximately the same volume as the fuel onboard each aircraft at the time of impact.

The exact location and distribution of fuel at the time of impact is complicated by the flight conditions prior to and at the time of impact. The terrorist pilots likely performed extreme flight maneuvers prior to impact causing most of the fuel to flow inboard. Extreme banking maneuvers with inappropriate trim could cause the fuel to flow inboard quickly. High loads on the wings due to the extreme flight regime at the time of impact would also cause fuel to flow inboard by increasing the dihedral angle of the wing. Since the baffle ribs restrict fuel from flowing outboard, it is reasonable to assume that all fuel that could flow inboard was actually inboard at the time of impact.

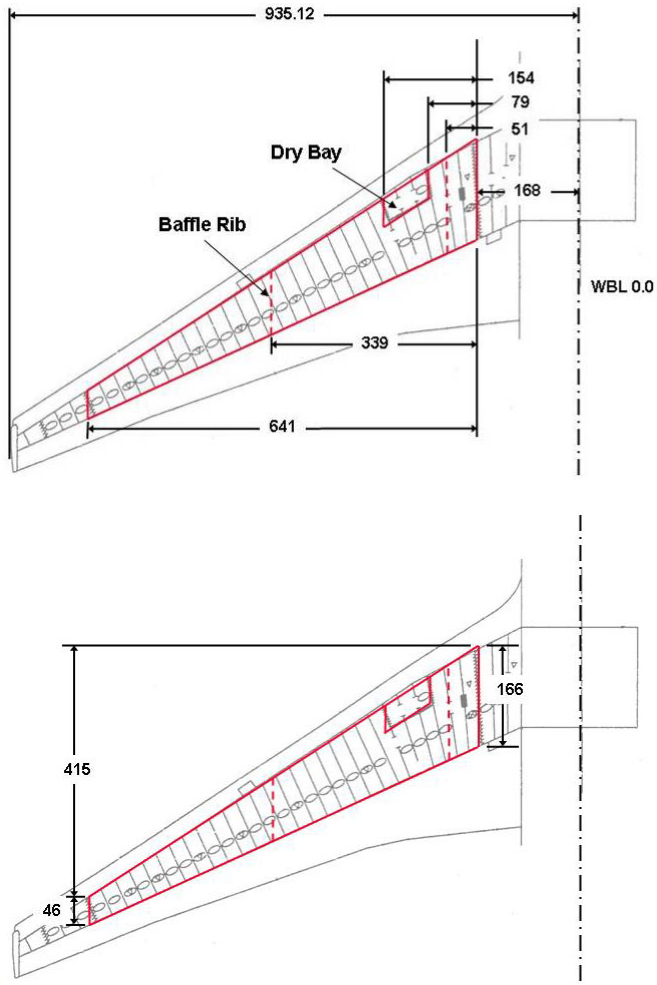

Figure C–55. Approximate fuel tank dimensions (in.).

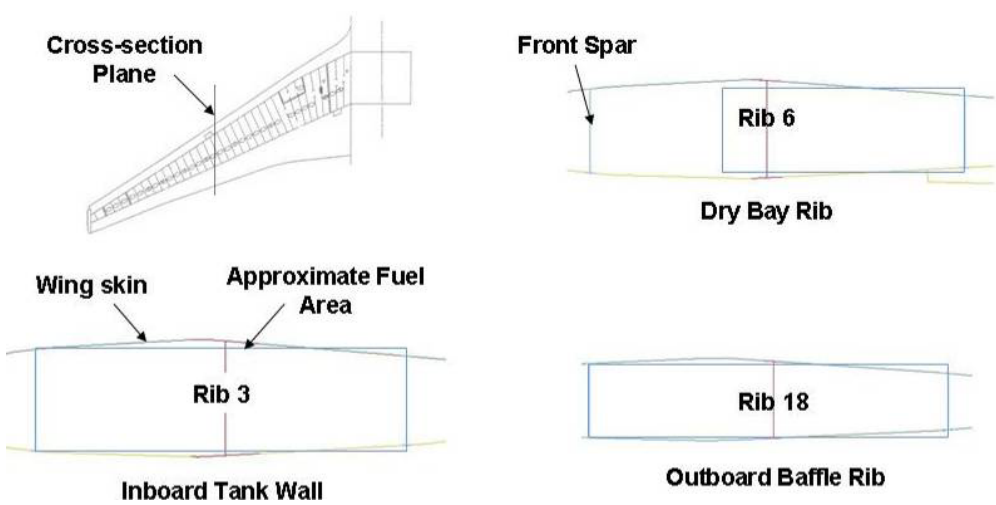

Figure C–56. Wing cross sections at various rib locations.

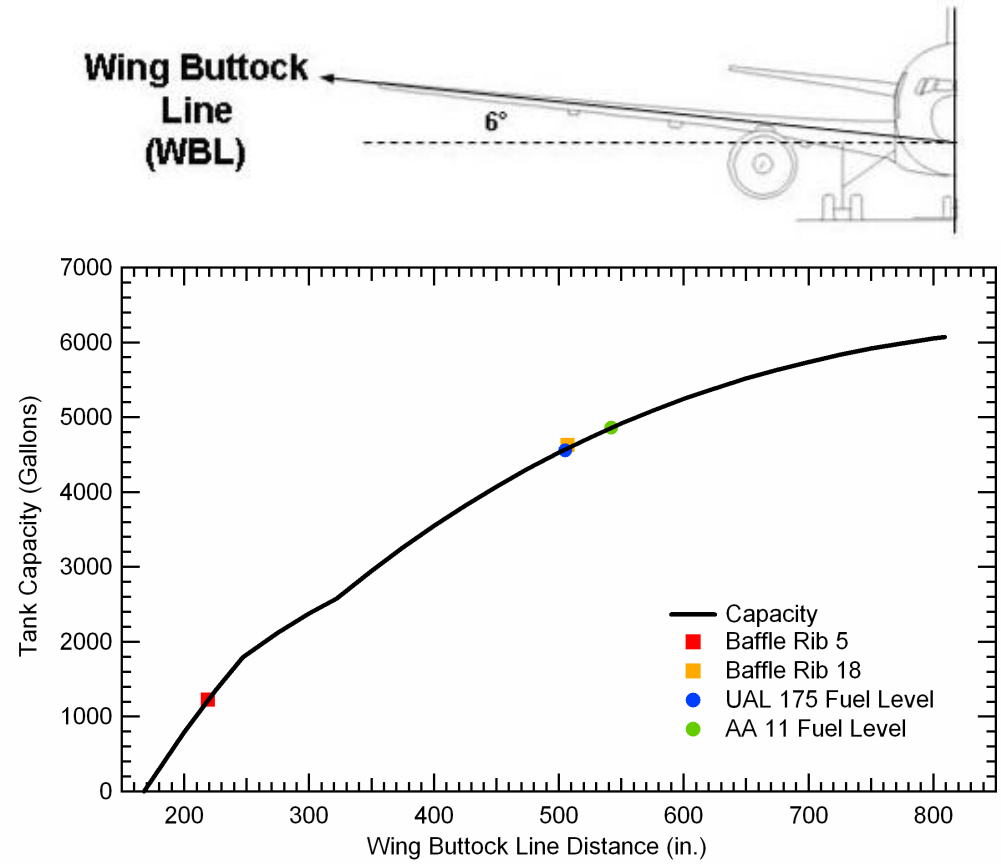

Figure C–57. Fuel tank capacity.

For simplicity, it was assumed that all fuel has moved inboard at the time of impact. Since the fuel tank capacity at the outboard baffle rib and the fuel onboard are approximately the same, a good first estimate is that the main tanks are full inboard of baffle rib 18 at the time of impact. A small amount of fuel is outboard of this rib for AA flight 11. This is shown graphically in Fig. C–58 for smooth and level flight with an undeformed wing shape. A full wing out to baffle rib 18 and dry outboard of this rib is taken as the nominal case in subsequent analyses.

C.4 COMPONENT-LEVEL ANALYSES

The primary objectives of component modeling are to (1) develop understanding of the interactive failure phenomenon of the aircraft and tower components and (2) develop the simulation techniques required for the global analysis of the aircraft impacts into the WTC towers. The approach taken for component modeling is to start with finely meshed, brick element models of key components of the tower structure and progress to relatively coarsely meshed beam and shell element representations that will be used for the subassembly and global models. This is done to develop reduced finite element models appropriate for high fidelity global impact analyses, as modeling each component with fine details would be too demanding from a computational standpoint and an inefficient use of resources.

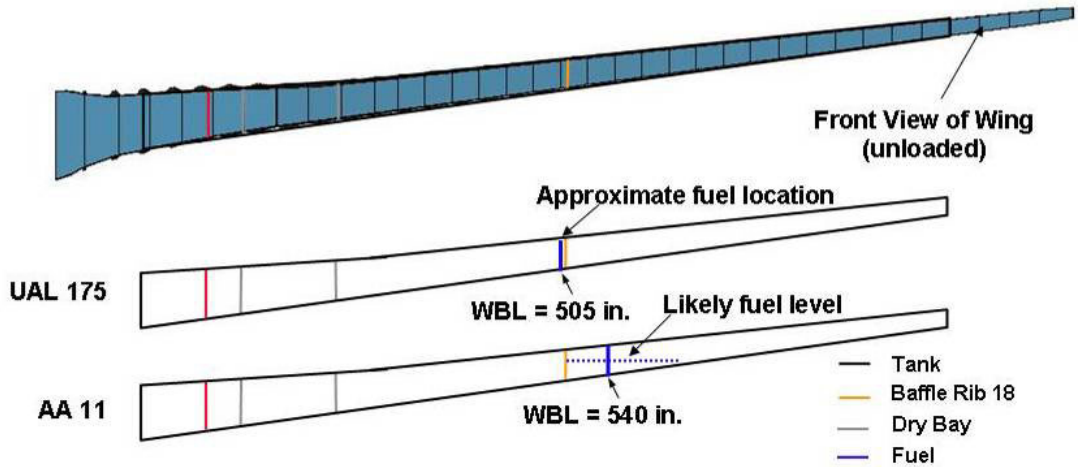

Figure C–58. Approximate fuel locations for smooth and level flight.

In addition to determining the optimal element size and type for global modeling, other key technical areas are addressed in the component modeling phase of the program. These issues include material constitutive modeling, treatment of connections, and modeling of aircraft fuel. The following component modeling scenarios were outlined at the start of the project:

- An exterior column impacted by an aircraft engine
- An interior column impacted by an aircraft engine
- An exterior column impacted by an aircraft wing segment with and without fuel

In addition to the above component impact analysis scenarios, a range of additional component analyses were identified that were considered important and helpful in developing the global impact models and analysis methods. These additional component analysis scenarios included:

- Bolted column end-plate connections with approximated dynamic loading
- Bolted spandrel connections with approximated dynamic loading
- Floor system with concrete slab impacted by an engine

The approach has deviated somewhat compared to the tasks above to maximize efficiency and to produce the most meaningful structural loading scenarios. Once preliminary calculations were performed it was found, for example, that the load generated by an impacting engine would totally overwhelm a single interior or exterior column. Simplified models based on this severe loading would match the detailed brick model but the subtle response from lesser loading might not be as accurate. To capture the more subtle response in the column components, wing sections with and without fuel were studied as impactors instead of engines. It was found that the empty wing section impact produced damage to the exterior columns that is near the failure threshold. Similarly, a fuel-filled wing section impacting both wide flange

and box type core column resulted in damage near the failure threshold. As a result, these impact scenarios were used primarily for the exterior and core column component impact analyses.

Included in this appendix are the impact analyses for exterior columns, core columns, bolted column connections, bolted spandrel connections, and floor systems.

C.4.1 Analysis Methodology

The impact analyses were performed using the LS-DYNA finite element code (LS-DYNA 2003). LS-DYNA is a commercially available nonlinear explicit finite element code for the dynamic analysis of structures (LSTC 2003). The initial foundation of LS-DYNA was the public domain DYNA3D finite element code developed at the Lawrence Livermore National Laboratory. Since 1987, the code has been extensively developed and supported by the Livermore Software Technology Corporation (LSTC) and is used for a wide variety of crash, blast, and impact applications.

LS-DYNA has several unique capabilities for this project such as Arbitrary-Lagrangian-Eulerian (ALE) and Smooth Particle Hydrodynamics (SPH) algorithms that can be applied to the analyses of fluid-structure interaction and large-scale fracture and fragmentation of structures. These capabilities are critical for the analyses of the fuel tank breakup and dispersion of fuel inside the towers upon impact. The fuel and debris dispersion is crucial for assessing the impact loads inside the tower structures and the corresponding damage to the mechanical systems.

The impact analyses described in this report use a variety of capabilities and algorithms in LS-DYNA. A brief description of these capabilities is described in this section. A significantly greater detailed description of the analysis methods is provided in the LS-DYNA Theoretical Manual (1998).

The fine mesh detailed component analyses typically use 8-node solid hexahedron (brick) elements with single point integration. This is the most commonly used solid element type in LS-DYNA due to its computational efficiency. The biggest disadvantage of the single point integration is the potential for hourglassing or zero energy modes. There are several methodologies for controlling hourglass modes in LS-DYNA. The typical approach used in these impact analyses is to apply a viscous hourglass control where a viscous damping is introduced that suppresses the formation of hourglass modes but does not significantly influence the global modes.

The component impact analyses using solid elements typically have a fine mesh. As a result, damage and failure are included strictly through the constitutive algorithms. Damage criteria (such as maximum plastic strain) are tracked for each element within the constitutive model evaluation, and elements are eroded when the failure criteria are exceeded. This allows for a direct evaluation of damage and failure within the impact simulations.

The eroded elements allow for the initiation and extension of fracture in the model. Eroded elements no longer support any stress, and the strains in the eroded elements are no longer calculated. The associated mass of the elements remains with the nodes in the calculation. If adjacent elements have not reached the failure surface, the nodes remain attached to the structure. If all of the elements connected to a specific node have failed, the node becomes a free particle. Free nodes can either be eliminated from the calculation or remain in the calculation with associated inertial properties and potential for impacts against other structural components (free nodes remain in contact algorithms).

As the mesh refinement and model size are reduced, the components are typically modeled using Belytschko-Lin-Tsay shell elements. This is a four node shell element with single point integration. The Belytschko-Lin-Tsay element is a computationally efficient alternative to the Hughes-Liu element in LS-DYNA and again is the most widely used shell element formulation within LS-DYNA for crash, impact, and metal forming applications. Results generated with the Belytschko-Lin-Tsay element typically agree with those using the Hughes-Liu element. As used in the solid elements, the most common approach to introducing damage and failure for the shell elements is through the constitutive models and element erosion.

In specific applications, unique algorithms are required to introduce failure modes in the analysis. An example is the interface between the skin and internal frame structures of the aircraft. Rivets are used for the primary connection between the airframe and skin. The approach used to model this connection and failure during the impact event is the tied interface with failure. In this approach, interface segments (shell elements) are constrained to move together until a failure criterion is exceeded. The failure criterion is a quadratic combination of the normal and shear failure stresses at the interface. After failure, the segments are allowed to move independently but not allowed to penetrate each other (typical contact algorithm behavior).

Overall contact in the impact analyses is modeled using the automatic single surface contact algorithm in LS-DYNA. Interacting components are defined by a material list, and contact segments are automatically generated by LS-DYNA. This greatly simplifies the specification of contact between various components in the aircraft and tower structures. The type 1 soft constraint option is used in the contact algorithm that determines the contact stiffness based on stability considerations, time step size, and nodal mass. This soft constraint option was found to be more robust than the default penalty formulation for modeling the complex contact behaviors in large impact and crash simulations.

C.4.2 Exterior Column Impact Analyses

Various exterior column component impact analyses were performed with different objectives. The preliminary exterior column component impact analyses were performed on a single column using a highly refined mesh of brick elements. These analyses were used to investigate the details of the column response and develop analysis techniques that can be applied to the subassembly and global impact analyses. These preliminary exterior column impact analyses used a simplified wing section impactor that was developed prior to gathering detailed structural information of the Boeing 767 wing design.

Subsequent exterior column impact analyses were performed using less refined models of the exterior columns in full panel configurations impacted by detailed wing section component models with and without fuel. The primary objective of these component analyses was to study the impact response of the aircraft wing structures and investigate various modeling techniques for including aircraft fuel in the analyses.

Figure C–59 shows the calculated response of a single exterior column component, impacted by an empty wing section. The figure compares the column damage calculated with two different models of very different resolutions. The column model on the left is a fine mesh made of brick elements and the column on the right is a coarser mesh of shell elements. The failure strains of the coarse model were estimated by calibrating the response of the coarse model against the refined model (see Section C.2.2). Contours of

resultant displacements are shown on the column components. It can be seen that the overall response, both in column and wing segment damage, is very similar. These analyses were used to develop the coarse column models used in subsequent analyses.

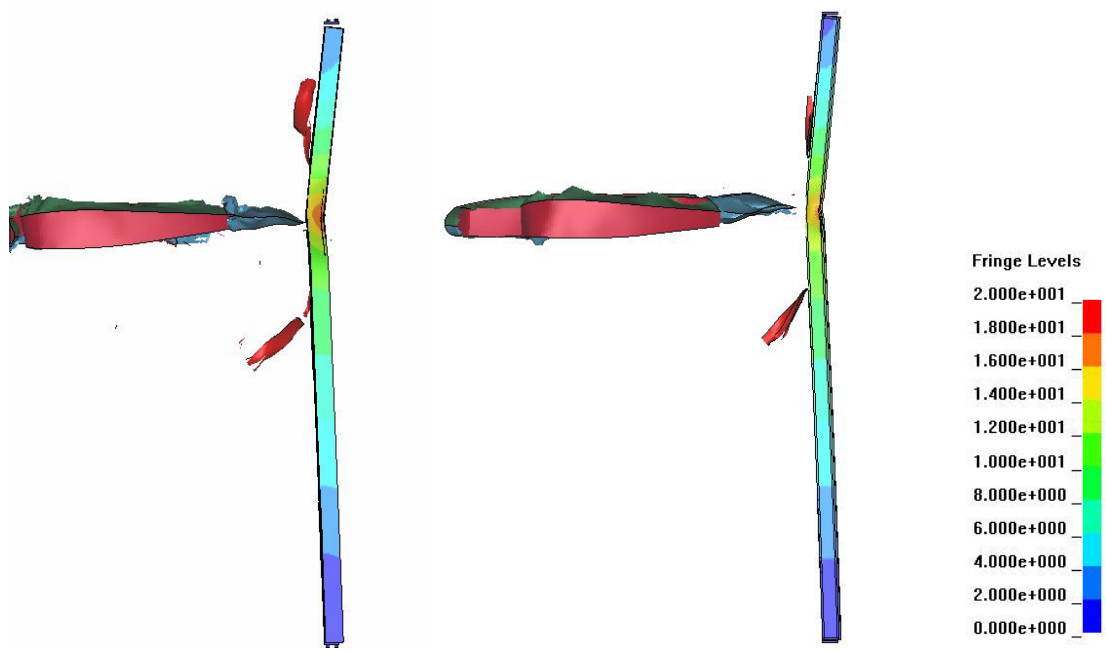

(a) Fine brick element column **(b) Coarse shell element column**

Figure C–59. Exterior column response comparison, showing contours of the displacement magnitude (in.).

Empty Wing Section Impact Analysis

Figure C–60 shows the impact of the small empty wing section into two exterior wall panels at a speed of 500 mph (223 m/s). These analyses use a wing section model with significantly improved structural fidelity over the preliminary wing segment model used in the column component impact analyses described above. The development of the wing section component model used here was described previously in Section C.3.2. The wing section model shown in Fig. C–60 consists of approximately 24,000 shell elements.

The model for the two exterior panels is made primarily of shell elements with a medium mesh resolution. The exceptions are the butt plates, which were made of solid brick elements and the bolted butt plate connections using beam element bolts, as described later. The boundary conditions at the ends of the exterior columns are a bolted connection to an adjacent butt plate with constrained displacements at the edges. In addition, the displacements in the direction of the impact were constrained on the spandrel plates at the location of the floor slab. The resulting model for the exterior panel had 54,096 shell elements (columns and spandrels), 2,112 solid brick elements (24 butt plates), and 48 beam elements for the bolts.

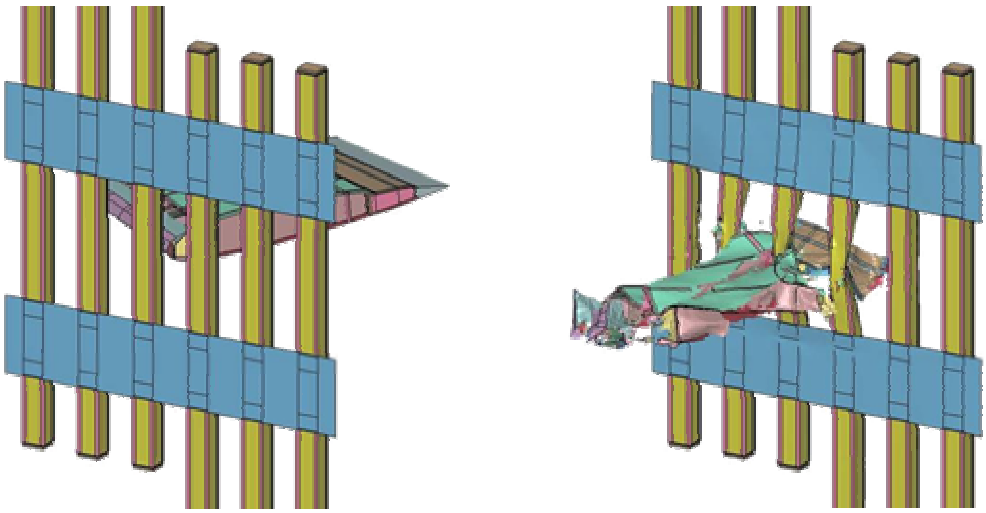

(a) Impact Configuration **(b) Calculated Response**

Figure C–60. Calculated impact damage with the empty short wing section component model.

The calculated impact response produces large scale damage and fragmentation of the empty wing section and significant damage to the exterior columns. The calculated impact damage to the exterior column panel is shown in Fig. C–61. The damage includes significant distortion of the columns, large plastic strains, and fracture of the plate connections within the columns. However, the columns are not completely severed and still maintain some load carrying capacity.

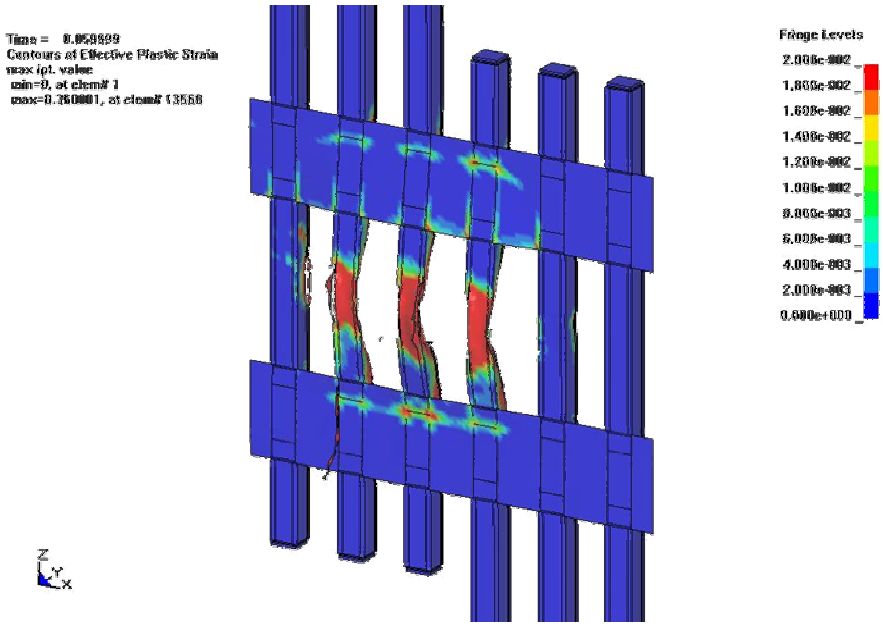

Figure C–61. Damage produced by the empty wing section impact.

Wing Section with Fuel Impact Analysis

A significant portion of the weight of a Boeing 767 wing is from the fuel in its integral fuel tanks. At the time of impact, it is estimated that each aircraft had approximately 10,000 gal of fuel on board. Upon impact, this fuel is responsible for large distributed loads on the exterior columns of the WTC towers and subsequently on interior structures, as it flows into the building. It therefore could have a significant effect on the damage done to the building structure. Accurate modeling of the fluid-structure interaction is needed to accurately predict the extent of this damage and the fuel dispersion within the building to help establish the initial conditions for the fire dynamics modeling.

A number of approaches to solving Fluid-Structure Interaction (FSI) problems are available in LS-DYNA. One approach is the standard Lagrangian finite element analysis with erosion, where the fuel is modeled using a solid mechanics approach. This approach accounts for the inertial effects of the fuel, but does not simulate the fuel flow during impact. The ALE method has been developed as one good approach to solve fluid and solid material interaction. With this methodology, fluids are modeled with a fixed Eulerian mesh, which allows for materials to flow between mesh elements. Solid materials are modeled with a moving Lagrangian mesh. With ALE, both mesh types can interact. An alternative approach is to use mesh-free methods such as SPH. SPH modeling for fuel effects has the advantage of a smaller mesh size and potentially much faster run times than ALE analyses. Both methods will be applied to the analysis of fuel impact and dispersion.

The small wing segment was used for performing component level analyses of the wing with fuel. The small wing segment is from rib 14 to rib 18, the outboard baffle rib. For this location, the segment was considered to be completely full of fuel. Figure C–62 shows the fuel-filled wing section model with an SPH mesh for the fuel, shown in blue. The wing section model is identical to that used in Fig. C–60, but with the addition of 4,400 SPH fuel particles.

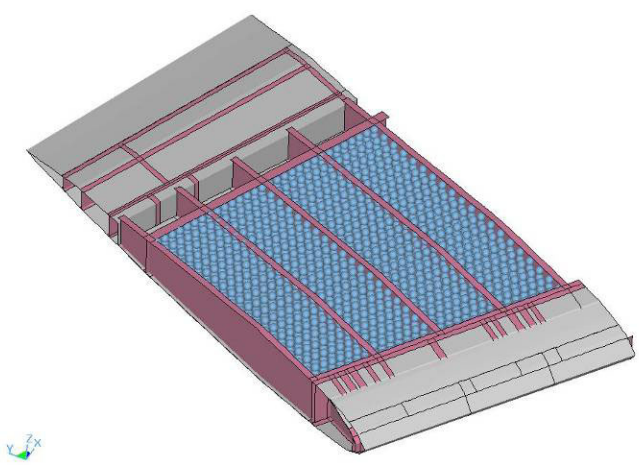

Figure C–62. SPH fuel in the small wing segment.

For the wing section with fuel component analyses, the impacted structures are the same two exterior panels as used in the empty wing section analysis above. As shown in Fig. C–63, the columns of the exterior panels are completely destroyed due to impact. Both the SPH and ALE methods simulate this extensive damage. This was not the case for the empty wing section model, as discussed in the previous section.

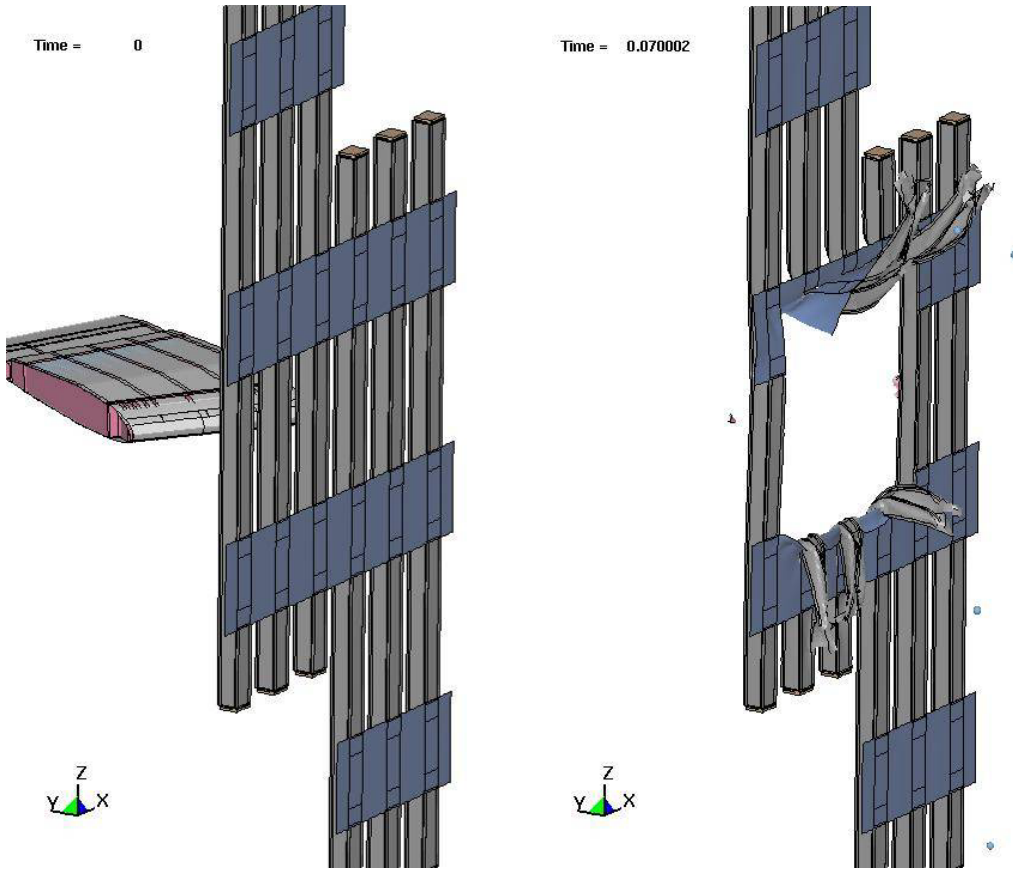

(a) Prior to impact **(b) After impact**

Figure C–63. Exterior panels impact behavior for a wing segment with fuel (SPH fuel model).

Figures C–64 through C–67 show the fuel dispersion and wing break up predicted by the two fuel modeling methods (ALE and SPH). As most clearly shown in the side view, the current SPH modeling method predicts greater fuel dispersion and wing break up than from using ALE. Current efforts are underway to study the effect of mesh density on these results. Both analysis methods calculate an impact load sufficiently large to easily rupture the exterior columns.

Run-times from these component analyses clearly indicate that the SPH method will be more practical for the global impact analyses. The current SPH model runs significantly faster than the ALE method as it requires a smaller mesh and does not need to rezone after each time step, as is done in the ALE method. In addition, the ALE method requires a mesh for both the fuel region and the void zone into which the fuel can flow. In the example shown, this required the addition of approximately 110,000 solid elements for the ALE analysis. These preliminary calculations indicate that the ALE analysis run-times are as much as 10 times longer than those for the SPH analyses. However, additional work is underway to

determine the mesh refinement in each approach required to calculate the fuel impact load effects and dispersion with sufficient fidelity.

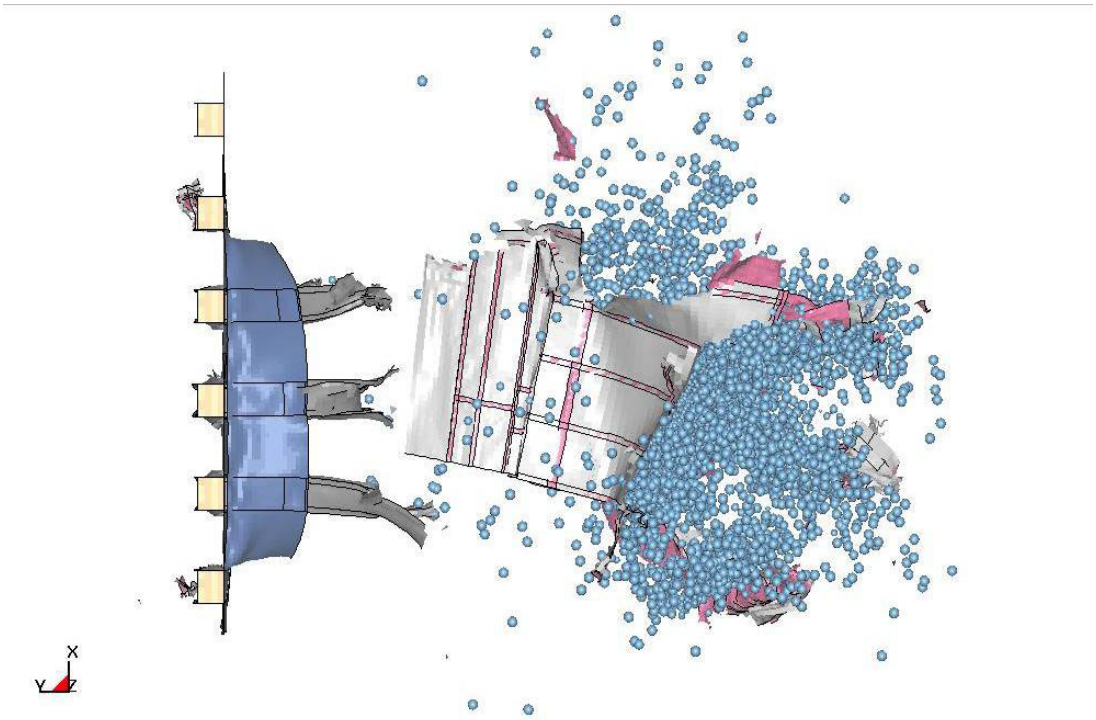

Figure C–64. SPH Analysis of structural damage and fuel dispersion (top view).

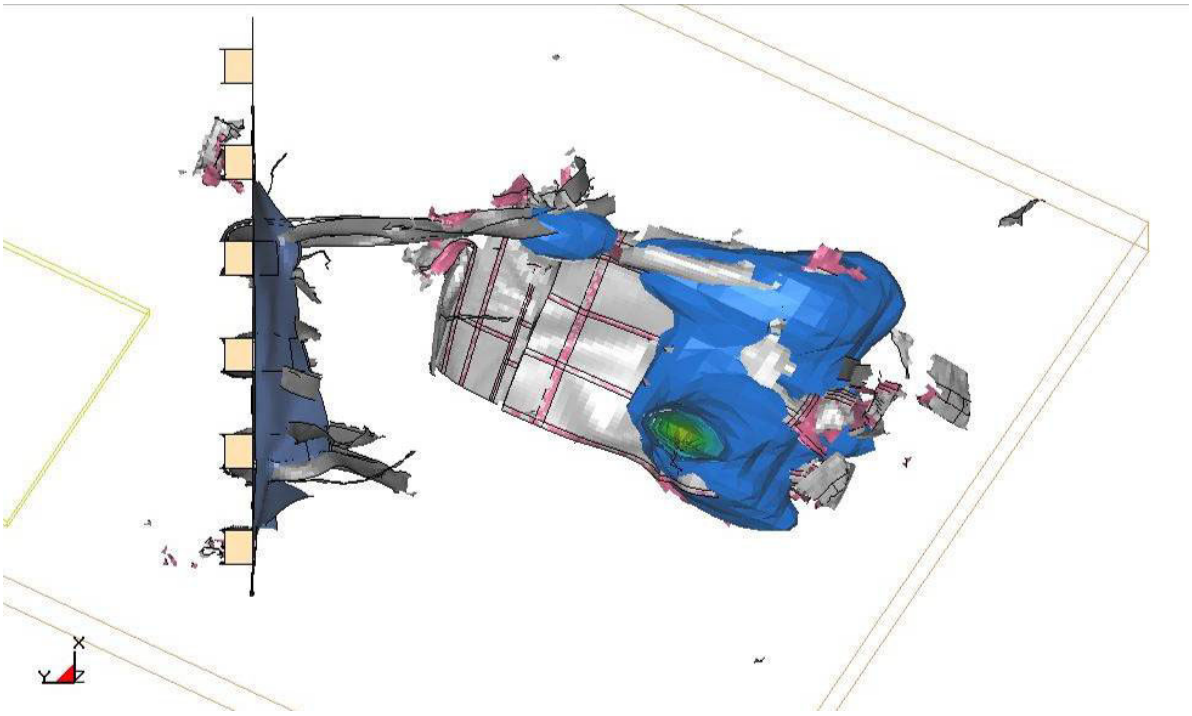

Figure C–65. ALE analysis of structural damage and fuel dispersion (top view).

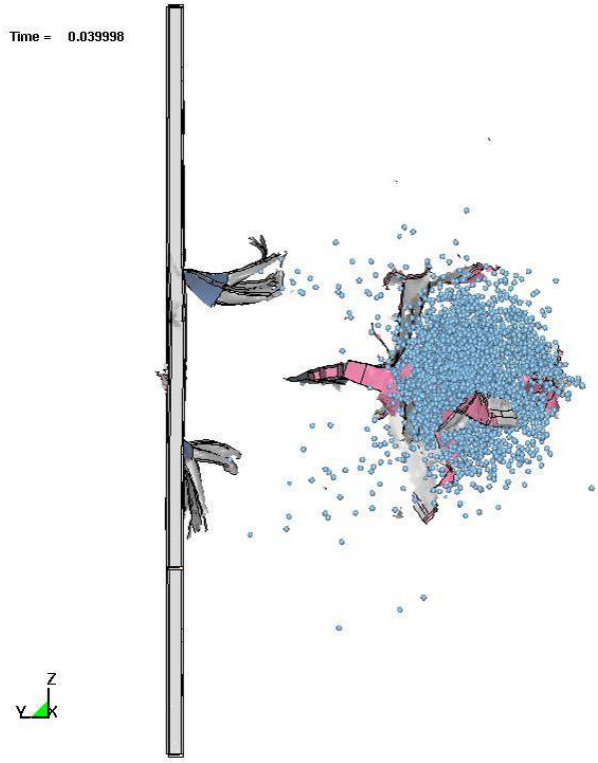

Figure C–66. SPH analysis of structural damage and fuel dispersion (side view).

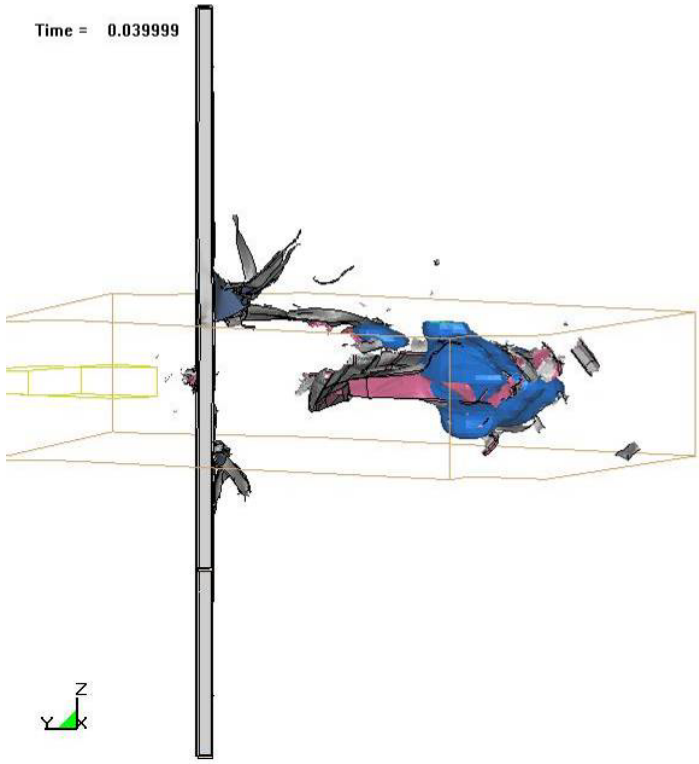

Figure C–67. ALE analysis of structural damage and fuel dispersion (side view).

Bolted Connection Modeling

There are a wide variety of different connections required for the assembly of the towers and aircraft. Wherever possible, evidence gathered from WTC steel will be applied to determine the importance of including connection details in the model and failure modes of those connections. For example, photographic and structural debris evidence clearly demonstrated that the external column connections played a significant role in the mode of column failure and extent of the external damage.

Two connections are of particular interest to the impact analysis of the aircraft into the WTC towers and are modeled in this section. These include the bolted connections at exterior column butt plates and the bolted spandrel connections. The objective of connection component analyses is to develop connection models for the global impact analyses that accurately capture the capacity and failure modes of the connection. Various connection component models developed include both fine models of these complex connection components (e.g., 3-D brick element models of bolts), to simple models such as beam element bolt models and tied constraints with failure. The constitutive behavior of the beam element bolt was described previously in Section C.2.1. A tied constraint with failure requires that two nodes or a node and a surface segment (shell element or solid element face) have tied degrees of freedom until a failure criterion is exceeded.

The coarse component models utilize many of the simplified connection and element types available in LS-DYNA to approximate the behavior observed in the fine models. For example, in the exterior column bolted connections, the bolts were modeled with elastic-plastic beam elements calibrated to match the fine model. Bolted joints, such as in the spandrel connections, were approximated with tied node algorithm that constrains degrees of freedom of adjacent nodes and element faces. Various options are investigated in these component analyses and final selections of the modeling methodology are based on both the fidelity and efficiency of the modeling approaches.

Component modeling of the exterior column butt plate connections has been completed. As shown in Fig. C–68 the detailed model includes individual bolts modeled with solid brick elements. The simplified model uses coarse brick butt plates joined by beam element representations of the bolts. A dynamic analysis was carried out to calibrate the beam element bolt model. The loading condition was a dynamic separation of the two butt plates. The velocity profile used to separate the butt plates was obtained from a preliminary engine impact analysis against the exterior wall similar to those described in the next subsection. The profile is a linearly increasing separation velocity between the butt plates with an initial velocity of zero and a velocity of 43 ft/s (13 m/s) at a time of 5.0 ms.

Failure strain in the beam models was calibrated such that the beam bolts failed at the same time as the brick element bolts. Failure of the bolts occurs at a time of approximately 3.0 ms. These connection models were used in the corresponding brick and shell models of the exterior column component impact analyses shown previously in Fig. C–59. Connection failure at the column ends was quite similar in both cases.

The spandrel connections consist of an overlapping splice plate across a spandrel joint with a row of bolts on either side of the joint. Typical failure of these spandrel joints in the impact zone resulted from bolt bearing shear failures, typically in the spandrel plate, as shown in the photographs in Fig. C–69. A common configuration in the impact zone would have six bolts on either side of the joint. The bolt bearing shear failure mechanism would be difficult to model using a beam element bolt as applied

previously to the exterior column bolted connections. In the exterior columns, the bolts fail primarily in tension and details of the contact between bolts and butt plates are not as important for capturing the failure behavior. As a result, an alternate modeling approach was required for the spandrel splice failures.

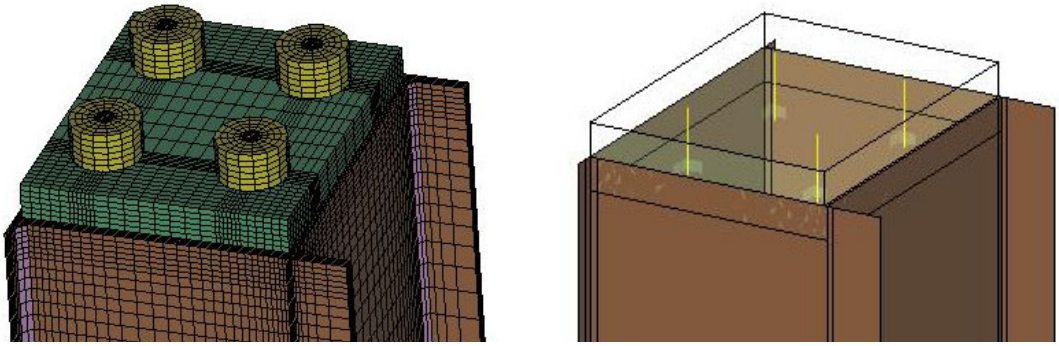

(a) Brick element bolts **(b) Beam element bolts (butt plates shown as transparent)**

Figure C–68. Exterior column end connection modeling.

Figure C–69. Typical bolt bearing shear failures of spandrel connections.

Spandrel connections are modeled using a splice plate made up of shell elements, as shown in Fig. C–70. Connections corresponding to individual bolts are treated by tying single nodes on the splice plates (center of green squares in Fig. C–70) to the spandrels. Two material definitions are used to make up the splice plate to allow for contact between the splice plates and the spandrels as well as having tied contact. The first splice plated material definition (shown in green in Fig. C–70) is used to allow the center node tied constraint (representing the bolt connection) to be aligned with the center of the spandrel plate. Since this material includes the tied constraint, it is not included in the automatic contact definition. The second material definition in the splice plate (shown in red in Fig. C–70) has a standoff distance equal to one half of the combined thickness of the spandrel and splice plate and is included in the automatic contact definition. Both material definitions have the same constitutive properties; however,

using a single material definition would sometimes result in a numerical instability due to conflicting constraint and interface algorithms on those segments. The application of the spandrel splice plate connection model is demonstrated in the engine impact component analyses below.

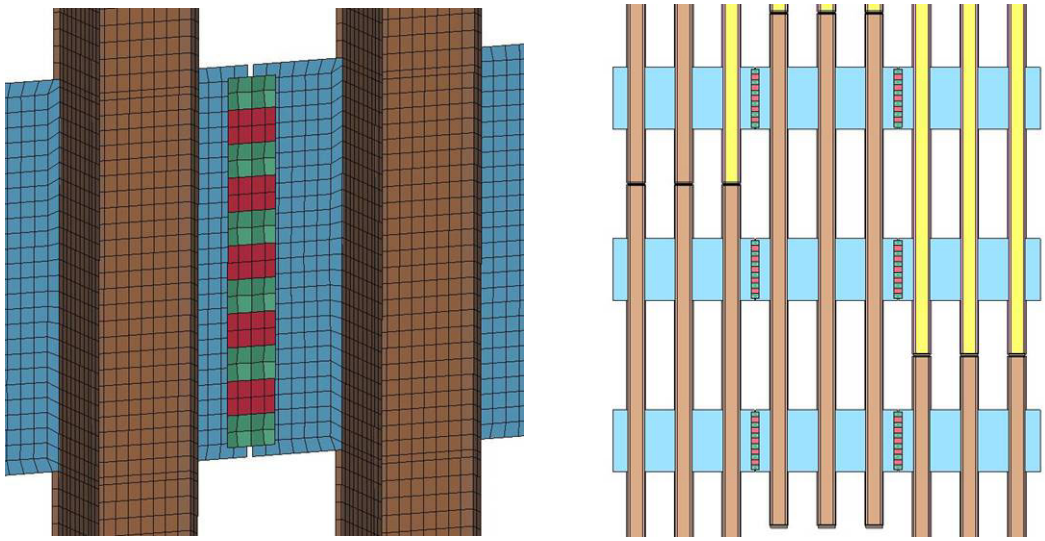

(a) Detail of spandrel connection **(b) Multiple panel connections**

Figure C–70. Bolted spandrel connection modeling.

Engine Impact Analysis

An example of an engine impacting an assembly of exterior panels is shown in Fig. C–71. The analysis includes an engine impacting an exterior panel of WTC 1 and is centered on panel 124 at floor 96 (the impact is centered on the middle spandrel). The exterior wall model does not contain any boundary conditions or components to represent the truss floor behind the panels. The initial engine speed was 500 mph (223 m/s). In this example, a medium mesh density shell element panel was used. Columns were connected with beam element models of individual bolts. Spandrels were merged together in this model—splice plates were not used. Fixed butt plates were bolted at the free column end and no boundary conditions were applied to represent the floors. Velocity time-histories for representative engine materials are shown in Fig. C–72. The plot shows an overall reduction in speed of about 13 percent after impact with the exterior wall.

A second engine impact analysis was performed with similar conditions except the impact location was moved downward by one half floor to create an impact centered between spandrels. A comparison of the two calculated impact behaviors is shown in Fig. C–73. In both analyses the engine breaks through the exterior wall with relatively little breakup of the engine core. The impact centered between spandrels results in a reduction in the velocity of the engine core of 56 mph (25 m/s).

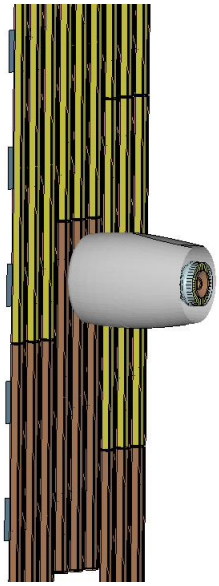

(a) Initial configuration

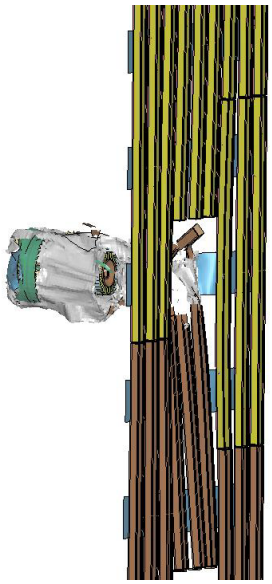

(b) Impact response at 40 ms

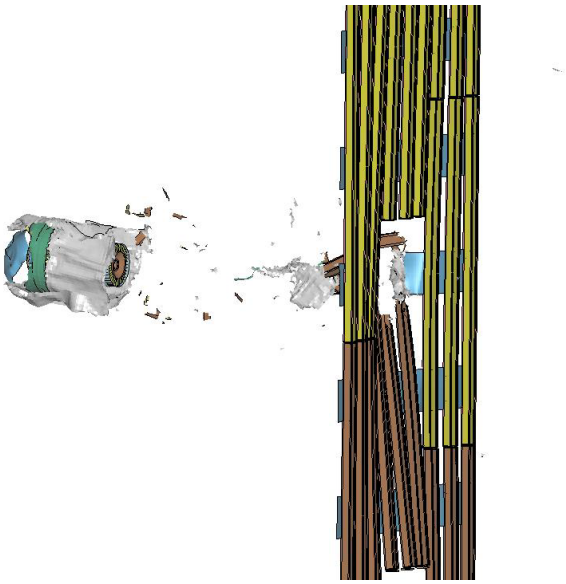

(c) Impact response at 80 ms

Figure C–71. Example engine impact analysis with exterior columns.

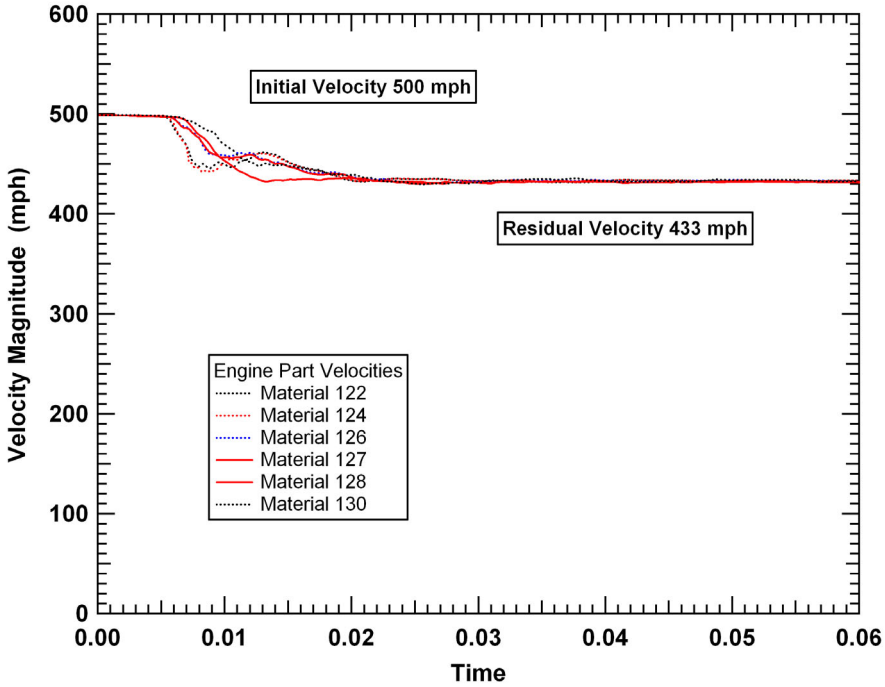

Figure C–72. Engine velocity history for the exterior wall impact.

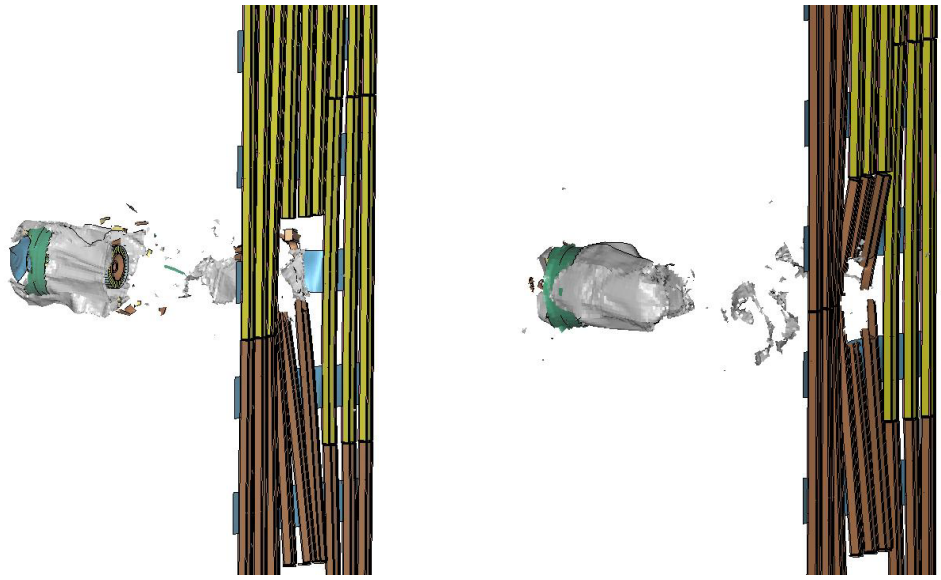

(a) Spandrel centered impact **(b) Between-spandrel impact**

Figure C–73. Example engine impact analysis with different impact locations.

A final revision of the above analysis included adding splice plates at the spandrel connections as explained in the previous subsection. Figure C–74 presents a comparison of both models. The figure shows exterior wall damage as seen from the outside without engine components. Contours of plastic strain are shown in the plot with blue being zero strain and red being at the failure strain threshold (20 percent in this case). Material exceeding the maximum failure strain is eroded and no longer shown

in Fig. C–74. The analyses differ most in spandrel failure modes. Spandrels fail at the column connection in the merged spandrel case, while the connection fails in the splice plate case. In the latter case, a realistic bearing stress type tear-out mode is seen in the splice plate. Engine core velocities for the three engine impact analyses are compared in Fig. C–75 for a single representative engine component. The splice plate model resulted in a 74 mph (33 m/s) velocity reduction of the engine core. The splice model results in the largest reduction in velocity in the engine.

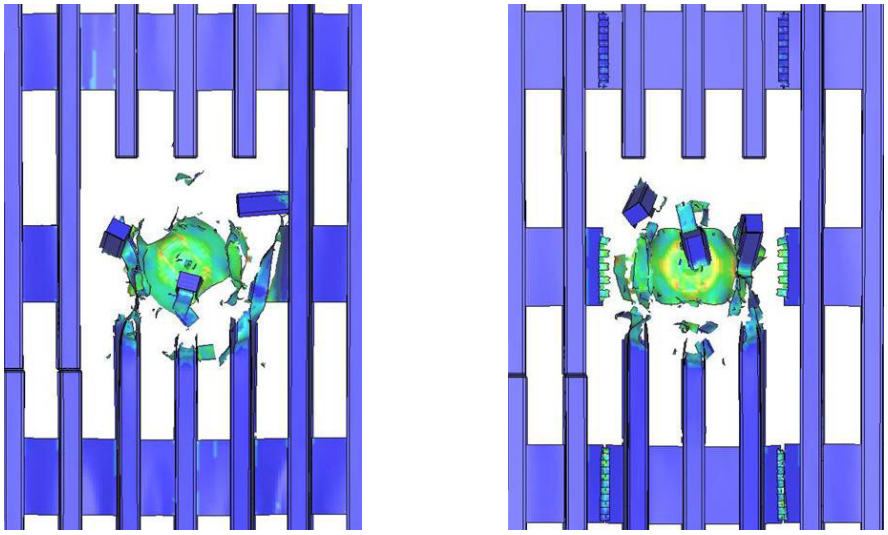

(a) Merged spandrel analysis **(b) Spliced spandrel analysis**

Figure C–74. Example engine impact analysis with different spandrel connection treatments.

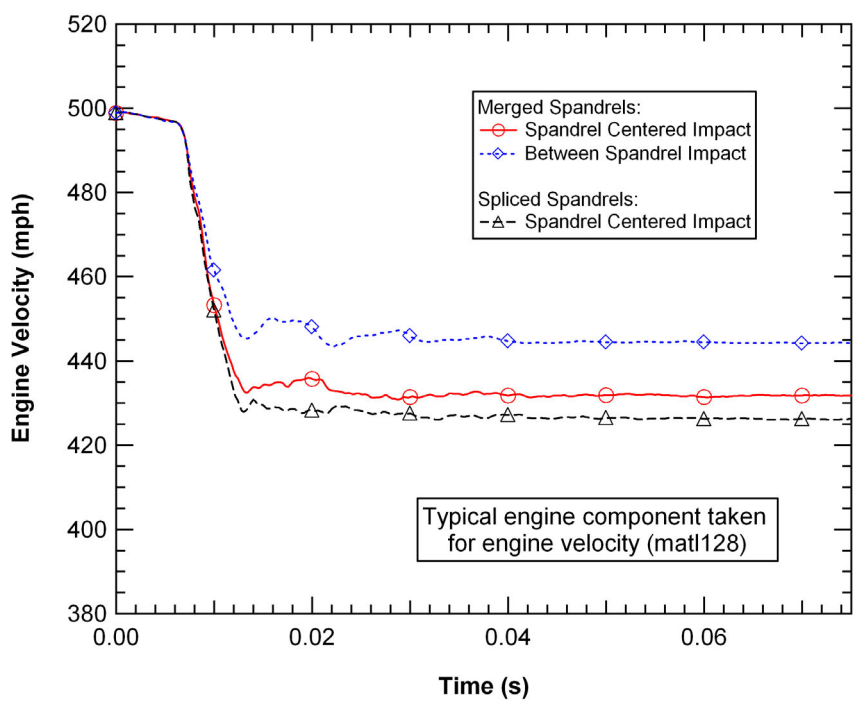

Figure C–75. Engine velocity history for the exterior wall impact.

The above comparison suggests that the splice plate has a relatively small influence on the exterior wall strength. The addition of the splice plate has approximately a 10 percent effect on the change in engine velocity during impact and penetration of the exterior wall. However, the spandrel connection model does not introduce a large computational cost and results in a more appropriate failure mode for the spandrels in the impact zone. Therefore, the spandrel splice connections will be maintained in subsequent impact analyses.

C.4.3 Core Column Impact Analyses

Engine Impact Analysis

Preliminary analyses of an engine impacting a single core column indicated that the impact load was sufficient to penetrate and overwhelm the column. Subsequent analyses of an engine impacting core columns have included multiple impacts and will be reported later along with the subassembly analysis and the uncertainty analyses.

Wing Section with Fuel Impact Analysis

Component analyses for core columns impacted by fuel-filled wing sections were conducted for both wide flange and box type columns (Figs. C–76 through C–79). Similar to exterior column analyses, the primary purpose was to progress from the initial finely meshed brick element models to coarser shell element models. Figure C–76 (wide flange core column) and Fig. C–78 (box section core column) compare the fine brick model and coarser shell model response under the same loading conditions. Figures C–77 and C–79 show corresponding displacement and kinetic energy comparisons for, respectively, the wide flange and box section core column models. The figures indicate that the response of the coarser shell models is very similar to that of the fine brick models. Therefore, the shell element formulation and mesh refinement of the coarse model are sufficient to capture the impact damage mechanisms in this component impact scenario.

C.4.4 Combined Engine Impact Analyses

An example of engine impact analysis is presented in this section to demonstrate the damage response to both exterior and interior columns. The impact configuration is an engine impacting at 560 mph (250 m/s) against a set of exterior columns in a single exterior panel, an interior box column, and an interior wide flange column. The columns are modeled using shell elements. The spacing between exterior and core columns was reduced to shorten the run time necessary for the complete impact scenario. The simulation included three external panels stacked vertically such that the impacted column was bolted to additional panels both above and below. The core columns models were several floors tall to reduce the influence of the clamped boundary conditions at the ends.

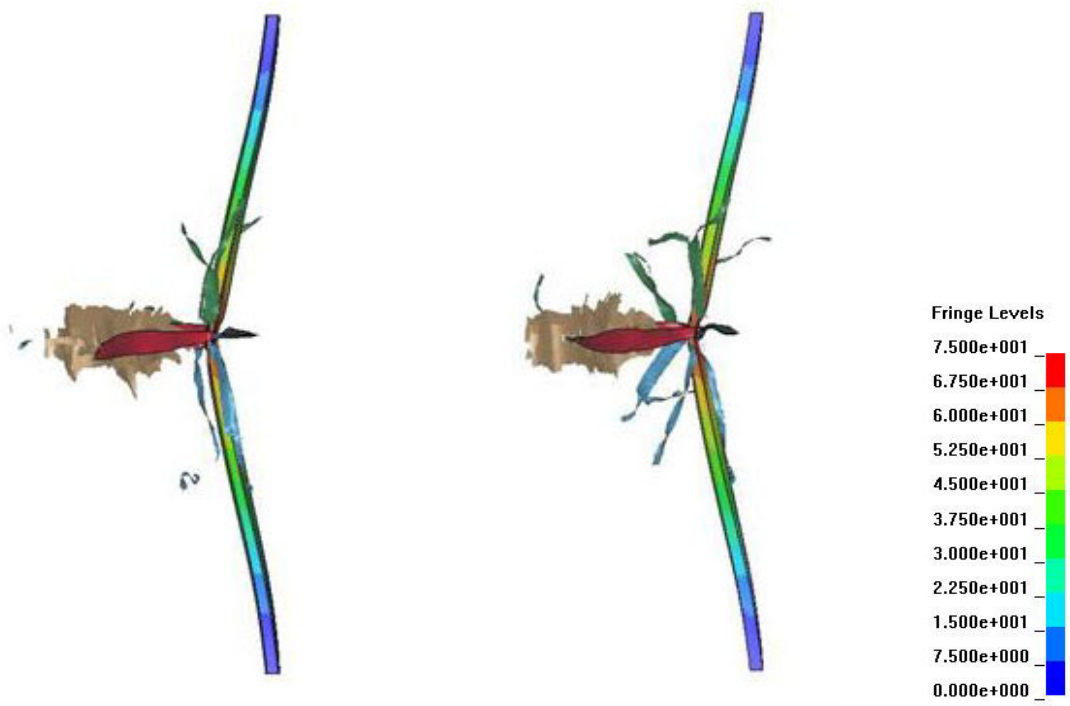

(a) Fine brick element column **(b) Coarse shell element column**

Figure C–76. Wide flange core column response comparison, showing contours of the displacement magnitude (in.).

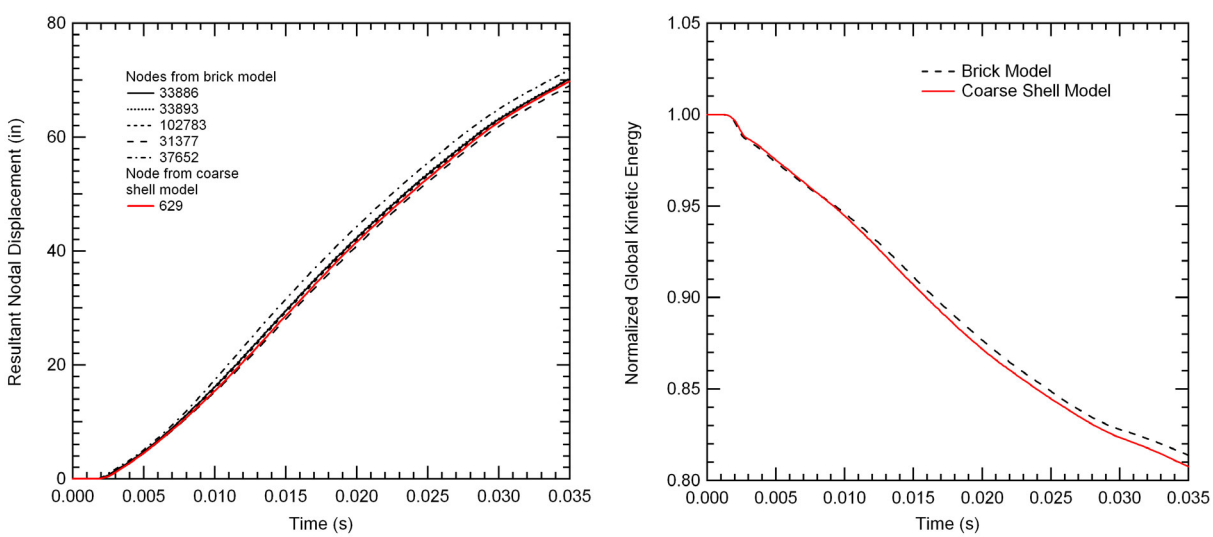

Figure C–77. Displacement and kinetic energy comparison for wide flange core column wing impact analysis.

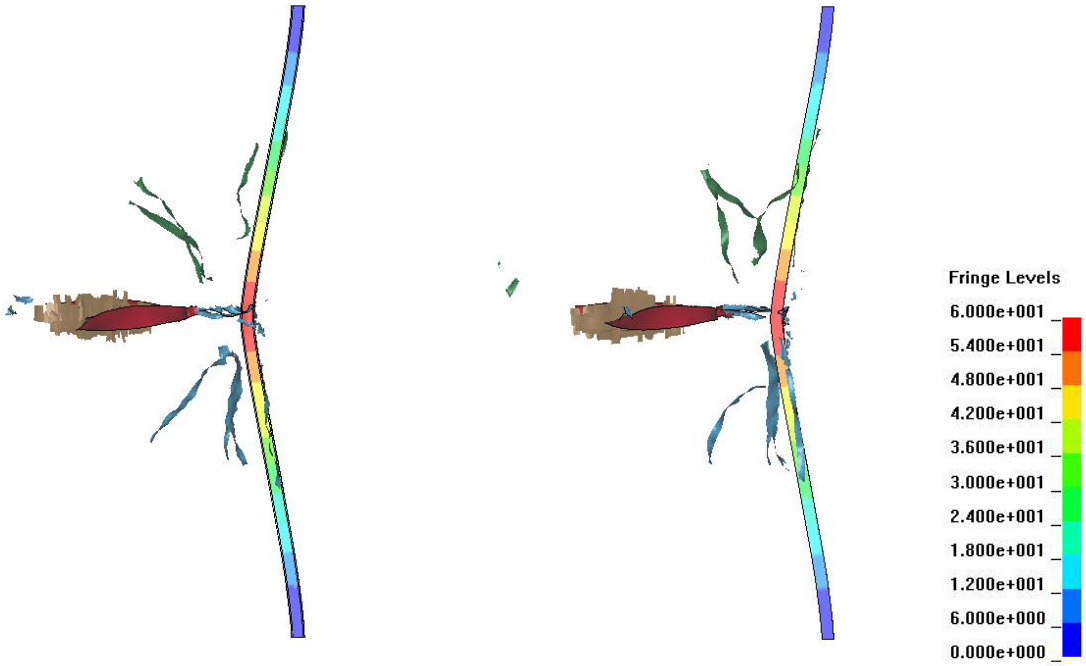

(a) Fine brick element column **(b) Coarse shell element column**

Figure C–78. Box core column response comparison, showing contours of the displacement magnitude (in.).

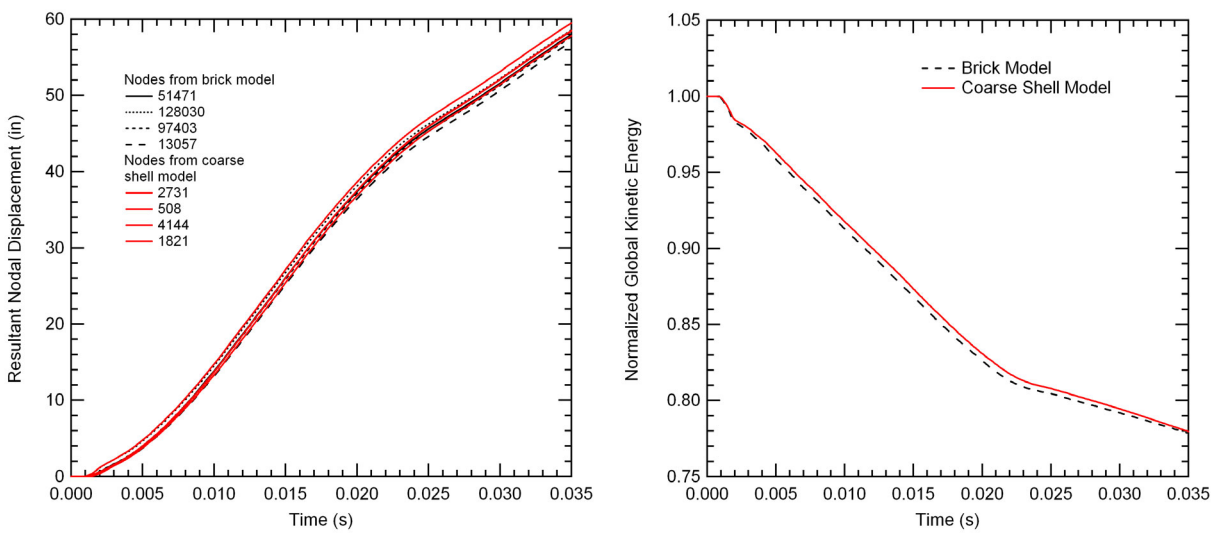

Figure C–79. Displacement and kinetic energy comparison for box core column wing impact analysis.

The impact scenario is illustrated in Fig. C–80 (a). The calculated impact damage is shown at a time of 90 ms in Fig. C–80 (b). The calculated engine impact response completely fails all of the columns with a residual velocity of the engine of approximately 224 mph (100 m/s). The deformations of the column include large lateral displacements which would be significantly reduced if the constraint effects of the concrete floor slab were added. The deceleration profile of the major engine debris fragment is given in

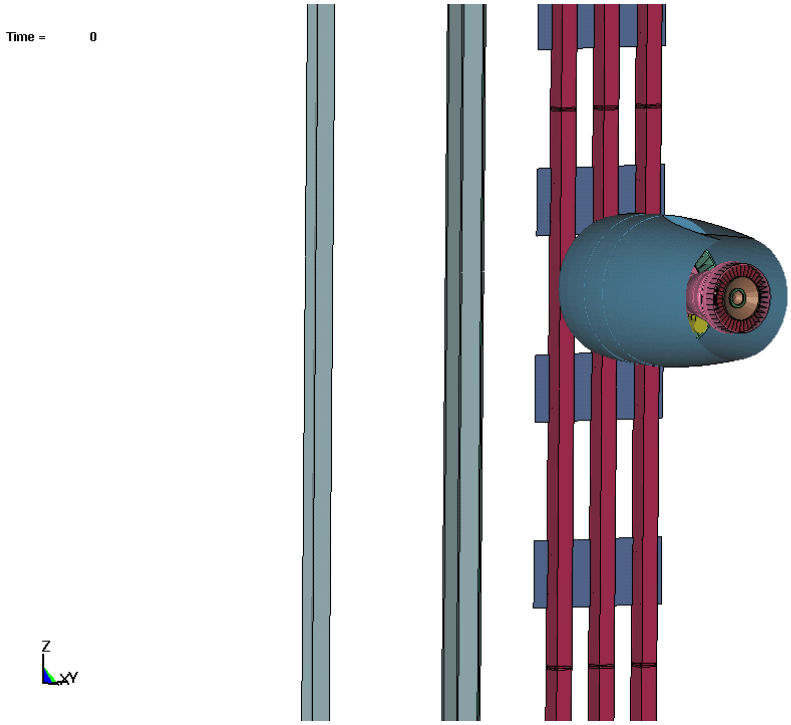

(a) Initial configuration

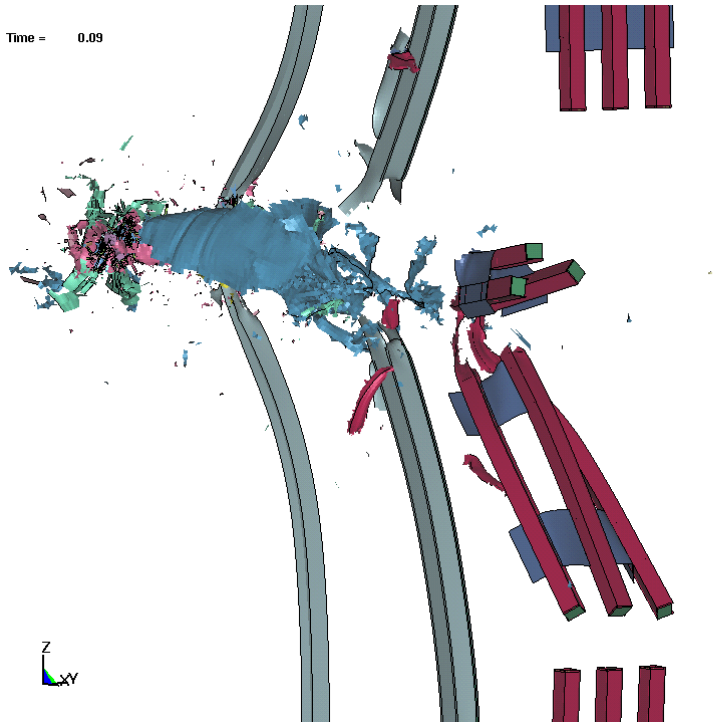

(b) Impact response at 90 ms

Figure C–80. Example engine impact analysis with interior and exterior columns.

Fig. C–81. The majority of the engine structure has been broken into fragments by the combination of the three impacts. The resulting size, strength, and velocity of the engine debris are not likely to produce severe impact damage or failure to a subsequent core column.

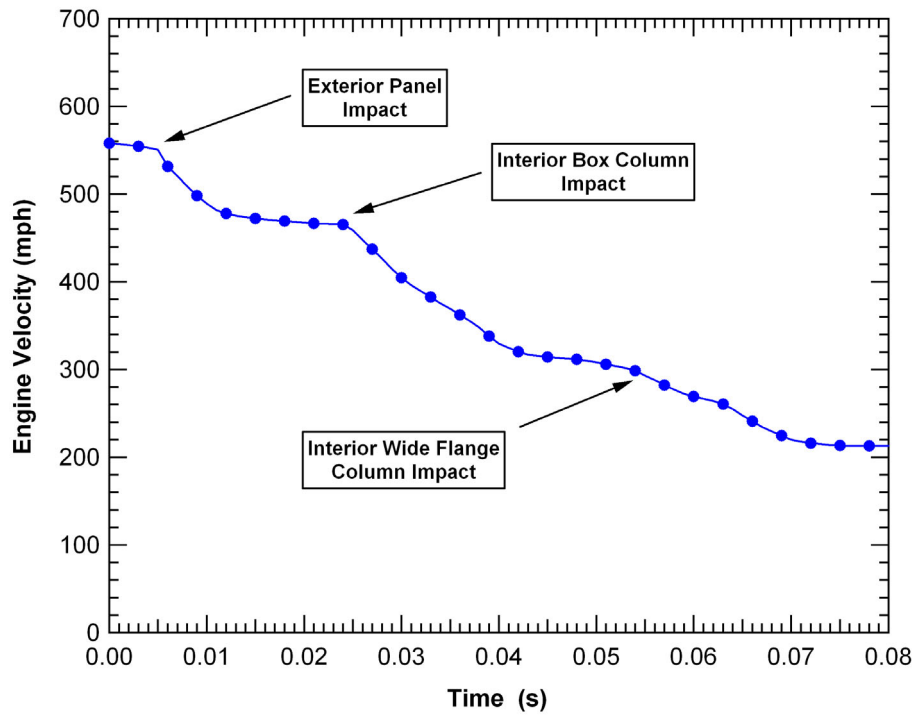

Figure C–81. Example engine impact analysis with interior and exterior columns.

This example illustrates the large level of damage produced by a massive aircraft component, such as an engine, at high impact velocity. The impact energy is sufficient to overwhelm a single core column and, therefore, makes it difficult to determine the effects of column component modeling parameters on the impact response using this impact scenario.

C.4.5 Floor Assembly Component Analyses

An additional component model analyzed is the truss floor assembly. The failure and penetration of the floor structures is important for assessing the extent of damage and the spread of fuel and debris through the structure. The integrity of the floor structures could also be significant in the analysis of the subsequent fire behavior in the towers. Loading of the floor structure was achieved by direct impact by the engine and a simplified impactor.

Component models of a section of the composite floor assembly outside the core were generated and used in various impact analyses. Initial floor component models used the detailed combination of brick, shell, and beam elements. Subsequent floor assembly models were less refined with shell and beam elements only. A comparison of the two floor system models and analyses is given in Table C–7. The modifications have reduced the size of the model by an order of magnitude and the run times by more than 80 percent.

Table C–7. Truss floor assembly component analyses comparison.

Model Type	Fine Brick Model	Coarse Shell Model
Number of beam elements	6,928	3,440
Number of brick elements	230,778	0
Number of shell elements	148,256	39,000
Total nodes	372,084	48,971
CPU time	16,796 s (4.7 h)	2,482 s (0.7 h)
Elapsed time	26,553 s (7.3 h)	4,454 s (1.2 h)

The impactor used in the initial component modeling is a simplified plow type impactor which promotes repeatable damage, not complicated by all the debris and randomness associated with an engine-floor impact. The weight of the plow impactor is comparable to an engine and the impact velocity was 500 mph. An example of a plow impactor analysis with the fine mesh floor model is shown in Fig. C–82. The calculated impact damage with a corresponding shell element floor system model is shown in Fig. C–83. This component impact configuration is useful for comparing the differences in response with changes in the modeling methods or refinement. Additional simulations with an engine impactor are being performed to validate the modeling approach and will be reported at a later date.

C.5 SUMMARY AND PRELIMINARY FINDINGS

The objectives of this project are to calculate the aircraft impact response of the WTC towers, including damage to WTC tower structural systems, acceleration environment, and fuel and debris dispersion. The impact analyses are conducted at various levels, including: (1) the component level, (2) the subassembly level, and (3) the global level to estimate the probable damage to the towers due to aircraft impact. The analyses also include simplified and approximate methods. Analysis of uncertainties using the component, subassembly, global, and simplified analyses will also be conducted to assess the effect of variability associated with various parameters on the damage estimates.

Significant progress has been made to identify the proper constitutive relationships, including high strain-rate effects and failure criteria for the various materials included in the analysis of aircraft impacts into the WTC towers. These materials include steels used in the exterior walls and core columns of the towers, weldment, bolts, reinforced concrete, and aircraft materials.

The development of the Boeing 767 aircraft model for impact analysis is nearing completion. The engine and wing models have been completed and are being used in the component and subassembly analyses. Work is underway to finalize the model of the fuselage, nose, tail, and nonstructural components of the aircraft.

The WTC towers and Boeing 767 aircraft are extremely complex structural systems, and a large database of detailed structural information has been collected on both the towers and the aircraft. In the model development process, the objective was to include all of the structural components and details of both the aircraft and towers that would influence the impact response and damage. This approach results in very large models for the tower and aircraft. The application of the models in the component and subassembly analyses were used to determine model simplifications that can reduce the overall model size while maintaining fidelity in determination of the impact damage.

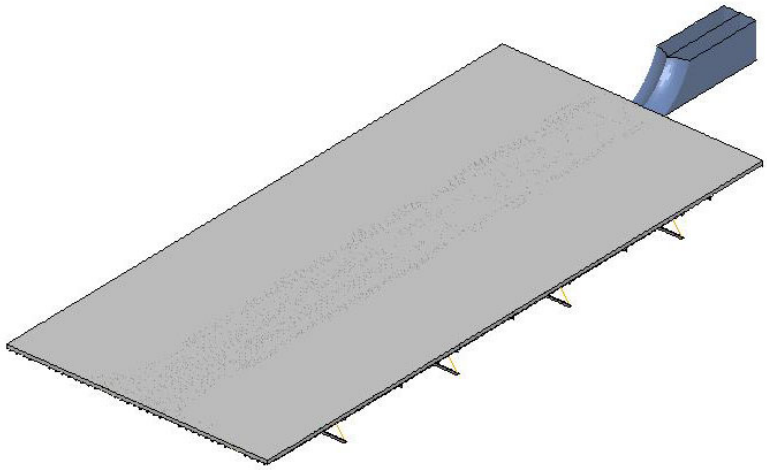

(a) Initial configuration

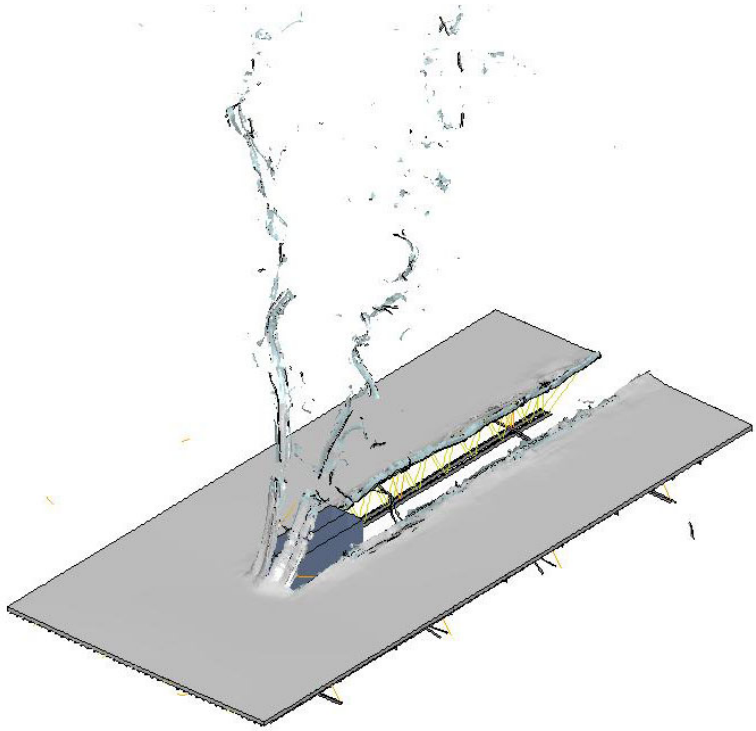

(b) Impact response at 0.10 s

Figure C–82. Floor assembly impact analysis with brick element concrete slab.

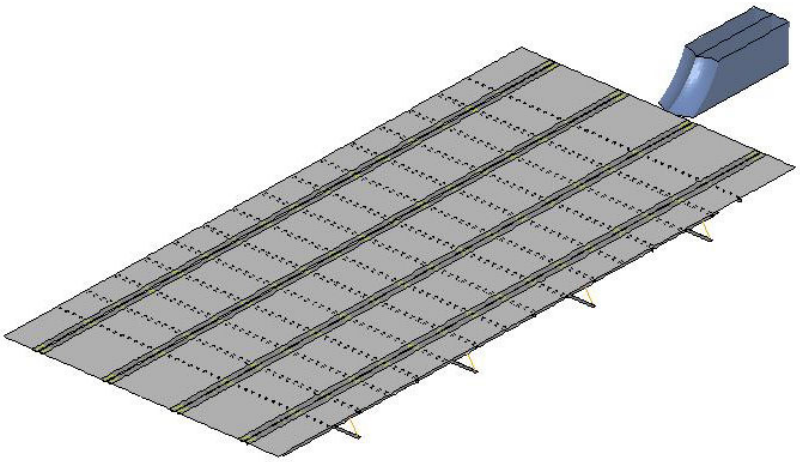

(a) Initial configuration

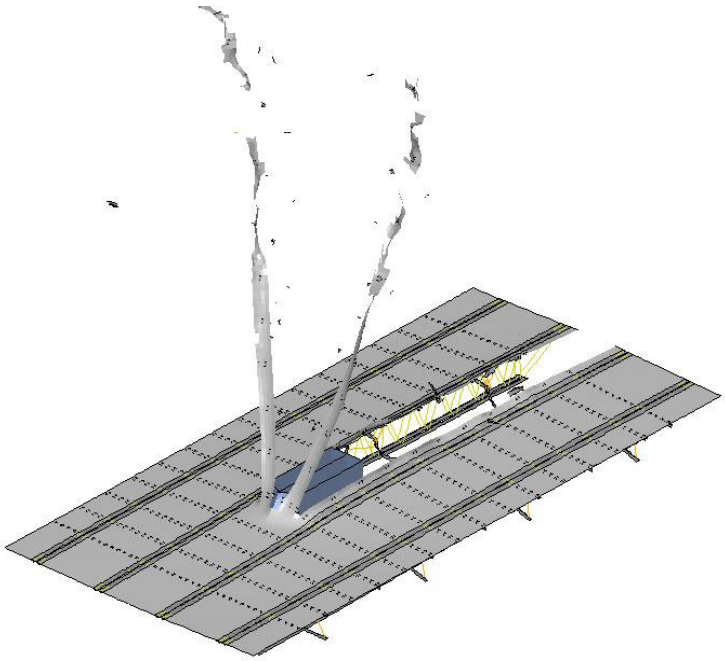

(b) Impact response at 0.10 s

Figure C–83. Floor assembly impact analysis with shell element concrete slab.

A series of component impact analyses were performed using models of tower exterior and core columns with wing section and engine component models as impactors. These models are used to develop the simulation techniques required for the global analysis of the aircraft impacts into the WTC towers. The following results were obtained from the component impact analyses:

- A 500 mph (223 m/s) engine impact against an exterior wall panel results in a penetration of the exterior wall and failure of impacted exterior columns. If the engine does not impact a floor slab, the majority of the engine core will remain intact through the exterior wall penetration with a reduction in velocity between 10 percent and 20 percent. The residual velocity and mass of the engine after penetration of the exterior wall is sufficient to fail a core

column in a direct impact condition. Interaction with additional interior building contents prior to impact or a misaligned impact against the core column could change this result.

- A normal impact of the exterior wall by an empty wing segment from the wing tip region will produce significant damage to the exterior columns but not necessarily complete failure. This is consistent with photographs showing the exterior damage to the towers due to impact. Specific details of the damage will depend on details of the impact orientation and locations of internal wing components such as control surface actuators and arms.

- A fuel-filled wing section impact results in extensive damage to the external including complete failure of the exterior columns. This is also consistent with photographs of the exterior damage. The resulting debris propagating into the building maintains the majority of the initial momentum prior to impact.

- Three different numerical techniques were investigated for modeling impact effects and dispersion of fuel: (1) standard Lagrangian finite element analysis with erosion, (2) Smoothed Particle Hydrodynamics (SPH) analysis, and (3) Arbitrary-Lagrangian-Eulerian (ALE) analysis. Of these approaches, SPH analyses appear to offer the greatest potential for modeling fuel in the global impact analysis due to the combination of both computational efficiency and modeling fidelity.

C.6 REFERENCES

ASTM Designation A 370 - 03a. 2003. "Standard Test Methods and Definitions for Mechanical Testing of Steel Products," Approved June 10.

Brown, W. F. Jr., H. Mindlin, and C. Y. Ho. eds. 1991. *Aerospace Structural Metals Handbook.* CINDAS/Purdue University Publishers, vol. 3 & 4.

Kirkpatrick, S. W., J. H. Giovanola, and J. W. Simons. 1996. DYNA3D analysis of dynamic fracture of weldments, IA'96, *Proceedings of International Seminar on Quasi-Impulsive Analysis.* November 20–22, Osaka, Japan, pp. A6.1-15.

LS-DYNA Keyword User's Manual. 2003. Livermore Software Technology Corporation, version 970. April.

Mackenzie, A. C., J. W. Hancock, and D. K. Brown. 1977. On the influence of state of stress on ductile failure initiation in high-strength steels, *Eng. Fracture Mechanics*, 9, 167–188.

Military Handbook. 1987. *Metallic Materials and Elements for Aerospace Vehicle Structures.* U.S. Department of Defense, MIL-HDBK-5F.

Mudry, F. 1985. Methodology and applications of local criteria for prediction of ductile tearing, *Elastic-Plastic Fracture Mechanics.* L.H. Larson, ed. ECSC, EEC, EAEC, Brussels and Luxembourg, Belgium, pp. 263-283.

Rice, J.R., and D.M. Tracey. 1969. On the ductile enlargement of voids in triaxial stress fields, *J. Mech. Phys. Solids*, 17, 201–217.

Wischers, G. 1978. Application of effects of compressive loads on concrete, *Betontech*, nos. 2 and 3. Berlin.

XYZ Scientific Applications, Inc. 2001. *TrueGrid Manual*, version 2.1.0. September.